POLITECNICO DI TORINO

POLITECNICO DI TORINO

Master Degree course in Mechanical Engineering

Master Degree Thesis

Experimental Testing and Dynamic Modelling of a Planetary Magnetic Gearbox Prototype

Supervisors
Prof. Maurizio Repetto
Dr. Luca Dimauro

Candidate
Alberto Coricciati

Academic Year 2024-2025

Abstract

This thesis studies the prototype of a coaxial Planetary Magnetic Gearbox (PMG) developed at Politecnico di Torino, analysing the experimental tests results as well as the developing a dynamic model in Simulink environment to conduct simulation tests. The PMG consists of two pairs of magnetic wheels acting as the sun and the ring of an epicyclic gear, and a set of ferromagnetic poles, acting as the planets, that can shift between the two wheels passing through a neutral position.

The study begins with an overview of the magnetic gears technology, focusing on its advantages over their traditional mechanical system counterparts, including reduced wear and tear, overload protection and absence of lubrication requirements. The analysis shifts to the main configuration studied, the coaxial PMG, highlighting its working principles and the derivation of its dynamic equations and magnetic torque transmission. The prototype under study is studied, including an overview of all the main components of the test bench, that is tested in both neutral and engaged configuration, via the adoption of a new methodology to account for the thermal stability and accuracy of the results. A correction coefficient has been proposed to account for the residual magnetic losses still present in the neutral configuration.

The main contribution of this work is the creation of a digital copy of the test bench, developed in Simulink environment, that replicates the architecture of the prototype and allows for the study of its dynamic behaviours. The model integrates all the main components of the test bench, and includes the mechanical torque maps obtained from the neutral testing as well as the magnetic torque transmission maps obtained through FEM analysis during previous works. The overall performances of the model achieve high consistency results, bearing errors of total system efficiency lower than 0.5% across all load scenarios analysed. The results show the high contribution of mechanical friction due to the bearings in the overall power losses, and validate the model capabilities to accurately reflect the prototype dynamics.

Contents

List of Figures

List of Tables

Chapter 1

Introduction

This chapter aims to provide a general overview of magnetic gears, showing their unique properties and the motivations behind their use. A brief historical context is provided, highlighting the main designed solutions, along with a comparative analysis with traditional mechanical gears, showing the advantages and limitations of both systems. Lastly, the field of application of magnetic gears is explored, showcasing their versatility and the growing interest towards this technology.

1.1 What are Magnetic Gears

Magnetic gears are an innovative solution in the field of power transmission systems that have seen significant advancements in the recent years. Unlike their mechanical counterparts, which rely on the mechanical torque transmitted from one gear to the other due to the physical contact between their meshing teeth, magnetic gears use the interaction between magnetic fields to achieve the torque transfer (Figure 1.1). This absence of contact in the working operations allows a reduction of wear and tear, lower maintenance costs and a significant reduction in the apparatus noise, positioning magnetic gears as a promising alternative for future applications in multiple fields.

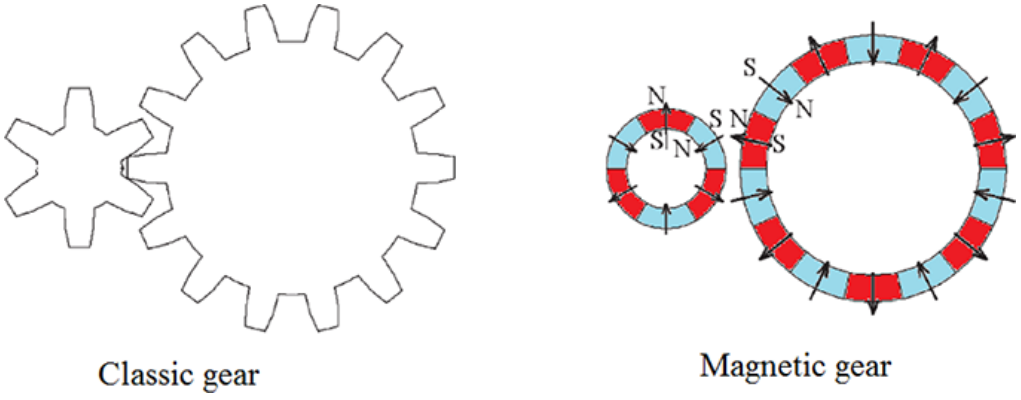

Figure 1.1: Simplified scheme of a mechanical and magnetic gear. [13]

Magnetic gears have become an area of major interest due to their ability to solve many challenges associated with the conventional mechanical gears. The evolution of magnetic gear technology aligns with the advancements in permanent magnet materials that provide stronger magnetic fields and higher efficiency. Their non contact operation allows for an increased working life, making them viable in harsh and specialised environments that cannot be easily accessed for maintenance operations.

The growing interest in this field is reflected in the number of papers and patents published each year, that saw an exponential growth in the last 20 years, as shown in the histogram in Figure 1.2.

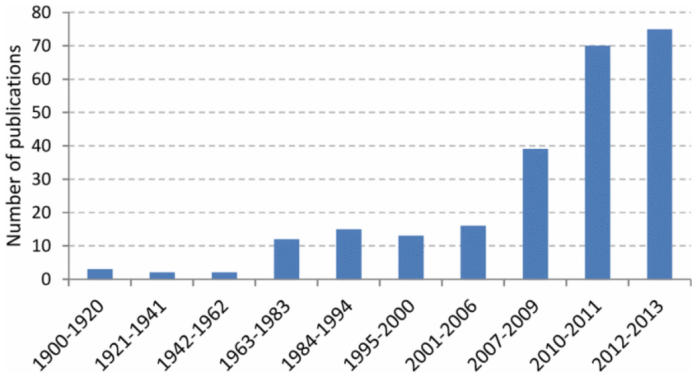

Figure 1.2: Publishings on magnetic gears (from 1900 to 2013) [31]

1.2 History of Magnetic Gears

The origin of magnetic gears goes back to the early 20th century, and specifically in 1901 with an electromagnetic spur gear patented by Armstrong [1]. Armstrong's design used for the first time magnetic interactions by putting coils on the teeth of conventional gears to transmit torque from one the gear to the other without contact being needed (Figure 1.3). These early designs utilised electromagnetic inductions phenomena, but they lacked the efficiency of permanent magnets.

A key milestone occurred in 1941, when Faus [11] proposed an alternative design that replaced traditional gear teeth with magnetic poles arranged in a circular pattern (Figure 1.4). The main problems of this new design were the performance limitations given by the limited torque densities and efficiencies obtained by the available magnets.

In the 1960s, Martin [23] published the first design of a coaxial magnetic gears, having an inner and an outer rotor, and a flux modulator interposed between them (Figure 1.5). Despite the poor performances related to practical constraints given by the poor quality of magnets, this design will prove to be of great interest in the 2000s for the development of the magnetic gears industry.

The research on this field didn't see much improvement until the 1980s, when the development of neodynium-iron-boron (NdFeB) magnets allowed for a dramatic increase

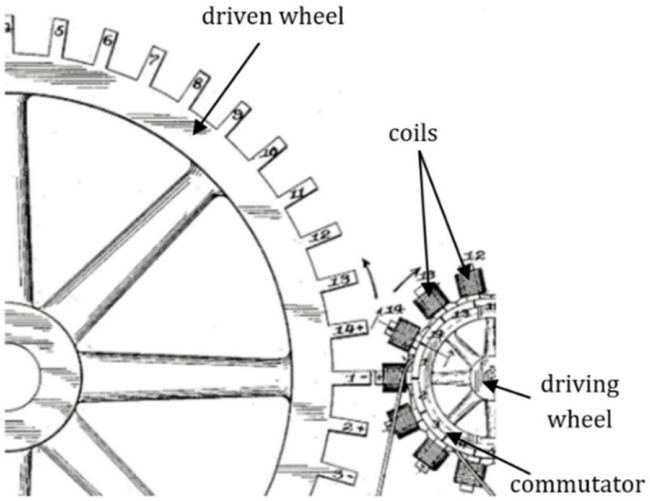

Figure 1.3: The first patented magnetic gear, Armstrong 1901. [22]

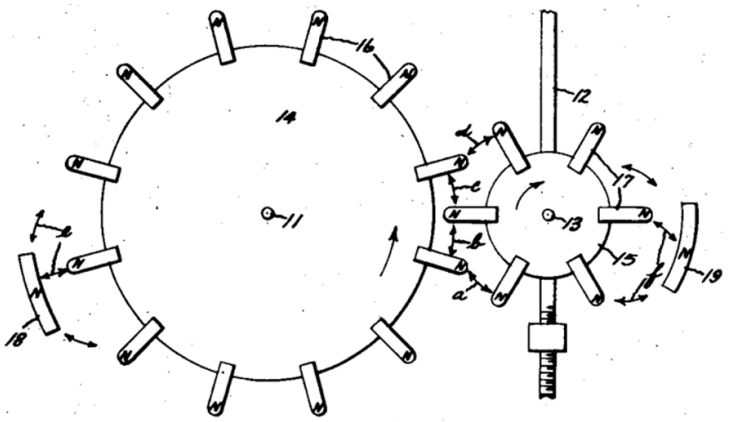

Figure 1.4: Faus's design of a magnetic gear, 1941.

in magnetic strength, allowing higher torque densities and improved efficiencies for magnetic gears that started to be comparable to their mechanical counterparts. This lead to a renewed interest in magnetic gears with researchers exploring new designs and potential applications.

In 2001, Atallah and Howe [3] modified and upgraded the coaxial magnetic gear design ideated by Martin with the use of the NdFeB magnets, creating what is known as the leading design for magnetic gears, which will be the focus of the study for the next chapters.

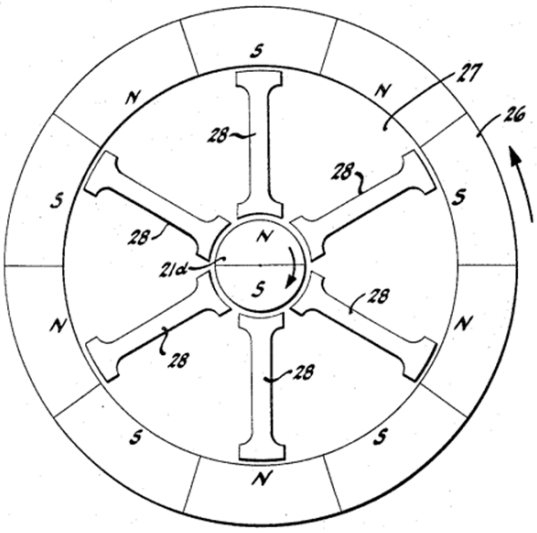

Figure 1.5: Martin's first design of coaxial magnetic gears, 1961.

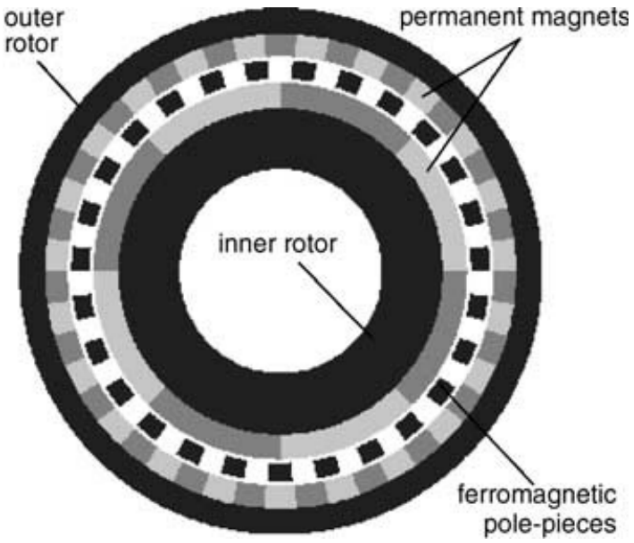

Figure 1.6: Atallah's refined design of coaxial magnetic gears, 2001. [2]

1.3 Modern Magnetic Gears

Modern magnetic gears can be categorised into non modulated and modulated designs (Figure 1.7). The ones adopting the non modulated design, such as spur and worm magnetic gears, rely on the direct magnetic interaction between permanent magnets. While this design offers a simpler structure, they generally cannot produce higher torque densities. Modulated magnetic gears use instead a ferromagnetic flux modulator to increase their torque transmission.

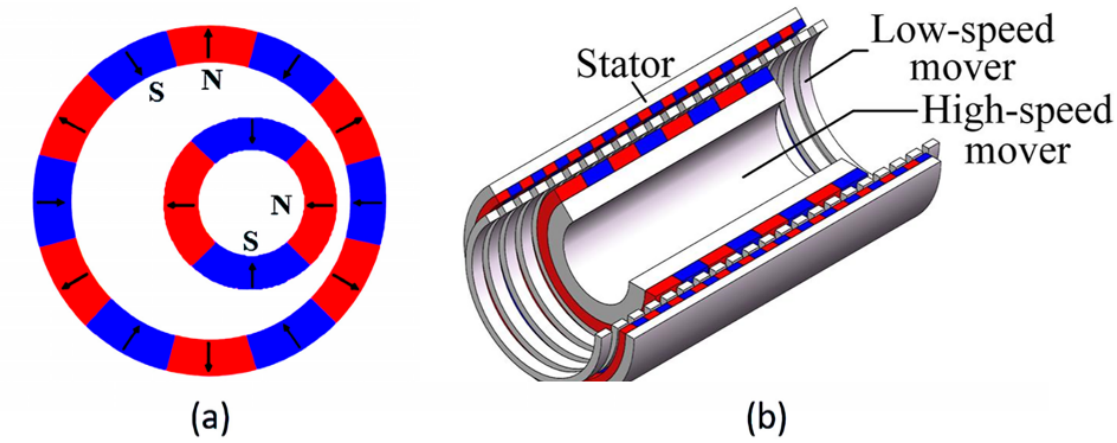

Figure 1.7: Examples of Non Modulated [28] (a) and Modulated [36] (b) magnetic gears.

The most common designs of magnetic gears that are being researched and implemented nowadays are:

- Coaxial Magnetic Gears : these gears consist of an inner and outer permanent magnet rotors that are separated by a fixed magnetic flux modulator. This design shows high torque density and efficiency in a compact structure. The most recent innovations include the Halbach array (the permanent magnets are positioned in such a way that the magnetic field is directed favouring a designed direction) and Spoke type (uses ferromagnetic spokes to guide the magnetic flux) configurations, which offer improvements in parameters like torque density and loss reduction (Figure 1.8).

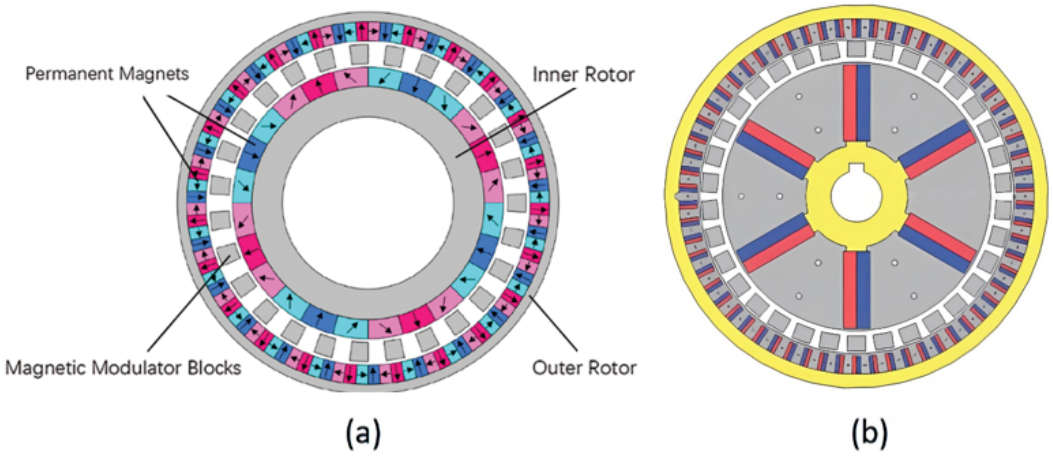

Figure 1.8: Examples of coaxial magnetic gears: Halbach array design [33] (a) and Spoke type design [24] (b) magnetic gears.

- Planetary Magnetic Gears: this design is inspired from the traditional mechanical planetary system, and is made up by a particular set up of coaxial magnetic gears: an inner sun gear, an outer ring gear and either with a set of intermediate planets fixed fixed together with a carrier or with simply a carrier (Figure 1.9). While the first design guarantees higher torque capacity, the second model is more used thanks to its simplicity and compactness, keeping an adequate torque density. Planetary magnetic gears offer multiple operational modes, allowing the designer to optimise the gear ratios for specific applications.

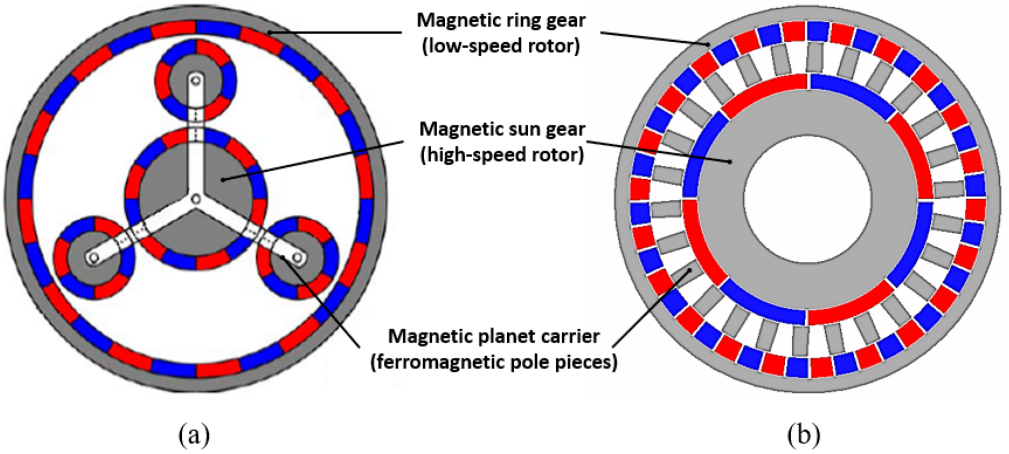

Figure 1.9: Examples of planetary magnetic gears: with multiple planets (a) and with just the carrier (b). [15]

- Harmonic Magnetic Gears: these gears use sinusoidal variation in the air gap to achieve smooth torque transfer at very high gear ratios. This variation is typically achieved through the use of an oval shaped flexible rotor, also known as a wave generator, which creates the sinusoidal air gap variation. The wave generator causes another rotor with permanent magnets to rotate at a specific gear ratio relative to an outer permanent magnet stator (Figure 1.10). Although very precise, harmonic magnetic gears are very complex and expensive to manufacture.

- Axial Magnetic Gears: these gears operate in a plane perpendicular to the shaft axis, making them suitable for applications that require a flat form factor Figure 1.11. Recent innovations in materials and geometries have increased their performance and led to their use in portable devices and compact industrial machines.

- Linear Magnetic Gears: these gears convert rotational motion into linear displacement, making them well suited for applications that require a linear motion (Figure 1.12). They excel in marine environments and particularly in wave energy converters. [12]

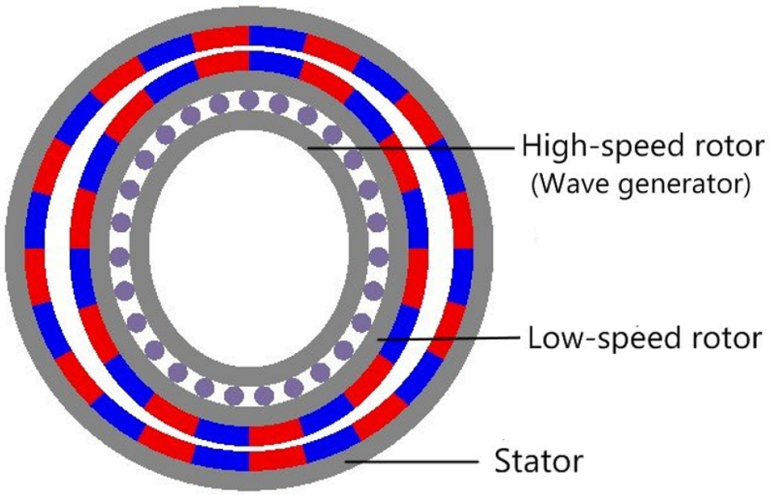

Figure 1.10: Harmonic magnetic gears design. [32]

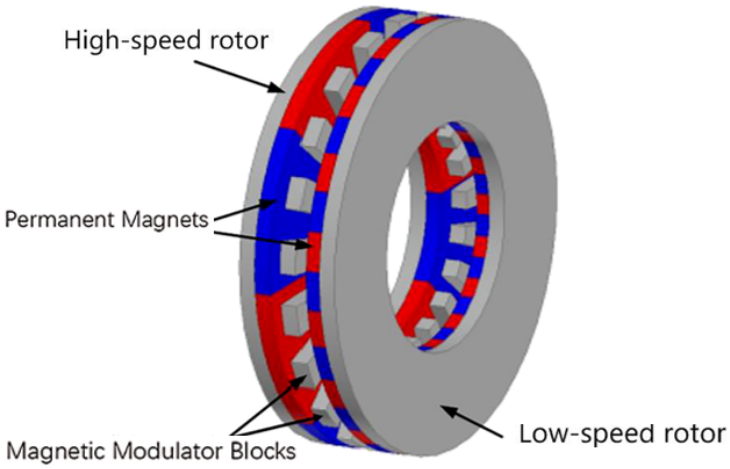

Figure 1.11: Axial magnetic gears design. [29]

1.4 Comparison with Mechanical Gears: advantages and limitations

Mechanical gears are the most widely used power transmission devices in industrial, automotive and energy sectors. The constant physical contact required to transmit torque leads, over time, to wear and tear of the meshing teeth surfaces, resulting in increased friction, reduced efficiency, reduced lifespan and the need for regular maintenance, to restore the lubricants and, eventually, to replace entire components. This leads to frequent downtime for maintenance, increasing operational costs and reducing the productivity of the machines. Additionally, the mechanical friction between gear teeth generates significant noise and vibration, often requiring additional noise and vibration dampening

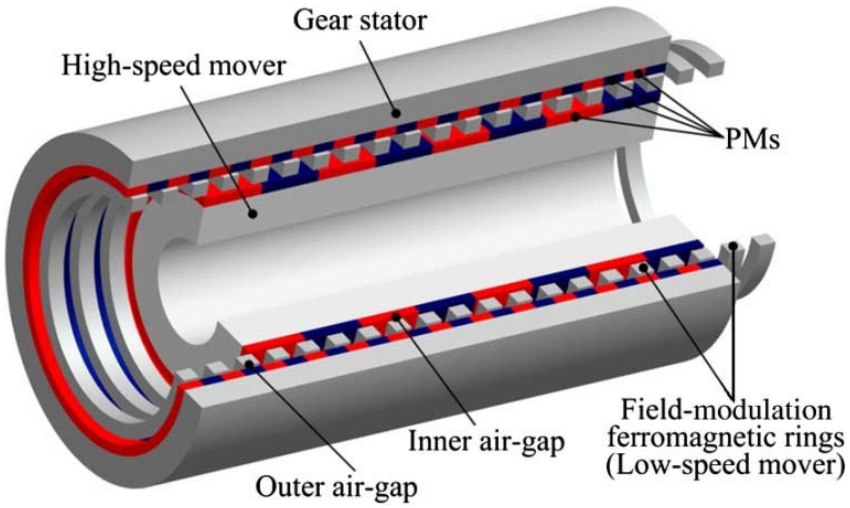

Figure 1.12: Linear magnetic gears design. [19]

designs and measures [21] [10].

Magnetic gears, on the other hand, represent an innovative alternative to mechanical gears and operate on a fundamentally different principle. While their designs are extracted from their traditional counterparts (Figure 1.13), they utilise magnetic fields to transmit torque, eliminating the need for direct physical contact between moving parts.

This non-contact operation offers several critical advantages:

- Reduced Wear and Tear: the absence of direct contact significantly reduces wear and tear on the gear components. This allows for extended operational lifespans, reduced maintenance requirements and machine's downtime, and increased reliability. This is extremely beneficial in harsh environments or applications where maintenance is difficult to operate, such as in marine [16] and aerospace fields [25].

- Overload Protection and Increased Reliability: when loaded with excessive torque, mechanical gears could fail catastrophically, leading to costly repairs and downtime. In contrast, magnetic gears have an intrinsic overload protection: in case of excessive torque being transferred, the magnetic coupling gets weaker allowing the rotors to slip and disengage without causing any permanent damage, protecting the connected equipment. This protection mechanism of magnetic gears further increases their durability and reliability.

- Noise and Vibration Reduction: the elimination of direct contact between moving parts significantly reduces the noise and vibration generated during operation. This makes magnetic gears ideal for applications where quiet operation is mandatory, such as in medical field and residential locations.

- Elimination of Lubrication: the non contact operation of magnetic gears eliminates the need for lubricants, which is a significant advantage in food and pharmaceuticals applications, where the presence of lubricants could contaminate products, posing

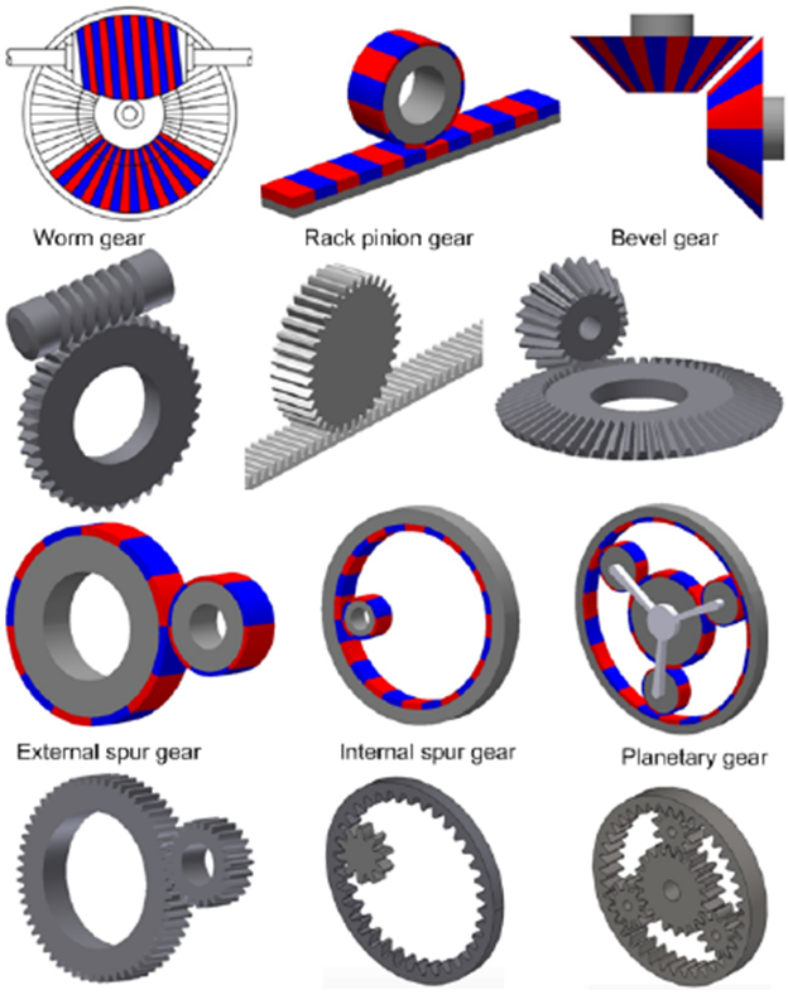

Figure 1.13: Mechanical gears and their magnetic counterparts. [32]

serious hygiene and safety risks. In addition to that, it also decreases the need for maintenance, with all the positive effects mentioned above.

- Improved Efficiency: while historically, magnetic gears have exhibited lower torque density compared to their mechanical counterparts, advancements in materials and design have significantly improved their efficiency. The development of high performance permanent magnets, such as neodymium-iron-boron (NdFeB) alloys, has allowed magnetic gear systems to work with efficiencies comparable to, and in some cases exceeding, traditional mechanical gears, particularly at higher speeds (Figure 1.14).

Despite their numerous advantages, magnetic gears also have certain limitations:

- Torque Density Limitations: while significant progress has been made in improving torque density, magnetic gears still generally exhibit lower torque density compared

Gear type	Torque density (kNm/m^3)
Mechanical spur gear	100-200
Magnetic spur gear	10-20
Magnetic planetary gear	100
Concentric magnetic gear	70-150

Figure 1.14: Torque densities of magnetic gears compared to spur mechanical gears. [31]

to some high performance mechanical gear systems. This limitation restricts their applicability in certain high torque applications, such as heavy machinery and large industrial equipment.

- Complexity of Design and Manufacturing: the design and manufacturing of high performance magnetic gears can require advanced manufacturing techniques. This can increase the complexity and cost of design and production.
- Higher Initial Costs: the manufacturing and material costs associated with magnetic gears are generally higher than those of traditional mechanical gears. This higher initial investment can be a major obstacle, particularly in cost sensitive applications.

Modern research is actively addressing these limitations and the development of magnetic materials with improved properties is expected to further increase the performance and efficiency of magnetic gears. Advancement in digital modelling allows designers to use finite element methods (FEM) to systematically analyse the magnetic flux distribution, aiding the optimisation of new magnetic gears topologies and maximise working parameters, such as torque density and efficiency. Moreover, advancement in manufacturing technologies, such as additive manufacturing (3D printing), greatly helps with the production of more complex and customised magnetic gears, cutting manufacturing costs.

1.5 Applications of Magnetic Gears

The unique advantages of magnetic gears have led to the adoption of this technology across a wide range of applications. The biggest fields where they are implemented are:

- Automotive industry: reduced noise and vibration levels of magnetic gears are advantageous in hybrid and, particularly, electric vehicles, where the noise of traditional power transmission systems is more noticeable due to the absence of an internal combustion engine [4]. Moreover, the overload protection mechanism increases the reliability of the components and reduces the risk of catastrophic failures.

- Renewable energy sector: in offshore wind farms [8] and wave energy converters [20], the non contact operation reduces maintenance requirements, which are crucial due to the challenging and costly intervention. Additionally, their ability to work efficiently under varying loads and speeds makes them ideal for transmitting energy taken from wind and waves.
- Medical industry: magnetic gears are used in surgical instruments where precision and absence of vibrations is mandatory. Their ability to work without the need of lubricants is also crucial in medical environments, avoiding dangerous contaminations and ensuring the patient safety.
- Industrial automation and robotics: the smooth and precise torque transfer given by magnetic gears greatly benefits industrial automation, where backlash and vibrations can affect the quality of final product. Furthermore, their reduced need for maintenance contribute to lower machine downtime and higher productivity [17].
- Aerospace industry: magnetic gears lower maintenance requirements and absence of lubrication renders them ideal for harsh environments, which is the case for satellite systems and other aerospace technologies, that can greatly benefit from their adoption over their mechanical counterparts [26].
- Oil and gas industry: the ability to have significant lower wear and tear compared to mechanical gears makes magnetic gears a reliable choice in drilling equipment, considering also their ability to work in high temperature and high pressure environments [30].
- Consumer devices: magnetic gears compact size and quiet operations make them suitable for household appliances, such as electric fans and washing machines.

As research and development continue to enhance the performance of magnetic gears and new manufacturing techniques emerge to cut the production costs, their range of applications is expected to expand even further, making them one of the leading solutions on the market.

Chapter 2

Planetary Magnetic Gearbox: Working Principle and Dynamic Behaviour

The concept of magnetic gears was broadly introduced in chapter 1 as a powerful alternative to traditional power transmission systems that rely on physical contact to transmit torque. Magnetic gears use, instead, magnetic interactions to transfer torque, resulting in reduced friction, wear, noise and vibrations.

In this chapter the focus will be shifted to the dynamic analysis of a planetary magnetic gearbox (PMG), a particular solution that stands out due to its ability to replicate the functions of traditional planetary gearboxes while also addressing their limits. This design proves to be very effective for transmitting torque and power in many fields, and specifically in the automotive industry, where the advancement of hybrid and electric vehicles have shifted the focus from more traditional mechanical setup in favour of new solutions that work in a smoother way, producing less noise and vibrations. The biggest advantage of PMG is their high torque density, that outperforms most of the other magnetic gears setups, and can rival the torque density of mechanical setups. Additionally, the PMG ability to achieve multiple gear ratios in a single configuration greatly increases their versatility, making them ideal for scenarios in which loads and velocities do not follow a specific pattern.

Section 2.1 will present an overview of mechanical planetary gearboxes, while section 2.2 will analyse their magnetic counterparts. In section 2.3, the working principle of the PMG technology will be addressed along with the definition of the magnetic transmitted torque. Finally, section 2.4 will explore the dynamic equations that will be needed to build the dynamic model of the PMG in later chapters.

2.1 Mechanical Planetary Gearbox

Before introducing the Planetary Magnetic Gearbox, it's important to discuss about it's mechanical counterpart, from which it originated.

The mechanical planetary gearbox has been widely used in various applications due to its ability to transmit a high torque output in a compact form ratio, resulting in high torque and power density, and a large gear reduction in a small volume. It consists of three main components: an inner sun gear, an outer ring gear and a set of planet gears connected together by a carrier that are simultaneously in mesh with the sun and ring gears (Figure 2.1). The number of planets can vary according to the specific application that the gearbox was designed for, but it typically consists of three or four planet gears. Having multiple planets allows a balanced partition of loads, avoiding load peaks that could compromise the working life of the system.

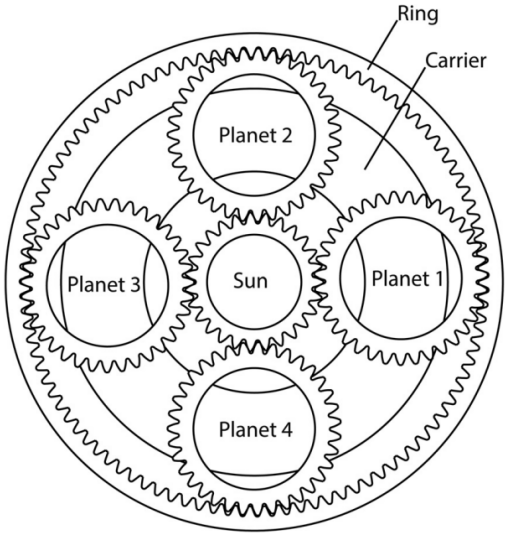

Figure 2.1: Schematic representation of a planetary gearbox with 4 planets [6]

In a typical planetary gearbox, the torque output is a function of the gear ratio between its components, namely the sun, the ring, and the planet gears. Such gear ratio can be changed both by modifying the design of the gears themselves, by increasing or reducing the number of their teeth, or by properly fixing one of their constitutive elements. In particular, a planetary gearbox consists of 2 degrees of freedom, hence to completely study its kinematic relations it is needed to define the rotational velocities of at least two of its elements, for example sun and carrier gears, to then compute the remaining speed, for example, the ring gear. Using Willis kinematic relation for planetary mechanical gear [35], it is possible to write:

$$\tau\omega_r + (1-\tau)\omega_c - \omega_s = 0 \tag{2.1}$$

where ω_s is the angular velocity of the sun gear, ω_c is the angular velocity of the carrier, ω_r is the angular velocity of the ring gear and τ is the ordinary gear ratio of the gearbox. Isolating the gear ratio on the left hand side, the formula can be rearranged as follows:

$$\tau = \frac{\omega_s - \omega_c}{\omega_r - \omega_c} \tag{2.2}$$

By imposing a null velocity of the carrier, the base gear ratio between sun and ring gears holds:

$$\tau_{s/r} = \frac{\omega_s}{\omega_r}\bigg|_{\omega_c=0} = -\frac{Z_r}{Z_s} \tag{2.3}$$

where Z_r and Z_s are the number of teeth of the ring and sun gear respectively. The same result can be obtained by combining the partial gear ratios between carrier (or planets) and sun and between ring and carrier (or planets), as follows:

$$\tau_{s/r} = \tau_{s/p} \cdot \tau_{p/r} = -\frac{Z_p}{Z_s} \cdot \frac{Z_r}{Z_p} = -\frac{Z_r}{Z_s} \tag{2.4}$$

where Z_p is the number of teeth of each planet gear. The minus sign shows that the sun and the ring gears rotate at opposite rotational speeds.

By changing the fixed element in the planetary system, it's possible to work in 6 different configurations, that will sorely depend on a single input and output relation. These operating modes are summed up in Table 2.1.

Gear ratio $\tau_{in/out} = \omega_{in}/\omega_{out}$	Input	Output	Fixed
$\tau_{s/r} = \tau$	sun	ring	carrier
$\tau_{r/s} = 1/\tau$	ring	sun	carrier
$\tau_{s/c} = 1 - \tau$	sun	carrier	ring
$\tau_{c/s} = 1/(1 - \tau)$	carrier	sun	ring
$\tau_{c/r} = \tau/(\tau - 1)$	carrier	ring	sun
$\tau_{r/c} = (\tau - 1)/\tau$	ring	carrier	sun

Table 2.1: Planetary gearbox configurations. [9]

Additionally, for any mechanical planetary gearbox it is possible to write the following relation between the number of teeth of ring, sun and planets:

$$Z_r = Z_s + 2Z_p \tag{2.5}$$

Combining equations 2.4 and 2.5, it is possible to define the working range of the gear ratio for the planetary system:

$$-\infty < \tau < -1 \tag{2.6}$$

Despite planetary gears have been a staple of a wide array of applications, they still experience noise and vibration problems. Their working conditions requires the constant contact between multiple meshing gears, that over time leads to increased frictional losses and wear, resulting in a reduced system efficiency and periodic maintenance. Nevertheless, statistics show that almost 60% of all the failures in mechanical transmission systems are caused by damaged gears. These problems lead to the research of alternative solutions, such as magnetic planetary gearboxes.

2.2 Planetary Magnetic Gearbox (PMG)

The magnetic planetary gearbox adapts the traditional mechanical planetary gearbox design but instead of relying on the physical contact between the gears, the torque is transmitted through magnetic interactions. The implementation of this magnetic gearbox leads to a number of benefits coming from the absence of contact between the gears, such as reduction of noise and vibrations, and protection against overload, preserving the system. A schematic representation of the equivalent magnetic planetary gear is shown in Figure 2.2, where the sun, planets and ring are equipped with permanent magnets.

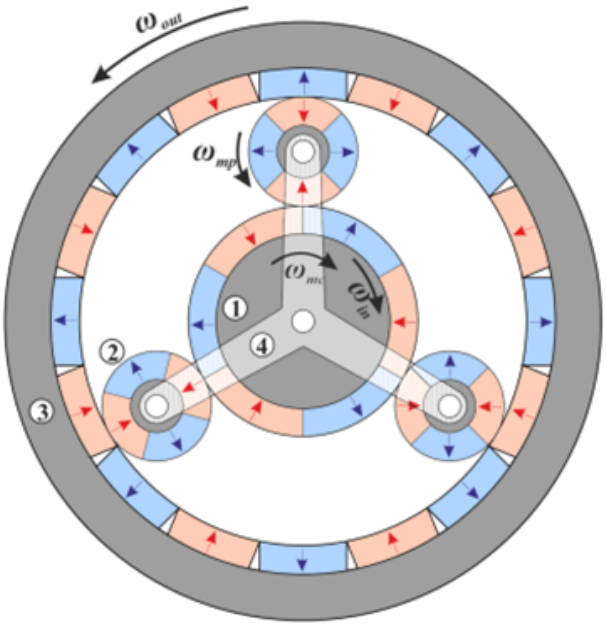

Figure 2.2: Example of a planetary magnetic gear composed by sun gear (1), planet gears (2), ring gear (3) and carrier (4). [18]

Researchers have demonstrated that this topology of magnetic planetary gearbox ensures very high torques to size ratios and high efficiency. Despite these advantages, this design proves difficult to manufacture and implement into various applications dealing with electric machines [14].

To solve this issue and to ensure that all magnets participate in the torque transmission simultaneously, Atallah [3] developed a new design of planetary magnetic gearbox in which the planets and carrier were substituted by a single carrier gear that function as a magnetic field modulator.

In particular, it consists of an inner sun rotor with n_s permanent magnets pole pairs, an outer ring rotor with n_r pole pairs, and the intermediate carrier rotor with q ferromagnetic steel poles Figure 2.3. In this innovative model of planetary magnetic gearbox, the contact between the meshing teeth of the mechanical gears is replaced by the magnetic field generated by the inner and outer rotors and modulated by the carrier gear.

Atallah proved that this design can reach the highest torque transmission when the

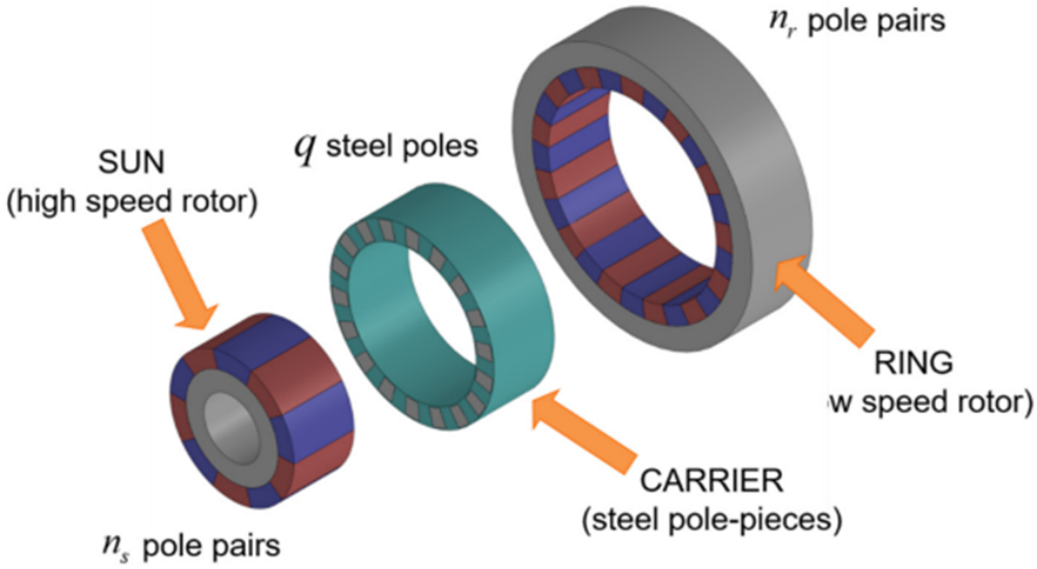

Figure 2.3: Exploded view of a Planetary Magnetic Gearbox with Sun, Carrier and Ring gears. [9]

number of ferromagnetic steel poles of the carrier is equal to the sum of the permanent magnets pole pairs of sun and ring gears [2]; in formulas:

$$q = n_s + n_r \tag{2.7}$$

The gear ratio between the inner and outer rotor, in case of stationary carrier, can be computed as:

$$G_{s/r} = \left.\frac{\omega_s - \omega_c}{\omega_r - \omega_c}\right|_{\omega_c=0} = -\frac{q - n_s}{n_s} = -\frac{n_r}{n_s} \tag{2.8}$$

In planetary magnetic gearboxes the number of permanent magnets pole pairs and the number of the ferromagnetic steel poles have the same function of the number of teeth of the mechanical gearbox. Additionally, just like what said for their mechanical counterpart, the PMG can also be used in 6 possible configurations, by fixing an element and changing input and output shafts (Table 2.2).

2.3 Working principle of the PMG

2.3.1 Overview

The working principle of the Planetary magnetic gearbox is based on the interaction between the magnetic field generated by each permanent magnet mounted on the rotors (sun gear and ring gear) and its modulation provided by the iron poles of the carrier gear. The ferromagnetic poles are arranged in such a way that the magnetic field is

Gear ratio $G_{\text{in/out}} = \omega_{\text{in}}/\omega_{\text{out}}$	**Input**	**Output**	**Fixed**
$G_{s/r} = -n_r/n_s$	sun	ring	carrier
$G_{r/s} = -n_s/n_r$	ring	sun	carrier
$G_{s/c} = q/n_s$	sun	carrier	ring
$G_{c/s} = n_s/q$	carrier	sun	ring
$G_{r/c} = -q/n_r$	carrier	ring	sun
$G_{c/r} = -n_r/q$	ring	carrier	sun

Table 2.2: Gear Ratios and Configurations of a PMG. [9]

reshaped and distorted to create a high number of space harmonics. Space harmonics are components of the magnetic field that show a periodic variation in space, each having a different number of poles and rotational speeds. It's the presence of these space harmonics that ultimately guarantees the torque transmission from the input to the output shaft of the gearbox and its functioning.

2.3.2 The role of the rotor's permanent magnet pairs

Permanent magnets are the basis of the magnetic gearbox setup: they are symmetrically spaced along the circumferential surface of the sun and ring gears and are responsible for the creation of a magnetic field. A permanent magnet is a material that keeps its magnetization properties in the absence of an external magnetic field, due to the alignment of its magnetic domains, that remain oriented in a fixed direction after being magnetised (Figure 2.4).

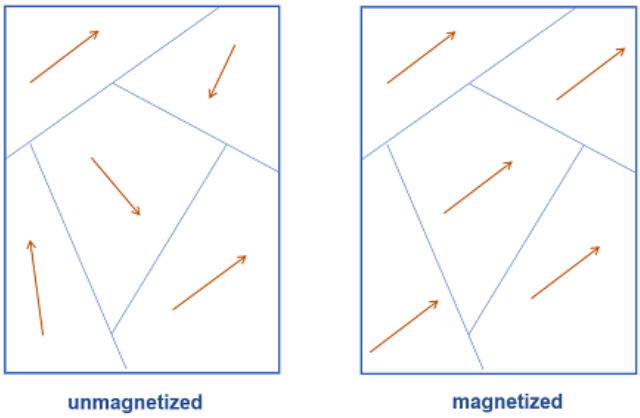

Figure 2.4: Schematic representation of unmagnetized and magnetized domains of a magnet. [27]

The magnetic field created by the permanent magnets present on the magnetic gearbox rotor can be visualised as a set of force lines coming out from the north pole and ending in the south poles of each of them. A schematic representation is shown in Figure 2.5a, while in Figure 2.5b the real field of a permanent magnet highlighted with the use of iron

dust is reported.

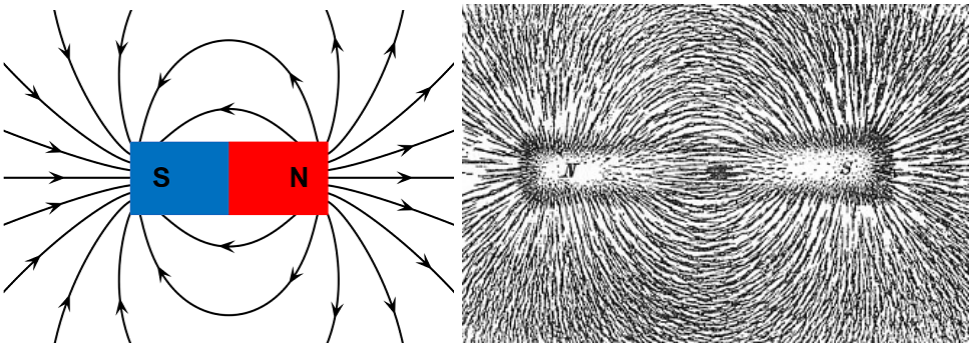

(a) (b)

Figure 2.5: Magnetic field generated by a permanent magnet. [27]

The strength and the trajectory of the field are functions of the magnet geometry and material (i.e., neodymium magnets present a stronger magnetic field).

The permanent magnet magnetic field can be computed as:

$$\mathbf{H} = \frac{\mathbf{B}}{\mu_0} - \mathbf{M} \tag{2.9}$$

where:

- H is the magnetic field: it's the cause of magnetic interactions and it represents the effects of the magnet on its surroundings;
- B is the magnetic flux density: it represents the effect of the magnetic field inside a material, taking in consideration both its permeability and the magnetic field properties.
- M is the magnetisation: it characterises the strength and the direction of the magnetic field produced by the magnet per unit volume;
- μ_0 is the free space permeability: it's related to the energy stored in a magnetic field.

The magnetic flux density allows us to have a better representation of the magnetic field in a material, as it takes into account not only the magnetic field intensity but also the response of the material surrounding the magnet, which in case of ferromagnetic materials is highly non linear.

The magnetic flux density produced by the permanent magnets of the planetary magnetic gear can be divided into a radial and a circumferential components, and both of them can be represented with the Fourier series expansion. The expression of both relationships at a radial distance r produced by either permanent magnet rotor is as follows:

$$B_r(r,\theta) = \sum_{m=1,3,5,\ldots} b_{rm}(r)\cos\left(mp(\theta - \omega_{s,r}t) + mp\theta_0\right) \tag{2.10}$$

$$B_\theta(r,\theta) = \sum_{m=1,3,5,\ldots} b_{\theta m}(r) \sin\left(mp(\theta - \omega_{s,r}t) + mp\theta_0\right) \tag{2.11}$$

where:

- m are the harmonics present in the magnetic field;
- p is the number of permanent magnets pole pairs;
- $\omega_{s,r}$ is the rotor's angular velocity;
- b_{rm} is the Fourier coefficient for the radial component of the flux density distribution;
- $b_{\theta m}$ is the Fourier coefficient for the circumferential component of the flux density distribution.

The magnetic flux density produced by the permanent magnets and its subdivision in Fourier harmonics is represented in Figure 2.6.

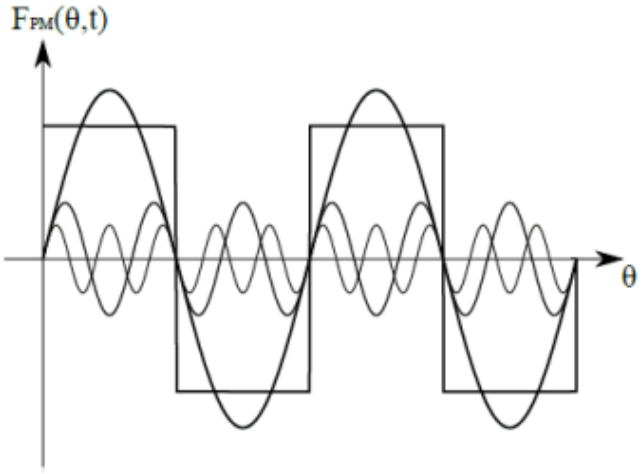

Figure 2.6: Schematic representation of the magnetic flux density and its harmonics without modulation. [34]

The distribution of the magnetic flux is affected by both the air gaps and the steel poles on the carrier. Additionally, the geometry of the magnetic flux density is not uniform, as the rotation of the rotors produce a variation in its direction and intensity.

2.3.3 The role of the carrier's iron poles

The iron poles distributed on the carrier are essential to the gearbox functioning as they allow to modulate the magnetic field created by the rotor's permanent magnets and enable torque transmission. Their interaction with the magnetic flux density inside the

system distorts and redistribute the flux in space and creates multiple space harmonics in the magnetic field, each of them representing a periodic variation of the magnetic field intensity and direction (Figure 2.7).

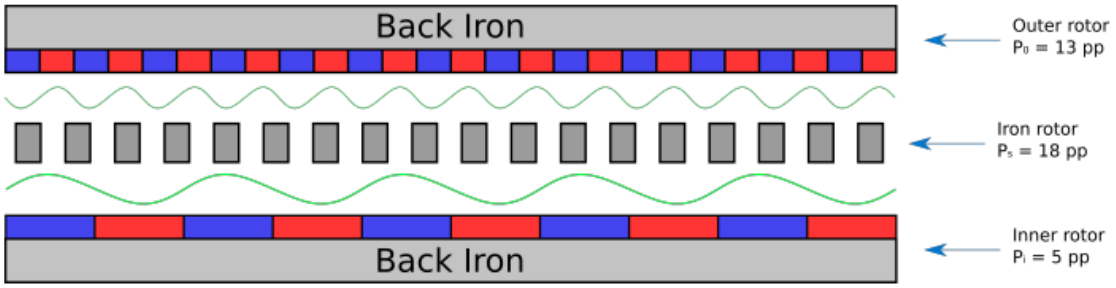

Figure 2.7: Schematic representation of the iron poles modulation of the magnetic flux density in a linear magnetic gears setup. [5]

The iron poles are made of ferromagnetic material with high permeability, making them susceptible to being magnetised and able to redirect the magnetic flux in specific directions. A relevant role is also played by the design of the spatial distribution of these ferromagnetic poles, as it's possible not only to highlight the space harmonics present in the original field, but also to create new ones.

In mathematical terms, the modulation of the magnetic flux density performed by the carrier's iron poles can be addressed by adding a term to formulas 2.10 and 2.11 that multiplies the permanent magnets contribution:

$$B_r(r,\theta) = \left(\sum_{m=1,3,5,\dots} b_{rm}(r)\cos(mp(\theta - \omega_{s,r}t) + mp\theta_0) \right) \times \left(\lambda_{r0}(r) + \sum_{j=1,2,3,\dots} \lambda_{rj}(r)\cos(jq(\theta - \omega_c t)) \right) \quad (2.12)$$

$$B_\theta(r,\theta) = \left(\sum_{m=1,3,5,\dots} b_{\theta m}(r)\sin(mp(\theta - \omega_{s,r}t) + mp\theta_0) \right) \times \left(\lambda_{\theta 0}(r) + \sum_{j=1,2,3,\dots} \lambda_{\theta j}(r)\cos(jq(\theta - \omega_c t)) \right) \quad (2.13)$$

where, on the additional terms:

- j are the new harmonics produced by the iron poles modulation;
- q is the number of the ferromagnetic poles in the carrier;

- ω_c is the carrier's speed;
- λ_{rj} is the Fourier coefficient for the modulating function of the radial component of the flux density distribution;
- $\lambda_{\theta j}$ is the Fourier coefficient for the modulating function of the circumferential component of the flux density distribution.

The results of the modulation performed by the carrier's iron poles is represented in Figure 2.8: the dashed lines show the intensity of the radial flux density in the absence of modulation, while the solid lines show the modulating results.

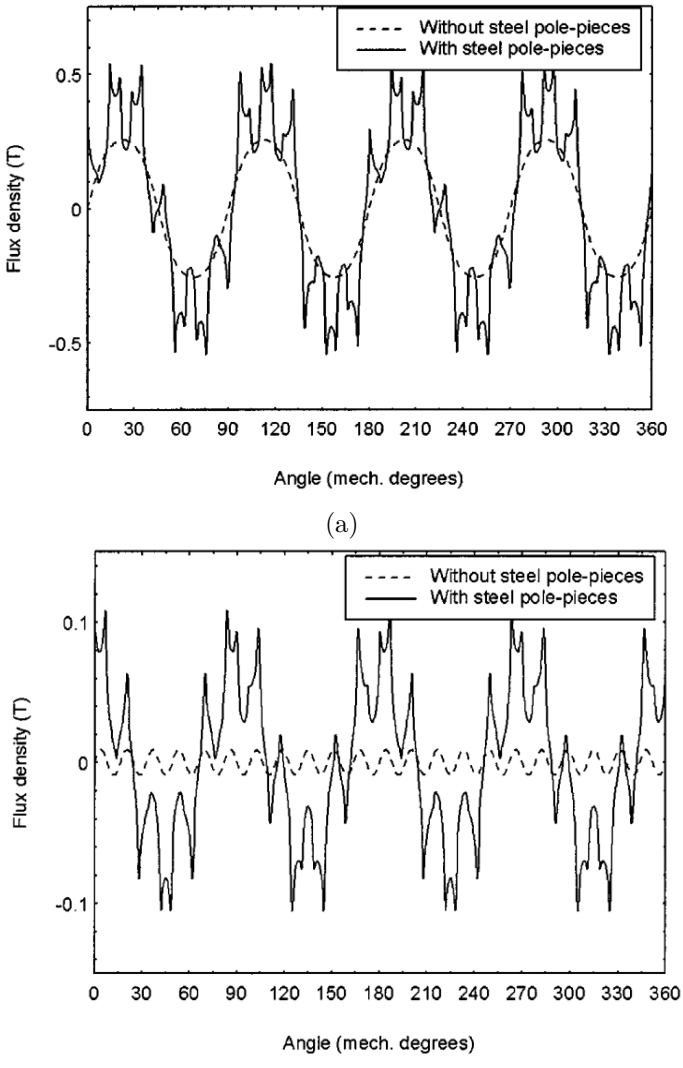

Figure 2.8: Modulation of radial flux density by ferromagnetic iron poles with high speed (a) and low speed (b) permanent magnets. [3]

As one rotor spins, the modulated magnetic flux density interacts with the opposite rotor, aligning the newly created harmonics with its permanent magnets to generate the torque required for the motion transmission.

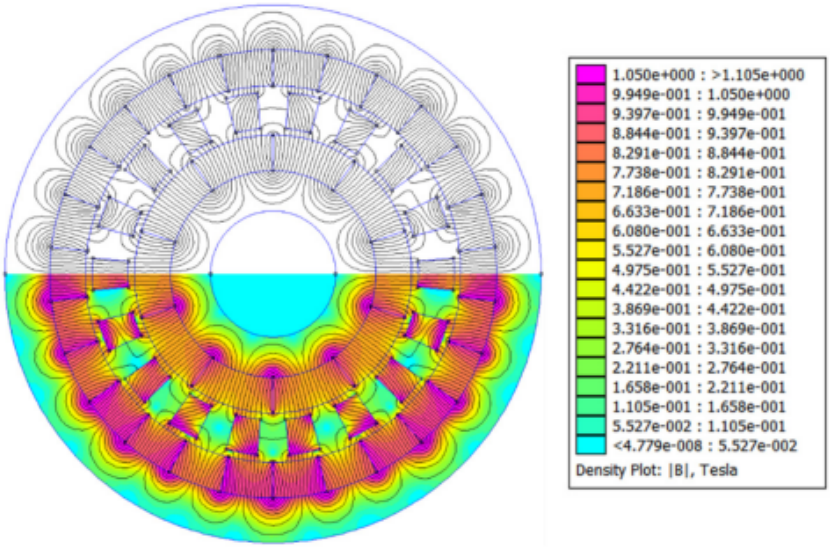

Figure 2.9: FEMM analysis of a planetary magnetic gearbox: contour plot (top) and density plot (bottom) of magnetic flux density. [9]

Design factors such as iron poles' size, shape, placement and material properties are essential for maximizing the torque transmission capability of the gearbox. Properly spacing the ferromagnetic pieces allows to have a uniform "wave" of magnetic flux that leads to a smooth transmission, minimizing at the same time power losses, noise and vibrations.

2.3.4 Magnetic Torque transmission

As previously stated, the interaction of the newly created harmonic with the rotor's magnetic field produces periodic forces and torques without the need of physical contact.

The transmitted torque could be computed recurring to the Maxwell stress tensor as follows:

$$T = \frac{L \cdot r^2}{\mu_0} \cdot \int_0^{2\pi} B_r(r,\theta) B_\theta(r,\theta) d\theta \tag{2.14}$$

As it's possible to see from the previous formulation, the torque's strength depends on the intensity of the magnetic flux density in radial and circumferential directions, computed using 2.12 and 2.13, and on the number and direction of the harmonics that are involved in the process. Lower order harmonics (present when the rotors present a lower number of permanent magnets pole pairs) contribute the most to the torque generation, while higher order harmonics (present when the rotors present a higher number of permanent magnets pole pairs) allow to have a better control and efficiency of the torque transmission

but if not properly designed and aligned could introduce power losses, torque ripple and vibrations.

Adopting the Maxwell Stress Tensor it is possible to perform a series of punctual FEM analysis to determine the values of the magnetic stiffness torques in the system, dependent to the relative angular positions of the rotors. In particular, when the ferromagnetic poles are fixed in space (i.e. the carrier gear is stationary) the transmitted torque from the input (sun) to the output (ring) gear can be represented as a function of their respective angular positions. This relationship is shown in Figure 2.10, where the left plot shows the magnetic torque transmitted between the sun and the carrier, and the right plot shows the torque transmitted between the carrier and the ring.

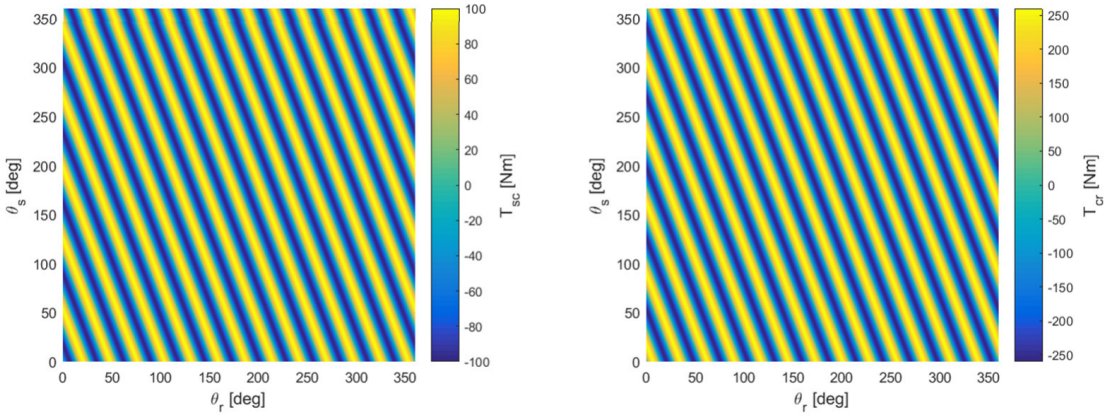

Figure 2.10: Magnetic Torque transmission between sun and carrier (left) and between carrier and ring (right) as a function of sun and ring angular positions [9]

These magnetic stiffness maps display several iso-torque lines, each with a characteristic slope that corresponds to the torque gear ratio between the input and output gears, directly related to the ratio of permanent magnet pole pairs on the two rotors. In particular, Figure 2.10 was built considering a PMG setup with a gear ratio G = -2.6 with 5 pole pairs on the sun gear and 13 on the ring gear, hence a periodic pattern in the transmitted torque is clearly visible along the y axis (associated with the sun gear angular position) and along the x axis (associated with the ring gear angular position). These periodicities can be expressed in formulas by simply dividing the entire available angular position that can be reached by the rotors, 360 degrees, by their number of permanent magnets pole pairs:

$$\tau_s = \frac{360^\circ}{n_s} = \frac{360^\circ}{5} = 72^\circ \tag{2.15}$$

$$\tau_r = \frac{360^\circ}{n_r} = \frac{360^\circ}{13} = 27.69^\circ \tag{2.16}$$

2.3.5 Torque ripple

As previously mentioned, it is vital to properly design the PMG in order to avoid major power losses, as well as torque ripples and vibrations.

In particular, torque ripple (or cogging torque) is caused by the interaction of the rotor permanent magnets with the iron poles of the carrier, and is detrimental to the gearbox performance. To minimise the influence of torque ripple on the system, a Cogging Torque Factor C_f was introduced by [37] as:

$$C_f = \frac{2n_{s,r}q}{\text{LCM}(2n_{s,r}, q)} \tag{2.17}$$

where:

- n_s , n_r are the number of permanent magnets poles on the sun and ring gears;
- q is the number of ferromagnetic pole pieces on the carrier;
- LCM stands for lowest common multiplier.

Having a lower Cogging torque factor leads to lower torque ripples in the gearbox and a smoother torque transmission. To achieve that, it's important to work with a fractional gear ratio, to maximise the LCM and minimise the cogging torque coefficient (Figure 2.11). Additionally, to achieve the lowest possible value of cogging factor of 1, it's required to design the system with an odd number of iron poles on the carrier.

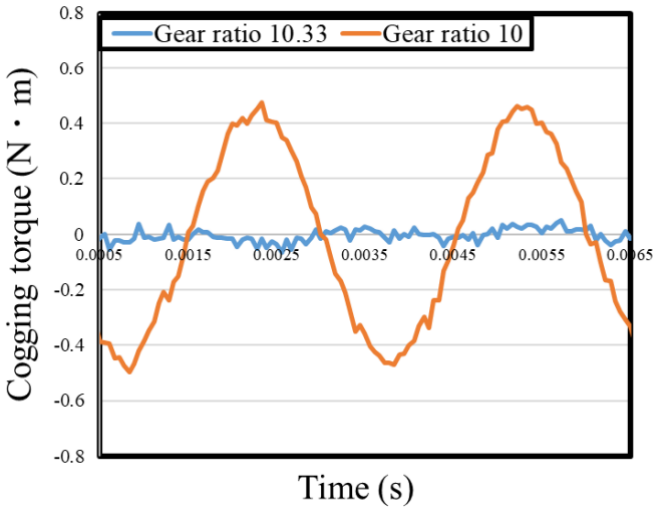

Figure 2.11: Comparison of calculated waveforms of the cogging torque with fractional and integer gear ratio. [7]

In conclusion, to have an efficient torque transfer it's necessary to carefully design the planetary magnetic gearbox choosing the most appropriate number of permanent magnets pairs and ferromagnetic poles on all the gears present in the system. Simulations and

FEM analysis can greatly help in tuning the system's parameters, ensuring the lowest torque ripples and losses, a perfect alignment of space harmonics and the highest torque transmission available at different speeds and loads.

2.4 Dynamic analysis of the PMG

To fully characterise the operation of the planetary magnetic gears, it is necessary to analyse the dynamic principle of the system. The Free Body Diagram (FBD) of the PMG system is shown in Figure 2.12.

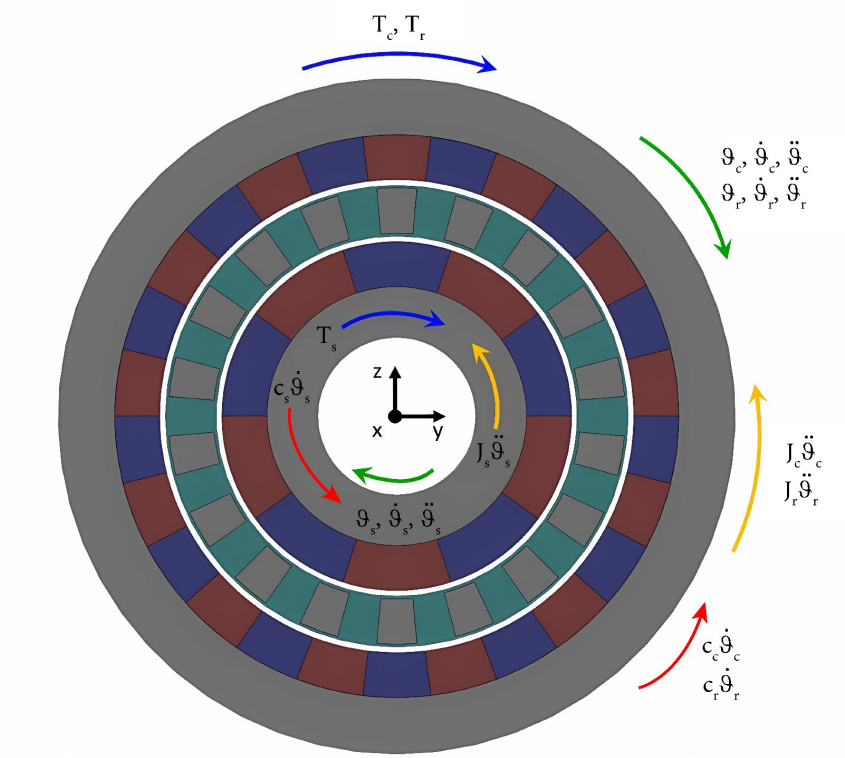

Figure 2.12: Free Body Diagram of Planetary Magnetic Gears [9]

Each rotor has one rotational degree of freedom (DOF), leading to a total of 3 DOFs in the unconstrained system. By keeping the carrier in a fixed position, the system is reduced to two dynamic DOFs: the angular position of the sun and the ring, along with their derivatives.

The operational inputs are the torques transmitted to the PMG system: $\mathbf{T_s}$, $\mathbf{T_c}$, and $\mathbf{T_r}$. The operational outputs are the angular accelerations of the system: $\ddot{\boldsymbol{\theta}}_s$, $\ddot{\boldsymbol{\theta}}_c$, and $\ddot{\boldsymbol{\theta}}_r$, which are assumed to have the same direction as their corresponding inputs.

The inertia contribution of the gears, as well as the dissipative damping terms, are considered in the analysis and are added with a discordant direction with respect to speeds and torques, while the bearing torque losses and additional losses are, in this

instance, neglected and accounted for separately.

In order to write the equations of motion of the setup it is necessary to analyse each gear singularly, highlighting the contributions of the magnetic stiffness torques created by the interaction and modulation of the carrier gear with the two other rotors (Figure 2.13).

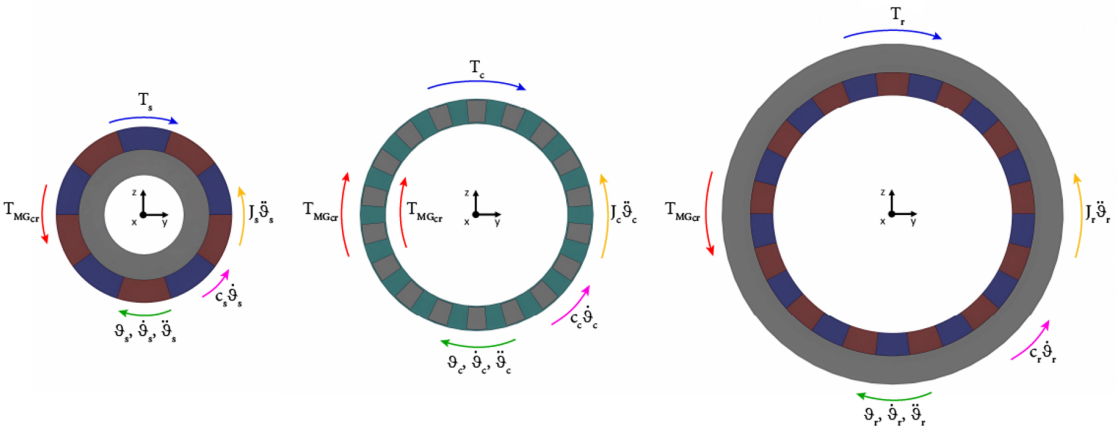

Figure 2.13: FBD of the sun (left), carrier (center) and ring (right) [9]

The equations of motion resulting from the analysis of the 3 gears FBD are the following:

$$T_s = J_s\ddot{\theta}_s + c_s\dot{\theta}_s + T_{MG_{sc}} \tag{2.18}$$

$$T_c = J_c\ddot{\theta}_c + c_c\dot{\theta}_c - T_{MG_{sc}} - T_{MG_{cr}} \tag{2.19}$$

$$T_r = J_r\ddot{\theta}_r + c_r\dot{\theta}_r + T_{MG_{cr}} \tag{2.20}$$

where:

- J_s, J_c, J_r are the inertia contributions of the three gears;
- c_s, c_c, c_r are the dissipative contributes of the three gears;
- ω_s, ω_c, ω_r and $\dot{\omega}_s$, $\dot{\omega}_c$, $\dot{\omega}_r$ are respectively the angular velocities and angular accelerations of the three gears;
- T_MG_sc and T_MG_cr are the magnetic torques coming from the magnetic interaction of the three gears, respectively sun and carrier and carrier and ring. They represent the magnetic stiffness coupling of the system;
- T_s, T_c and T_r are the torques that are transmitted mechanically to the three gears. Considering a fixed carrier, i.e. $\omega_c = 0$, and considering the sun gear as the input of the PMG and connected to a motor granting a torque T_s, T_r will be the resistant torque capable of being transmitted by the output ring rotor.

The Equations of Motion can be rearranged to highlight the primary operational outputs and expressed in matrix form as follows:

$$\begin{bmatrix} J_s \\ J_c \\ J_r \end{bmatrix} \begin{Bmatrix} \ddot{\theta}_s \\ \ddot{\theta}_c \\ \ddot{\theta}_r \end{Bmatrix} = \begin{Bmatrix} T_s \\ T_c \\ T_r \end{Bmatrix} - \begin{bmatrix} c_s \\ c_c \\ c_r \end{bmatrix} \begin{Bmatrix} \dot{\theta}_s \\ \dot{\theta}_c \\ \dot{\theta}_r \end{Bmatrix} - \begin{Bmatrix} T_{MG_{sc}} \\ -T_{MG_{sc}} - T_{MG_{cr}} \\ T_{MG_{cr}} \end{Bmatrix} \tag{2.21}$$

Chapter 3

PMG Prototype Description

In chapter 2, the working principle of the PMG was broadly discussed, along with the definition of the dynamic behaviour of the system being analysed and its overall theoretical structure.

In this chapter, there is a shift from purely theoretical considerations to the study of the physical prototype that is being experimentally tested. This prototype is fundamental to link the theoretical knowledge, physical results and simulated analysis to validate the behaviour of magnetic gears under operating conditions, analysing their potential for future industrial applications. The main goal is to broadly characterise the architecture and realisation of the experimental test bench that has been previously developed in the laboratories of Politecnico di Torino. The main elements that will be analysed are the magnetic gearbox itself along with all the main peripherals that are needed to ensure the correct and reliable operation of the system, as well as the needed softwares necessary to capture the test data.

Section 1 will describe the magnetic gearbox, focusing on its internal components, their structural arrangement and the design choices adopted. In section 2, the main elements of the test bench will be analysed, such as the chosen motors to provide power to the prototype, the sensors needed to monitor torques and speeds under operating conditions, and the electric panel that connects the motors to the grid and provides safety measures to the system. Finally, the data acquisition system and the software adopted for motor control and data handling are investigated in section 3.

These sections will serve as a base for a comprehensive overview of the test bench experimental analysis that will be presented in the following chapter.

3.1 Planetary Magnetic Gearbox Prototype

3.1.1 General Overview and Design Parameters

The coaxial Planetary Magnetic Gearbox (PMG) used in this work is a previously developed prototype, designed and constructed as part of earlier research activities at the Politecnico di Torino. Its development aimed to validate the theoretical modelling and simulations carried out in the earlier stages of the research in a laboratory setting through

experimental demonstration. In the present thesis, the prototype is used as an experimental platform to conduct dynamic tests in order to characterise the data that will be needed to build a Dynamic Model of the system.

The PMG prototype consists of two sets of coaxial magnetic gear stages, with each stage designed with a different transmission ratio. Each stage is made up by a sun rotor and a ring rotor, both equipped with Neodynium Iron Boron (NdFeB) permanent magnets pole pairs on their surfaces. In particular, these magnets are partially embedded in the steel yokes to improve their mechanical stability and avoid displacements in case of high torque operating conditions, as shown in Figure 3.1. The magnetic interaction, and consequently the torque transmission, is guaranteed by the correct positioning and alignment of the ferromagnetic iron pole pieces mounted on an axially movable carrier with one of the rotor stages' magnet pairs. In addition to that, an axial gap between the two stages was designed to allow operations under neutral conditions, disengaging the input and output rotors and removing magnetic coupling between the two, making it possible to isolate and measure the mechanical losses in the system due to bearings and structural damping. The total configuration of the gearbox provides reliable magnetic interactions while also keeping a balance between magnetic performances and structural stability.

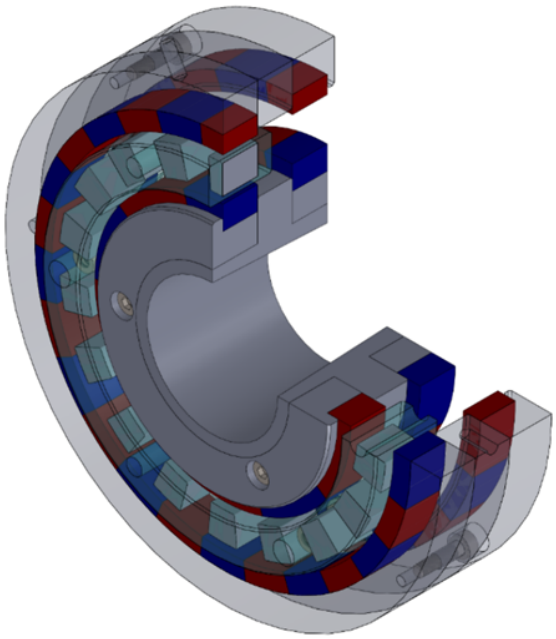

Figure 3.1: PMG prototype: total view of the two stages

The magnetic pole configuration is of fundamental importance for the PMG's functionality. In the first gear stage, the sun rotor is equipped with 5 pole pairs and the ring rotor with 13, while in the second gear stage, the sun and ring are equipped with 7 and 11 pole pairs respectively (Figure 3.2).

This configuration guarantees a consistent total of 18 magnetic pole pairs per stage, corresponding to the number of ferromagnetic pole pieces in the carrier (Figure 3.3), as

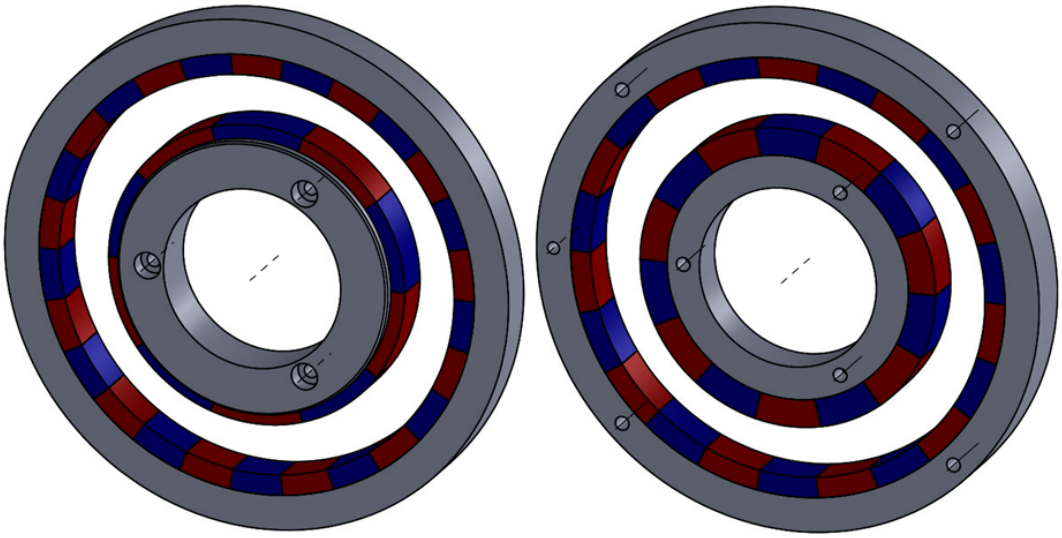

Figure 3.2: View of the sun and ring rotors in the first stage (left) and in the second stage (right)

previously discussed in Equation 2.7. This consistency allows for a proper flux modulation by the carrier, regardless of which stage is engaged in operation.

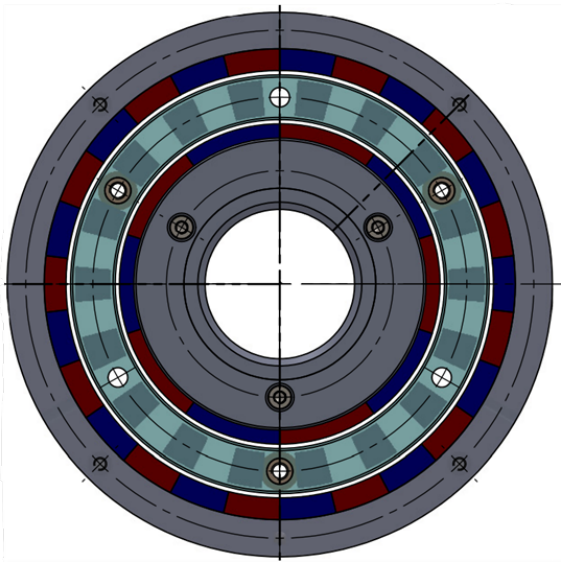

Figure 3.3: Frontal View of the carrier engaged with the first stage

The main design parameters are summarized in Table 3.1. These include geometrical dimensions of magnets, steel poles and structural components, as well as transmission ratios and maximum transmissible torques in both available gear stages.

Parameter	**Value**	**Unit**
Sun PM thickness - $th_{PM,s}$	6.75	mm
Ring PM thickness - $th_{PM,r}$	5	mm
Steel poles thickness th_{poles}	8.25	mm
Air gap	2	mm
Gear external radius - R_{ext}	62.5	mm
Gear axial length - L	10	mm
Sun PMs pole pairs - n_s	[5 7]	
Ring PMs pole pairs - n_r	[13 11]	
Carrier steel poles - q	18	
Gear transmission ratio - τ_{slr}	[-2.6 -1.57]	
Design Results	**Value**	**Unit**
Torque inner rotor - (sun) T_{sc}	[2.57 3.46]	Nm
Torque outer rotor - (ring) T_{cr}	[6.68 5.43]	Nm
Torque carrier - T_c	[-9.25 -8.89]	Nm
Weight - m_{PMG}	0.66	kg
Torque density - T_ρ	[3.89 5.24]	Nm/kg

Table 3.1: Parameters and Results of the magnetic gearbox design

3.1.2 Assembly

The PMG prototype was assembled with a focus on preserving geometric precision and alignment while also providing functional modularity to the system. The total assembly is divided into 3 main elements: an active part, a passive part and an actuation system for gear shifting (Figure 3.4).

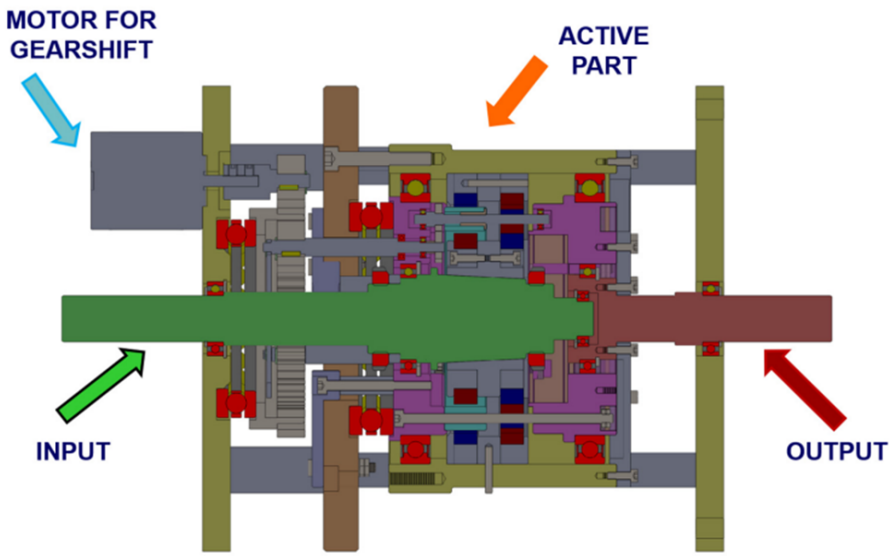

Figure 3.4: 2D CAD representation of the PMG assembly

The active element is made up by the two stages that have been described in the previous section. The pre-assembled rotors, each having permanent magnets pairs glued to their respective yokes (Figure 3.5), were secured into position: the inner sun rotors were connected to the input shaft through a conical coupling and secured in position by locknuts to prevent axial slippage, while the outer ring rotors were, instead, secured with screws to the external housing and properly aligned to the inner rotors (Figure 3.6).

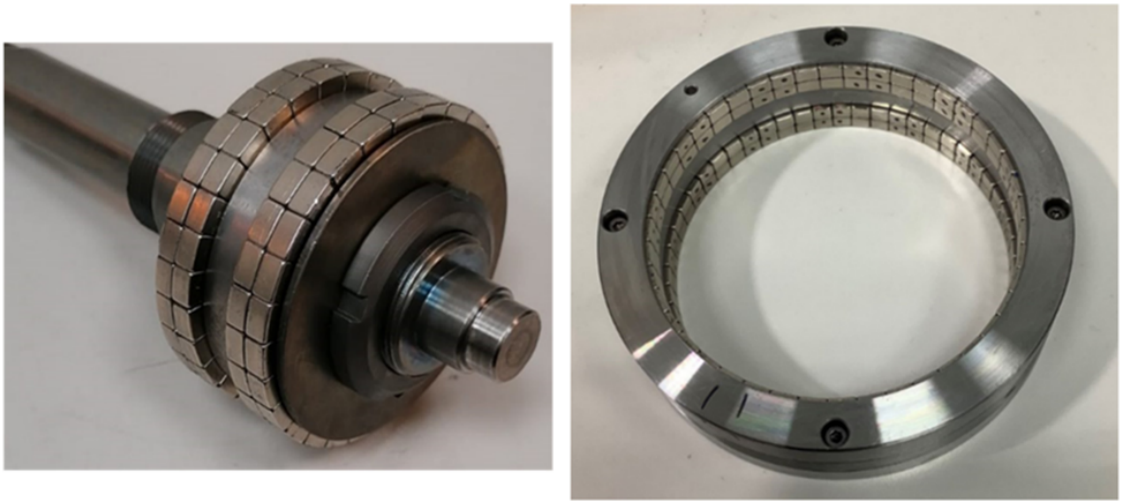

Figure 3.5: Assembly of the inner (left) and outer (right) rotors of the PMG

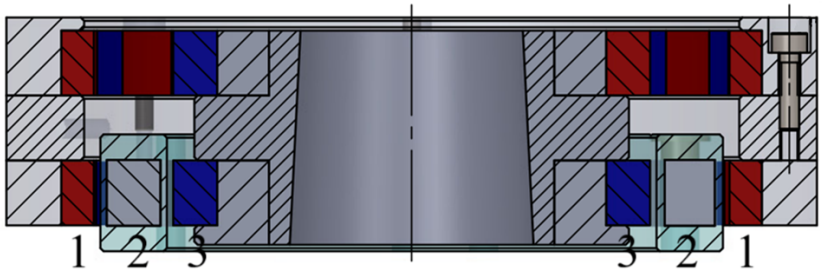

Figure 3.6: Assembly of the active part of the PMG engaged in the first gear: ring rotor (1), carrier stator (2), sun rotor (3)

In the gap between inner and outer rotors, an axially movable resin carrier housing 18 ferromagnetic pieces was inserted. Once assembled, this active element is secured onto the passive structure of the prototype (Figure 3.7).

The rotation is transmitted from the inner shaft to the sun gears, from the sun gears to the ring gear of the engaged stage (i.e., the stage in which the carrier is currently sitting), and from the ring gear to the outer shaft. Additionally, the carrier is connected to a step motor that allows its axial movement for performing gear shifting operations. For what concerns the research activity performed in this thesis, the research focused on the first gear of the prototype, and the step motor was not been utilised.

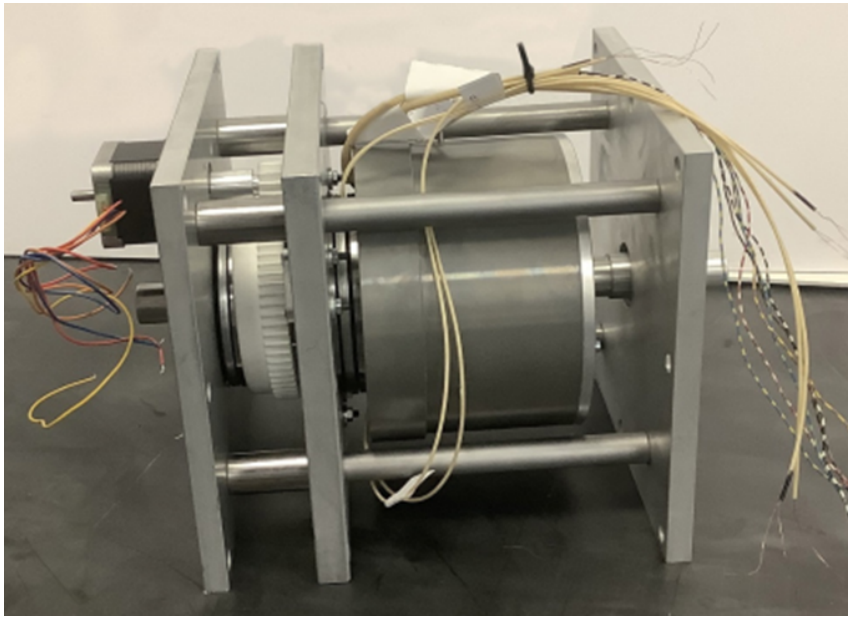

Figure 3.7: Total Assembly of the PMG prototype

3.1.3 Bearings

Great attention was given to the selection and placement of bearings. The PMG prototype is supported by a total of seven radial ball bearings, positioned to ensure the proper alignment of the shafts and to minimize mechanical friction losses (Figure 3.8). These bearings vary in role and size and are distributed symmetrically along the PMG in order to keep structural balance and rigidity during working conditions.

Table 3.2 lists the bearings used. Their choice was influenced by space constraints, rotational speed requirements, and the need to minimize mechanical losses during tests. Originally, a different set of bearings was installed on the system, however, due to unexpectedly high mechanical losses, a redesign was performed, and this newer and more efficient set was implemented.

Number	Denomination
1, 7	W 61804-2Z
2, 6	W 61807-2Z
3	W 61802-2Z
4, 5	61820-2RZ

Table 3.2: Bearing SKF Identification Model.

Bearings 1 and 7 are mounted between the inner and outer shafts and the fixed outer frame, providing end support and constraining along the axial direction. Bearings 2 and 6 are positioned to support both the inner and outer shaft relative to the carrier, ensuring proper alignment during operations. The largest pair of bearings, 4 and 5, is dedicated

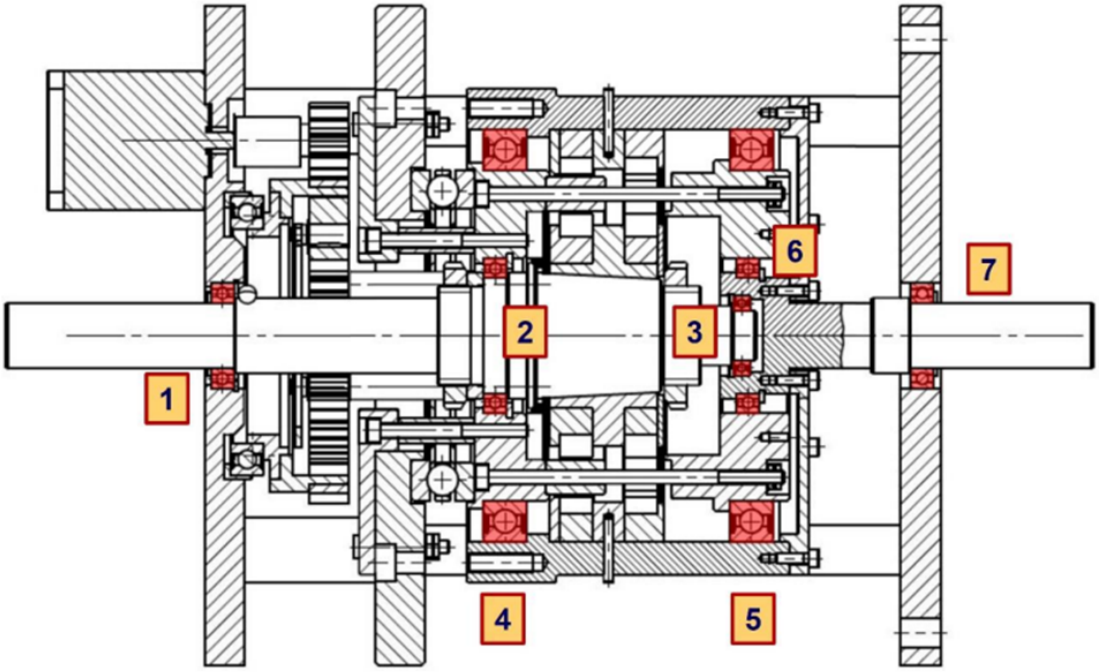

Figure 3.8: Bearings Designation

to supporting the rotation of the ring with respect to the carrier. Finally, bearing 3, the smallest bearing used in the assembly, allows relative motion between the inner and outer shafts.

While the prototype is primarily tested in the carrier fixed mode, its bearing architecture also allows different operating conditions, such as with a fixed ring rotor and movable carrier. In this case, an extra axial bearing allows a relative motion of the carrier with respect to the housing. However, for the tests conducted for this thesis, it is neglected.

3.2 Test Bench Description

The experimental analysis performed on the coaxial Planetary Magnetic Gearbox prototype was carried out through a dedicated test bench, specifically designed for the control and monitoring of mechanical and electromagnetic quantities, such as torque, speeds, and magnetic flux. The test bench integrates high performance actuators, precise sensors and a custom built electric panel that allows safe and reliable operating conditions during experimental tests.

In particular, this test rig is completely symmetrical with respect to the magnetic gearbox, as shown in Figure 3.9. Starting from the PMG and proceeding alongside both directions, there is a first elastic joint that allows to connect the respective gearbox shaft to a torque sensor, which is capable of measuring rotational speed as well. The torquemeter is then connected to the shaft coming out from the motor. In total, two brushless electric motors are installed on the bench, each of which can be controlled

separately and supplied with power, thus allowing the gearbox to be tested as both a speed reducer and speed multiplier, as well as in neutral conditions.

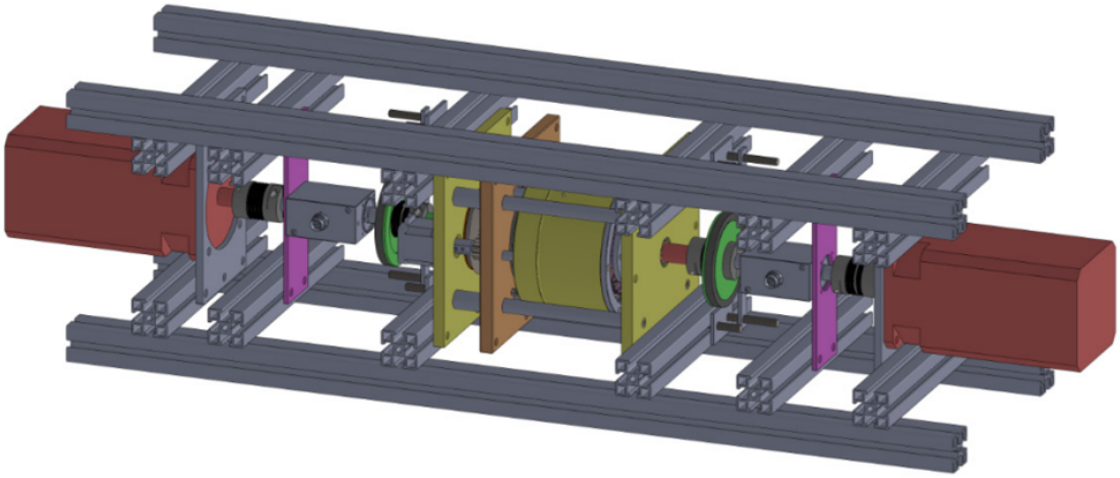

Figure 3.9: 3D model of the test bench.

3.2.1 Actuators

The actuation of the Planetary Magnetic Gearbox is achieved through two identical brushless DC motors manufactured by Servotecnica, precisely the SVTM A 03-11.5-107 model (Figure 3.10).

Figure 3.10: Servotecnica SVTM A Series Brushless Motors.

The choice of these motors was based on their ability to deliver a consistent torque above the gearbox requirement, while also being able to keep good accuracy and control during dynamic operations. The SVTM A series is also particularly adequate for laboratory applications due to its high torque to size ratio enabled by internal neodymium

permanent magnets. The most important parameters of these actuators are summed up in Table 3.3.

Parameter	**Value**	**Unit**
Nominal Voltage	560	V_{DC}
Continuous Stall Torque	11.5	Nm
Continuous Stall Current	6.85	A_{rms}
Nominal Torque	9.3	Nm
Nominal Current	5.54	A_{rms}
Nominal Speed	2800	rpm
Peak Torque	30	Nm
Peak Current	21	A_{rms}
Torque Constant	1.68	Nm/A_{rms}
BEMF Constant	107	$V_{rms}/krpm$
Resistance	1.86	Ohm
Inductance	12.8	mH
Rotor Inertia	10.8	$kgcm^2$

Table 3.3: SVTM A 03-11.5-107 main specifications.

The symmetrical assembly of the test bench allows either motor to function as a driver or as a load, depending on the operating condition being tested. Usually, one motor operates in speed control, while the other works in torque control to operate as the resisting load, making it possible to simulate a real scenario. Additionally, each motor integrates a Hall effect incremental encoder that supplies real-time angular position feedback of the rotor position and makes it possible to control speed and torque with high fidelity and accuracy.

3.2.2 Sensors

The accurate and precise measurement of torque and angular speed is essential for the correct characterisation of the dynamic and magnetic performances of the PMG prototype. To that end, the test bench is equipped with two transducers and two incremental encoders to measure torque and speed, respectively, as well as test coils for measuring magnetic flux intensity.

Torque Transducers

Torque measurement is handled by two HBM T21WN torque transducers, shown in Figure 3.11, one on each shaft connecting the motors to the PMG. These sensors provide both measurements in voltage and digital frequency, however, the latter is the preferred option for data acquisition as it's less affected by noise and signal degradation.

The transducers are calibrated for different nominal torques:

- Sun shaft transducer: 5 Nm

- Ring shaft transducer: 10 Nm

This differentiation comes from the torque asymmetry resulting from the gear ratio of the engaged stage of the PMG: in speed reducer conditions, assuming first gear operations, the torque on the ring side is 2.6 times higher than that on the sun side.

Figure 3.11: HBM T21WN Torque Transducer.

The main characteristics of these transducers are summed up in Table 3.4. To highlight the most significant, they offer a small deviation from linear conditions and angular displacement under load, as well as good frequency resolution.

Parameter	**Value**	**Unit**
Precision Class	0.2	
Nominal Torque	[5 10]	Nm
Nominal Speed	19000	rpm
Non Linearity	$<\pm 0.1$	%
Frequency Output	$[5 \div 15]$	kHz
Null Torque Frequency Output	10	kHz
Frequency Resolution	0.19	Hz
Voltage Output	$[-10 \div 10]$	V
Null Torque Voltage Output	0	V
Voltage Resolution	0.38	mV
Sensitivity Tolerance	$\pm$ 0.2	%

Table 3.4: HBM T21WN torque transducers main specifications.

Rotational Encoders

The rotational speed of the input and output shafts of the PMG is captured by two Renishaw LM10 incremental magnetic encoders, installed one on each shaft. These encoders are made up of two different elements: a contactless readhead and a magnetic ring to be installed on the shaft whose rotational speed is to be measured, as shown in Figure 3.12.

The magnetic ring has evenly spaced magnetic poles installed on it, which interacting with the readhead as the shaft rotates, enabling the speed measurement in the form of

Figure 3.12: Rotational Speed Encoder: Renishaw LM10D01-15 readhead (1) and RLS MR02D01-02 magnetic ring (2).

a digital output. The resulting digital output comes in the form of three differential signals (and channels), allowing reduced electromagnetic noise and ensuring good signal integrity. In particular, one of these signals (i.e., the Z channel) provides a reference pulse once per rotation, which is essential for synchronization purposes and to establish the absolute reference position.

The non-contact working mechanism of this encoder prevents mechanical tear and wear, allowing for a consistent signal monitoring over time. The main characteristics of these encoders are summed up in Table 3.5.

Parameter	**Value**	**Unit**
Resolution	1280	*ppr*
Maximum Frequency	60	kHz
Number of Magnetic Poles	160	
Coefficient of Interpolation	32	
Response Time	<10	µs

Table 3.5: Renishaw LM10D01-15 speed encoder main specifications.

These encoders are installed directly on the shafts, putting particular attention to the proper concentricity and gap between the magnetic ring and the readhead, to make sure that when the operational condition reaches higher speeds, the system is stable and there is no rupture.

Magnetic Flux Sensing

A direct measurement of the magnetic field inside the Planetary Magnetic Gearbox is not possible due to limited access to the rotating gears. To solve this problem, the test bench uses a set of custom made electromagnetic sensing coils mounted on the ferromagnetic pole pieces installed on the carrier gear, as shown in Figure 3.13. These coils allow for an indirect measurement of the magnetic field distribution through the electromotive force (EMF) induced by the variation of the magnetic flux during operating conditions.

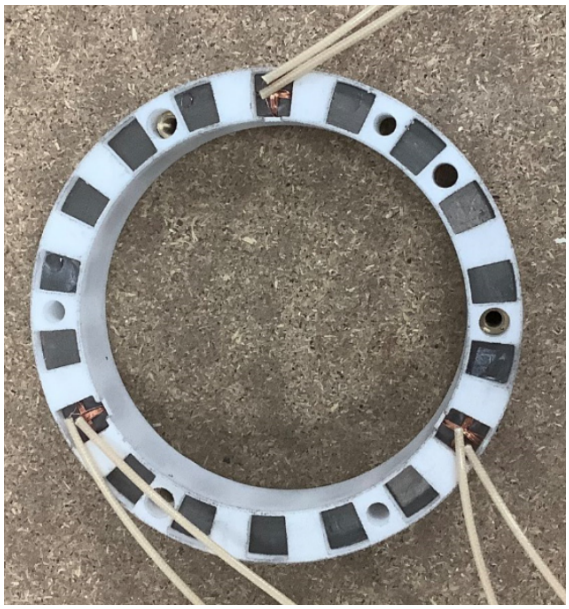

Figure 3.13: Coil windings for magnetic flux sensing installed on the carrier gear.

A total of six coils were installed, of which three are suited for the measurement of the tangential component of the magnetic field, while the remaining three are aligned to measure its radial component. Additionally, these two sets of coils are equidistantly positioned, 120° apart from each other, enabling the phase analysis of the flux. As the PMG rotates, the interaction between the permanent magnets pairs mounted on the inner and outer rotors and the modulation provided by the iron poles on the carrier generates a magnetic flux variable in time, which induces a voltage across each coil according to Faraday-Neumann-Lenz's Law:

$$V(t) = -N\frac{d\Phi(t)}{dt} \tag{3.1}$$

where $V(t)$ is the induced voltage, N is the number of turns in the coil and $\Phi(t)$ is the magnetic flux. Assuming that the Magnetic Flux Density B is uniform and parallel to the coils' surface, it can be related to the magnetic flux by:

$$\Phi = \int_S \mathbf{B} \cdot d\mathbf{A} \longrightarrow B = \frac{\Phi}{A} \tag{3.2}$$

it is possible to compute B by linking it to the voltage signal acquired by each set of coils:

$$|B| = \frac{1}{A}\int_0^T \frac{V(t)}{N}dt \tag{3.3}$$

The coils were designed using the parameters shown in Table 3.6.

Parameter	**Value**	**Unit**
Angular Distance	120	°
Winding's Number N	18	
Wire Resistance R	17	Ω
Tangential cross sectional area A_T	73.59	mm^2
Radial cross sectional area A_R	65.81	mm^2

Table 3.6: EMF coils Specifications.

3.2.3 Electric Panel

A central component of the test bench is the electric panel, which is responsible for all the power distribution, safety, and control systems that are required for testing the PMG prototype. It was designed to support the motors, sensors, data acquisition systems, and ancillary components to ensure the correct operation during the experimental tests. Its configuration is shown in Figure 3.14.

Figure 3.14: Electric Panel.

The electric panel is connected to the grid by a three-phase 400V AC line. From this main input, power is tuned and distributed to reach all the components in form of five different voltage levels:

- 400V AC: input to the rectifier unit, which converts the 400V AC into a 540V DC.
- 540V DC: output from the rectifier to supply the motor inverter and the motor control boards. These modules are designed to communicate over an EtherCAT connection with a NI CompactRio 9045, which allows to control the motor commands in real time.
- 230V AC: intermediate tension level used by AC/DC converters, in particular 230V AC to 24V DC and 230V AC to 5V DC.
- 24V DC: powers the stepper motor, torque sensors, CompactRIO controller, inverter auxiliaries, and cooling systems.
- 5V DC: supplies the magnetic encoders.

Each of these five branches safety is ensured by the use of fuse disconnectors and governed by an automatic circuit breaker, which will act in case of overload or short circuit.

Aside from the internal circuits, the electric panel is also equipped with a front user panel, which offers an accessible interface for the users. The front panel is shown in Figure 3.15 and it includes:

- a voltage indicator light confirming the system's power on status;
- a selector switch to enable the motor inverter;
- an emergency stop button, which immediately triggers the inverter's safe shutdown state;
- an Ethernet port for PC to CompactRIO communication;
- a stepper driver on/off switch;
- manual controls for the gear shift actuator;
- two AC sockets for utilities.

3.3 Data Acquisition System

In order to perform experimental evaluations of the planetary magnetic gearbox performance, it is necessary to properly implement the data acquisition system to acquire, process, synchronise, and control data from multiple sources in real time, while also ensuring safety measures in case of component malfunction. To this aim, a National Instruments (NI) hardware and software environment was chosen. For what concerns the hardware,

Figure 3.15: User Interface of the electric panel.

a CompactRIO 9045 platform was chosen, which is supported by the use of LabVIEW software, which allows for the user control of torque and speed related quantities of the test bench, as well as fault management.

3.3.1 Data Acquisition Hardware

A CompactRIO 9045 hardware configuration was chosen and configured to host multiple data acquisition modules that communicate in real time with sensors, actuators, and safety devices installed on the test bench (Figure 3.16).

Figure 3.16: NI CompactRIO 9045.

This configuration can be connected via Ethernet cable to the user's PC and programmed using LabVIEW software. The acquisition system must be able to manage three different types of signals:

- Digital frequency signals from torque sensors and encoders.
- Analogue voltage signals from magnetic flux test coils.
- Digital logic signals from on/off switches and emergency buttons.

To this end, three distinct modules were installed for the data acquisition systems, one for each signal type (Figure 3.17):

- NI 9411: Digital differential input for frequency based signals from torque sensors and encoders.
- NI 9205: Analogue input for induced voltages coming from magnetic flux coils.
- NI 9421: Digital input for logic signals (emergency stop, on/off switches).

Figure 3.17: National Instruments acquisition boards: NI 9411 (left), NI 9205 (center), NI 9421 (right)

The main characteristics of these modules are summarized in Table 3.7.

DAQ Module	Signal Type	Signal Range	Channels	Update Rate
NI 9411	Digital	±5V	6	500 ns
NI 9205	Analogue	±10V	37	250kS/s
NI 9421	Digital	12V,24V	8	100 µs

Table 3.7: NI DAQ modules specifications.

The data acquired from the sensors is acquired by these modules using a buffered counter strategy, allowing signals to be temporarily stored before transferring them to the PC. This allows for a faster and more precise acquisition, especially when dealing with a high frequency signal. This data is then synchronised by using a shared sample clock provided by the NI 9205 module, fundamental operation to guarantee that all signals are aligned in time. The signal synchronisation is necessary to correctly compare signals and properly address their frequency contents during post processing operations.

3.3.2 Data Acquisition Software

The entire test bench is operated and monitored by the use of LabVIEW, a programming language software developed by National Instruments. This software allows direct communication with the CompactRIO hardware and integrates all its real time motor controlling, signal acquisition and data processing functionalities by adopting a graphical interface that allows for parallel processing.

Programs made in LabVIEW software environment are called Virtual Instruments (VIs). Each VI is made up of two main components:

- the Front Panel, the user interface of the program, that is usually equipped with buttons, indicators, plots, and input fields;
- the Block Diagram, the programming interface of the program, which contains the graphical code needed to run the VI.

Two principal VIs were previously developed to manage the tasks of motor control and data acquisition: the Main Control VI and the Synchronous Acquisition VI.

Main Control VI

The Main VI allows the user to control both motors in either speed or torque control, by interfacing with the inverter positioned in the electric panel by the use of a real time EtherCAT protocol.

The front panel of the Main VI, shown in Figure 3.18, is structured into multiple sections, each having different roles, that are:

- emergency and reset controls;
- status feedback and fault diagnostics;
- input fields for torque and speed control references;
- real time graphical plots of motor feedback signals.

The respective block diagram, shown in Figure 3.19, simply reflects this logic by the adoption of parallel loops for user input handling, error checking, EtherCAT transmission, and motor response monitoring.

Synchronous Acquisition VI

The Synchronous Acquisition VI is, instead, responsible for acquiring the digital signals coming from the torque transducers and incremental encoders. As the name suggests, it is mandatory that all signals are acquired synchronously, by referring to the shared sample clock present on the NI 9205.

This user interface of this VI is shown in Figure 3.20 and is made up of:

- input fields for sampling rate, acquisition window duration, and channel selection;
- graphical representation of the torque and speed signals over time;

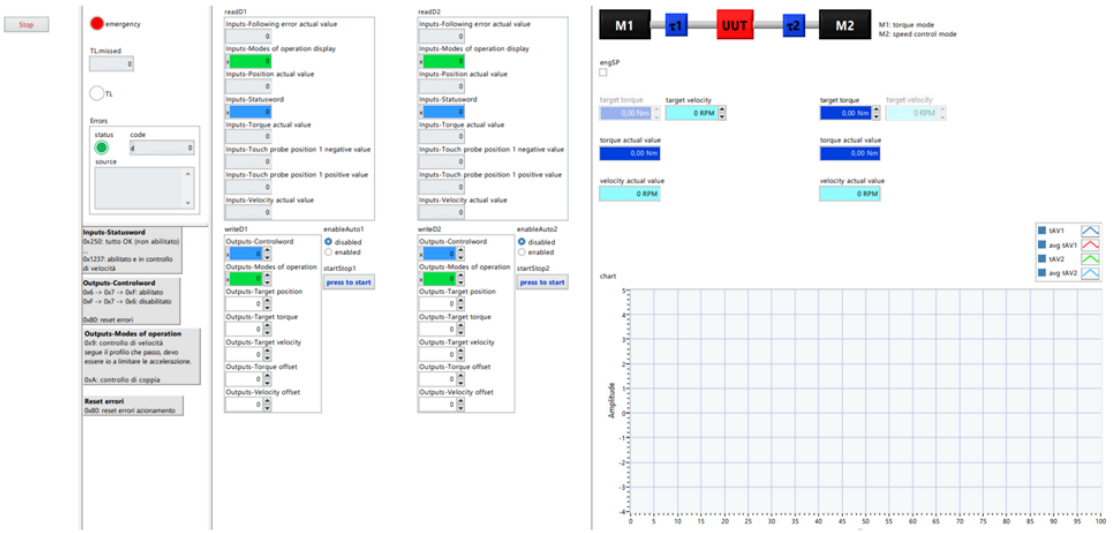

Figure 3.18: Front panel of the Main Control VI.

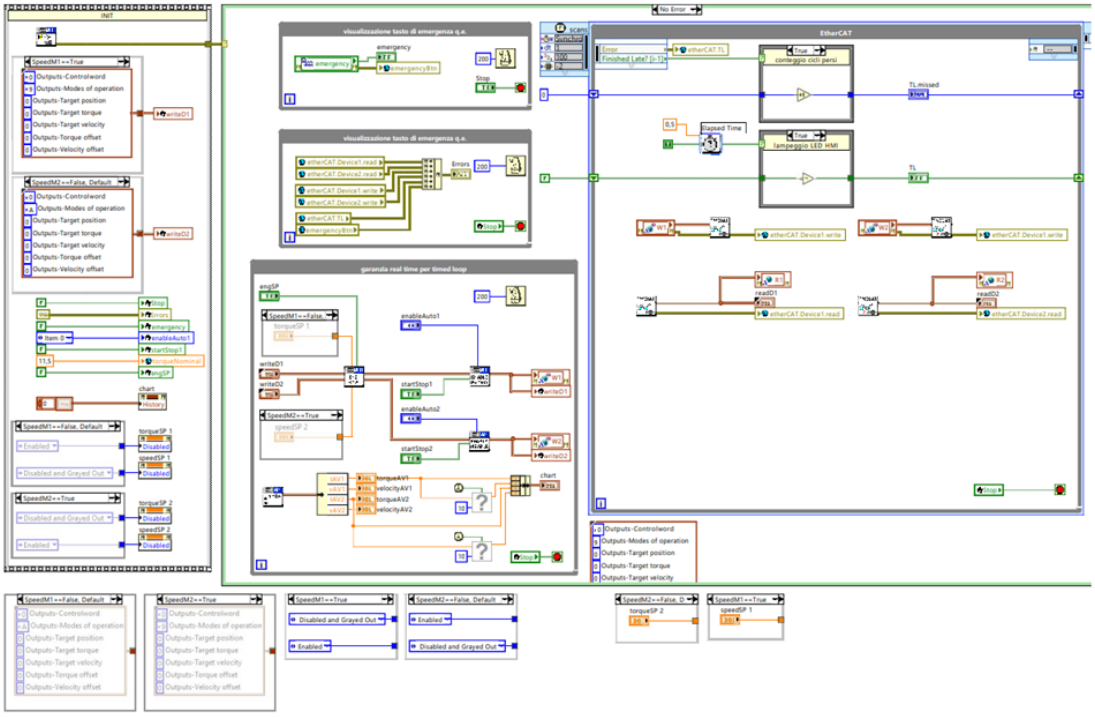

Figure 3.19: Block diagram of the Main Control VI.

- Real time FFT of the signals.

This VI supports both time domain and frequency domain analysis, which are important for studying the dynamic performance of the PMG and finding eventual resonance

Figure 3.20: Front panel of the Synchronous Acquisition VI.

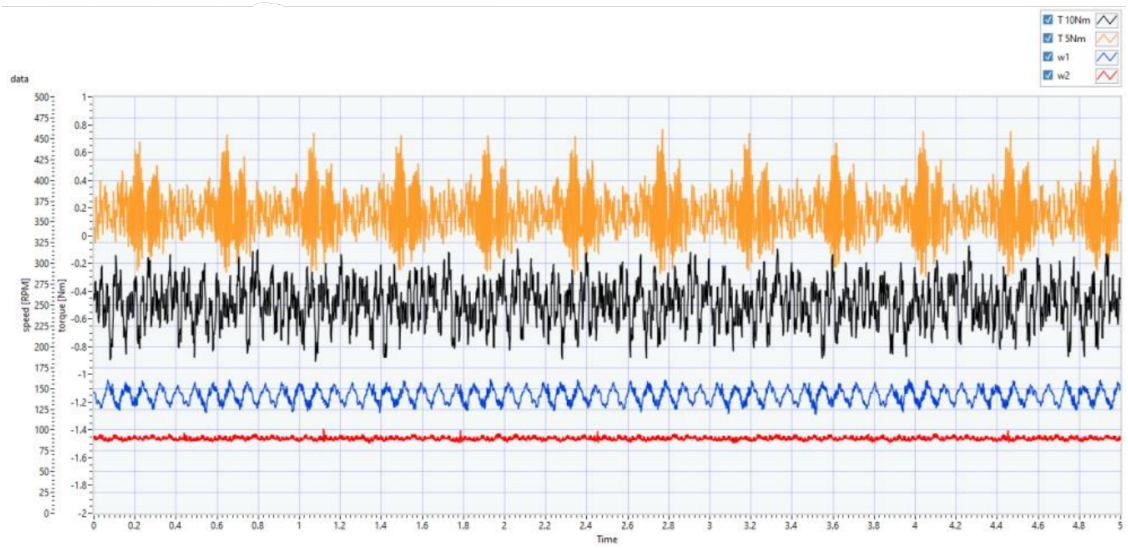

Figure 3.21: Zoom of the torque and speed signals plot of the Synchronous Acquisition VI under operating conditions.

peaks.

Together, these two VIs form the core of the software environment that enables safe, flexible, and high resolution testing of the PMG prototype.

Chapter 4

Experimental Tests

In Chapter 3, the physical prototype of the Planetary Magnetic Gearbox was described, together with the main components of the test bench that was developed to perform its experimental validation. The internal architecture of the gearbox, together with the selected actuators, sensors, and supporting hardware and software systems for data acquisition, was presented as the essential elements that would enable a consistent testing setup.

This chapter focuses on the actual experimental testing carried out on the PMG prototype. The main goal is to describe the testing procedures adopted to characterize the losses and the performance of the PMG. Additionally, a comparison with previous tests performed on the same prototype is discussed, pointing out their limitations and the improvements introduced with the new set of tests, with the aim to obtain better physical consistency and accuracy.

In section 1, a general overview of the experimental tests is given, along with the definition of the main objectives and methodology, while in section 2, the main data processing operations are discussed. In section 3, the neutral testing environment will be analysed. The main objective of the neutral tests is the quantification of the prototype's mechanical losses. The results obtained from the previous set of tests are shown, pointing out their limitations and physical inconsistencies. Then a new set of neutral tests is performed with some improvements, and compared to the previous one. The potential application of a corrective factor to take into consideration the residual magnetic losses that may be present in neutral testing conditions is also discussed. Section 4 focuses instead on the engaged tests, whose aim is the analysis of the gearbox performances. Following the same procedure as before, the results of the older sets of tests are discussed, by taking into account both the older and newer characterization of mechanical losses computed by neutral tests. Then a new set of engaged tests was performed and analysed using the new neutral losses with or without the application of the corrective factor previously mentioned. Finally, a general comparison of all the different configurations of engaged tests is shown for clarity.

The results obtained from these new sets of experimental tests, shown within this chapter, will be later used to define the parameters of the dynamic Simulink model of the PMG, whose development will be analysed in Chapter 5.

4.1 Testing Design and Methodology

The experimental tests conducted on the Planetary Magnetic Gearbox prototype were performed to investigate multiple parameters. Primarily, the experiments were designed to accurately measure the mechanical losses in the system under no load conditions, in order to model the frictional effects of the bearings mounted inside the PMG assembly. A second objective was the evaluation of the total losses and the performance parameters of the torque transmission of the PMG, evaluated in its first gear configuration. A third objective was the correction of the data recorded from the prototype by improving the testing conditions and addressing some physical inconsistencies that were found in the older tests with a newer set of tests. The final objective, as well as the most important for the scope of this thesis, is the creation of a correct and accurate dataset that will be utilized for the calibration and validation of the Simulink model of the PMG in the later chapters. In order to fulfil these points, the experimental activity was divided into two sets of tests: neutral tests and engaged tests.

4.1.1 Testing Configurations

The neutral tests are performed with the gearbox mechanically uncoupled, with the carrier axially positioned between the first and second gear setup, as shown in Figure 4.1 (B), so that the magnetic interaction between the inner sun rotors and the outer ring rotors is interrupted and no torque is transferred. Ideally, the only source of torque resistance measured in this configuration is the mechanical loss due to the bearings friction on the rotating shafts. Isolating these losses is very important as they allow for indirectly measure the magnetic losses by simply being subtracted from the total amount of losses in the system measured in the engaged operating conditions. However, a partial residual magnetic coupling could still be present, so the evaluation of a corrective factor is introduced during the data analysis. Since the gearbox is not transmitting torque in the neutral configuration, both sun and ring motors can be independently controlled in speed, without any dynamic coupling between them.

Instead, the engaged tests are performed with the gearbox operating in its first gear, axially aligning the carrier to the sun and ring gears having 5 and 13 permanent magnets pairs respectively, and allowing torque to be transferred via magnetic coupling. This configuration is shown in Figure 4.1 (A). Additionally, the PMG is set up to work in the speed reducer and torque multiplier configuration: the input sun shaft is driven by a motor controlled in speed, while the output ring shaft is controlled by a motor in torque control, in order to simulate a user load (Figure 4.2). These tests allow for the evaluation of the total input and output powers, and, by subtraction, the total power loss in the gearbox, as well as the magnetic and mechanical losses, as previously mentioned. Furthermore, the total, mechanical, and magnetic efficiencies of the PMG can be studied by analysing the acquired data from this engaged configuration.

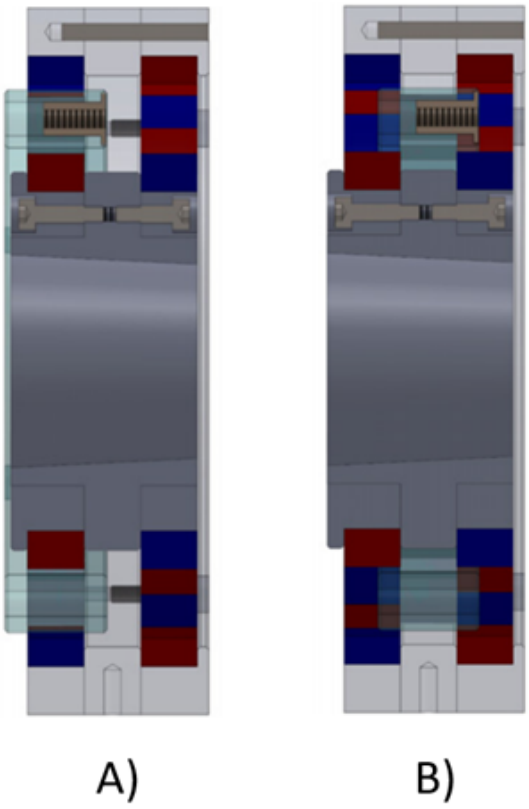

Figure 4.1: Carrier position in Engaged configuration (A) and Neutral configuration (B)

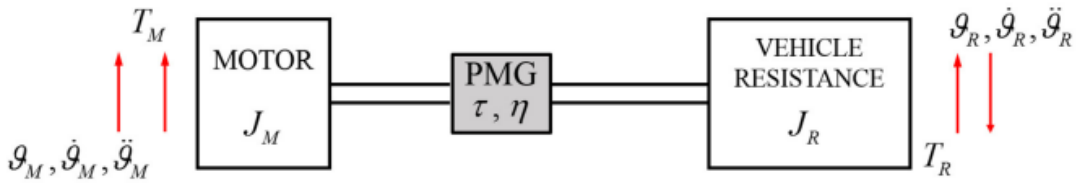

Figure 4.2: Schematic representation of Motor-PMG-User, in speed reducer configuration.

4.1.2 Testing Methodology

A major improvement introduced in the new tests performed on the PMG was the research of the thermal stability of the machine before the data acquisition procedure. In the previous tests, measurements were performed progressing from low to high rotational velocities, with the system gradually heating up as speeds increased. This led to an overestimation of the bearings losses, in particular at lower speeds, due to higher lubrication viscosity and tighter mechanical tolerances. To address this, for the newer tests, the machine was first run at the highest acquisition speed for a few minutes, and only then the data was collected, proceeding with downwards speeds. This procedure was

performed for both neutral and engaged tests, improving the repeatability and accuracy of the acquisitions, eliminating the thermal coupling. Furthermore, all the data acquired during the tests, being them in neutral or engaged configuration, were taken when the system had reached its mechanical steady state condition, with both torques and speeds constant in time, to eliminate any transient behaviour bias that could have altered the results.

To ensure a structured and complete testing environment, all tests were performed following predefined grids of operating conditions. For what concerns neutral tests, a full matrix of sun and ring speed combinations was created by pairing every possible value used in the engaged tests, as well as some extra values for low speeds, as shown in Table 4.1. This allowed for a more complete mapping and definition of the bearing losses contributions.

		Ring speed n_r (rpm)												
		0	60	120	180	240	300	360	420	480	540	600	660	720
Sun speed n_s (rpm)	0													
	60													
	90													
	120													
	156													
	312													
	468													
	624													
	780													
	936													
	1092													
	1248													
	1404													
	1560													
	1716													
	1872													

Table 4.1: Neutral Tests Grid.

For engaged tests, the grid is made up by a sweep of speeds for the sun motor and four different resistant torques on the ring side, as shown in Table 4.2. This matrix allows for a better understanding of the PMG performances over a range of user load scenarios. Both grid types will be filled with the main test parameters and reported in the Appendix.

		Ring Torque T_r (Nm)			
		0.78	1.17	1.56	1.95
Sun speed n_s (rpm)	156				
	312				
	468				
	624				
	780				
	936				
	1092				
	1248				
	1404				
	1560				
	1716				
	1872				

Table 4.2: Engaged Tests Grid.

4.2 Post Processing

4.2.1 Digital Filtering

The raw data acquired during all kinds of tests performed on the gearbox were processed using a digital low pass filter that allows for a cleaner estimation of the transmitted torques. These torque signals recorded from the torsiometers installed on the test bench are often affected by high frequency disturbances coming from mechanical vibrations, sensor noise, or ripples, which are irrelevant for what concerns the study of the steady state analysis of the machine. Not only that, they can distort the torque estimation and lead to inconsistencies in the losses and performance computations. For these reasons, the digital filter allows to retain only the meaningful portion of the signal by eliminating all frequency content above a specific frequency threshold, set to 0.5Hz.

The digital filter works through a 3 step process: first the time domain torque signal is transformed into frequency domain by Fast Fourier Transform (FFT), then all the frequency components above the threshold are zeroed out, and finally the filtered signal is reconstructed in the time domain via an Inverse FFT (IFFT). The whole process is shown in Figure 4.3.

The application of this filtering step is of fundamental importance to achieve consistency across all the torque acquisitions across all the different tests, enabling a more precise identification of the system's losses and efficiencies.

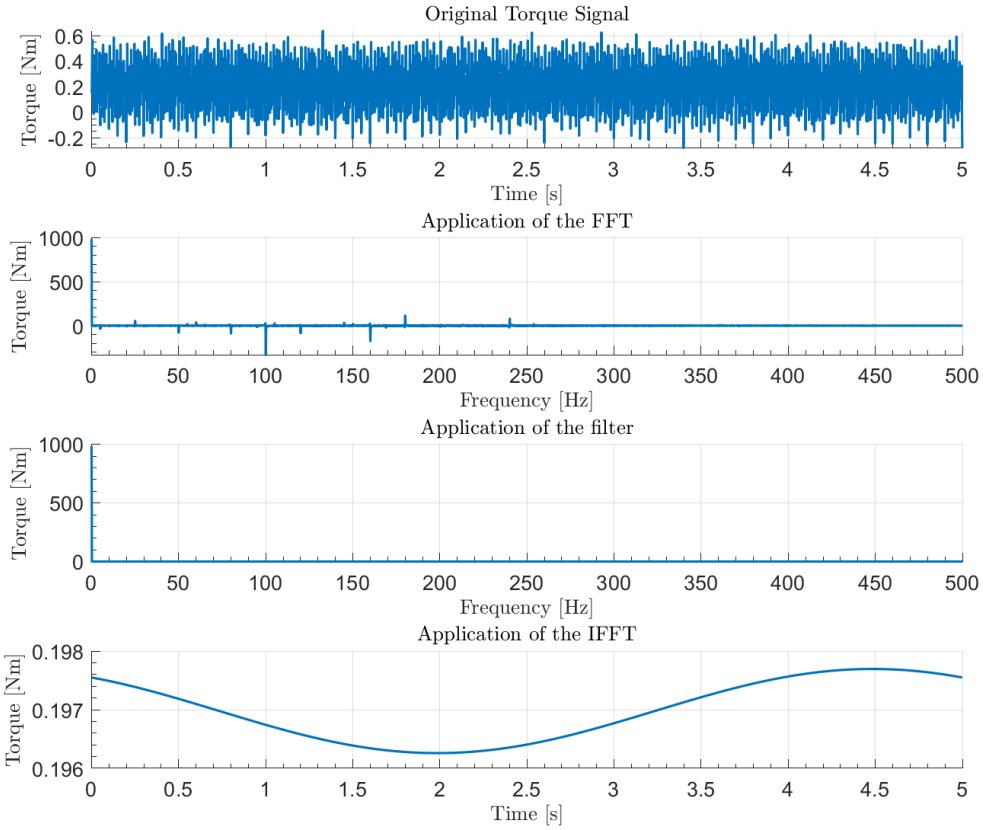

Figure 4.3: Example of Digital Filtering procedure.

4.2.2 Signal Averaging

Once the raw torque signals are filtered using the digital filter previously discussed, an averaging operation is performed to compute a reference value of torque for each test condition. For each acquisition, a time window of 5 seconds is recorded once the system has reached its mechanical steady state conditions, with constant speeds and torques over time. The signal is then filtered and averaged to obtain a single scalar value that represents the effective torque associated with that specific testing condition. This procedure is applied to both the sun and ring shafts torque signals, both in neutral and engaged configurations.

For instance, in a neutral test, where both sun and ring motors are controlled in speed, the torque measured on the sun shaft is filtered, averaged and paired with the combination of sun and ring speed $[n_s, n_r, \bar{T}_{bs}]$, and the same is done for the ring side $[n_s, n_r, \bar{T}_{br}]$. These values are then collected across all combinations tested and inserted in matrices having the same structure as those defined in section 4.1.2, as shown in Figure 4.4.

The same operation is performed also for the torque signals acquired during the

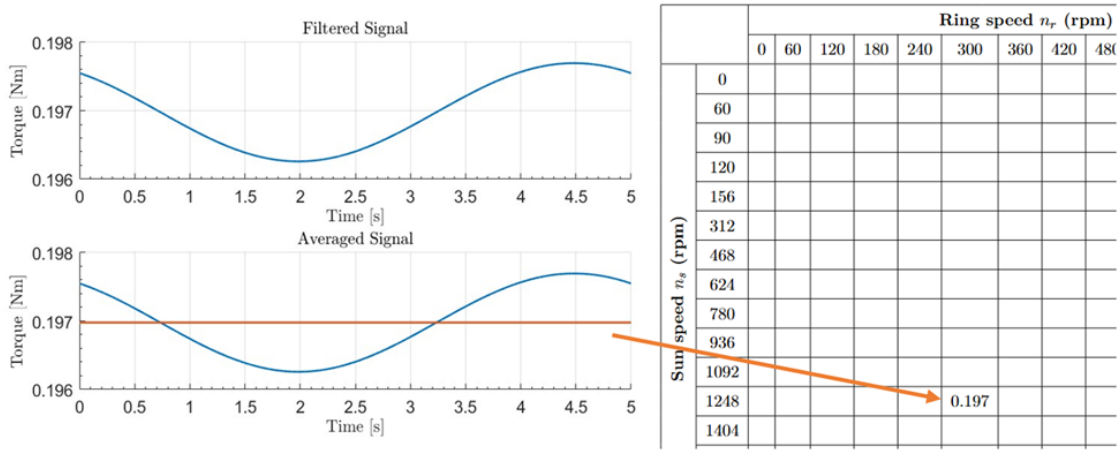

Figure 4.4: Example of averaging and grid filling.

engaged test setup.

The matrices built for the neutral tests will form the basis for the following interpolation step.

4.2.3 Polynomial Least Mean Square Interpolation

For what concerns just the neutral testing, after filtering the torque signals and averaging the values for each point of the testing grids, the next step is to perform an interpolation of the mechanical losses as a function of the shafts speed. This interpolation was performed by means of a Least Mean Square (LMS) fitting, which works by minimizing the root mean square error between the curve and the actual data points:

$$\mathrm{err}_{LMS} = \frac{1}{n}\sqrt{\sum_{i=1}^{n}\left(y_{\mathrm{int}}^{(i)} - y^{(i)}\right)^2} \tag{4.1}$$

An example of the interpolation result is shown in Figure 4.5.

In particular, a polynomial function, whose terms are selected by the user depending on the required complexity of the fitting, is used to interpolate the filtered torque signals, resulting in a smooth and regular trend, deprived of any remaining noises or irregularities. The interpolation was applied separately for the sun and ring shafts, producing two different fitting curves that describe their respective torque losses in neutral conditions. These curves allow the torque losses to be estimated even at speed values that were not experimentally analysed, providing a more general notion of this phenomenon.

4.2.4 Neutral Losses Correction Factor

Finally, it is worth noting that although the neutral tests were conducted to isolate the bearings mechanical losses, during the post processing and data analysis operations performed on the engaged tests data, it was observed that residual magnetic torque losses

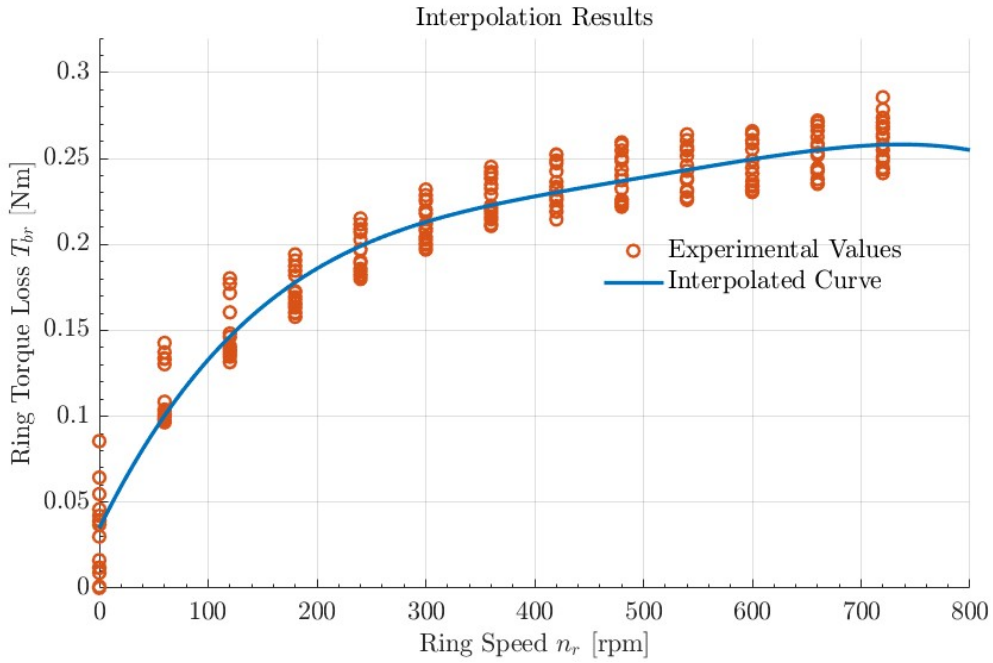

Figure 4.5: Example of Interpolation Results

were still present in the disengaged configuration. These effects could be caused by an imperfect axial position of the carrier that leads to a non perfect disengagement of the gear or from remaining magnetic fields and interactions between the gears, and, hence, not due to the pure bearing friction that the test was intended to capture.

The existence of this issue was raised by the comparison of the total power losses measured in the engaged tests and the 'bearings' losses analysed at the same rotors speed in the neutral tests: in all tests combination it was found that the neutral losses were higher than the engaged losses in at least some operational points, leading to magnetic efficiencies above 100%, which is physically wrong. By studying this phenomenon, it was found out that the application of a 0.9 corrective factor to the neutral losses guaranteed that the engaged losses would always be higher than the neutral losses, and a magnetic efficiency always lower than 100%. This means that 90% of the neutral losses are to be attributed to bearings losses, while the remaining 10% is related to remaining magnetic interactions losses. The application of a correction factor is shown in Figure 4.6.

Further analysis, performed in the Simulink model development stage discussed in chapter 5, showed that the lower the correction factor, the better the numerical interpolation of the system behaviour would be. To this end, a coefficient of 0.8 (80% mechanical losses and 20% residual magnetic losses in the neutral sets) was selected, being it a compromise between ensuring a low enough magnetic contribution in neutral conditions and achieving an improved performance interpolation with the digital model.

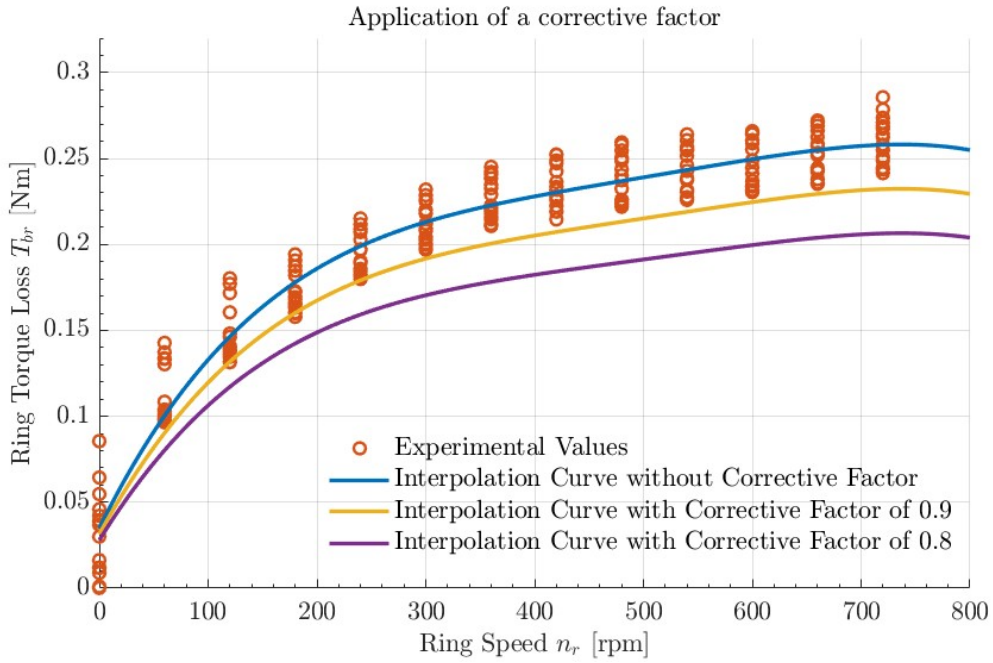

Figure 4.6: Example of application of a Correction Factor.

4.3 Neutral Tests Results

The neutral tests were designed to measure the mechanical losses within the Planetary Magnetic Gearbox by operating the system in a disengaged configuration, in which magnetic torque transmission is disabled. This condition is achieved by axially positioning the carrier gear between the two engaged configurations, decoupling sun and ring rotors. In this setup, the torque measured on each shaft is primarily due to the frictional resistance induced by the bearings mounted on the prototype.

Two different datasets are compared: the first one was acquired in tests performed prior to the development of this thesis, while the second one was collected during this work to try to correct some imperfections encountered in the previous set, mainly providing thermal stability to the system before the data acquisition procedure. Both datasets have been processed using the same digital filtering, signal averaging, and polynomial interpolation procedures previously discussed in section 4.2.

The test results will be displayed and compared to identify the dataset that better represents the mechanical losses inside the PMG, following the expected physical trend while having high degrees of consistency and smoothness across the acquisitions.

4.3.1 Sun Shaft Torque Losses Results

For what concerns the sun shaft, the torque losses acquired from the two different datasets are shown in 2D, plotting the registered torque losses over the sun speed, varying the ring shaft speed, in Figure 4.7 and in 3D in Figure 4.8. In both figures it is possible

to see how the adoption of the new testing methodology discussed in section 4.1, which consists of first bringing the system to its thermal stability and then proceed in the data acquisition procedure by progressively reducing the speed, unlike the previous tests where an ascending speed approach was adopted, results in a more precise evaluation of the neutral losses, especially at higher velocities.

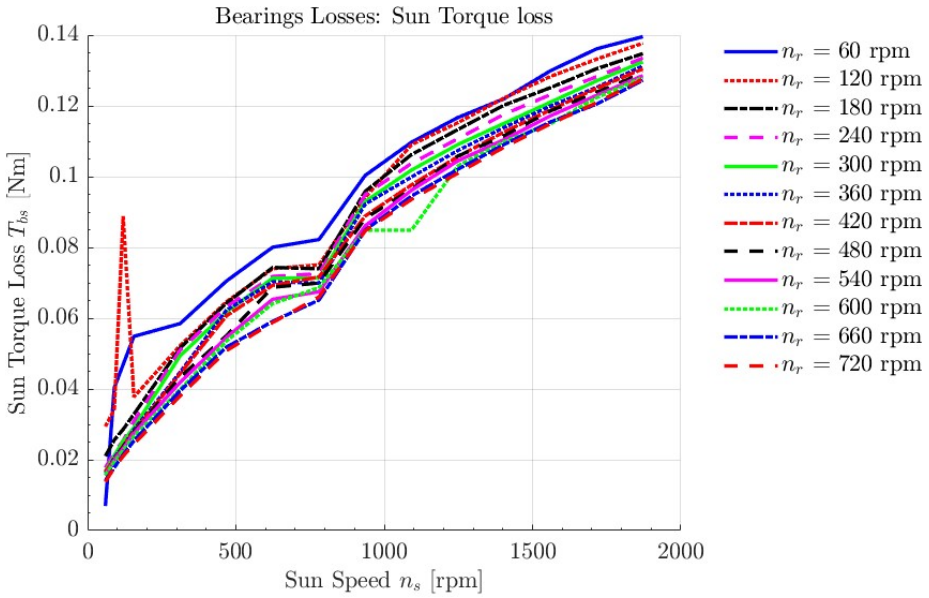

(a) Old Neutral Tests

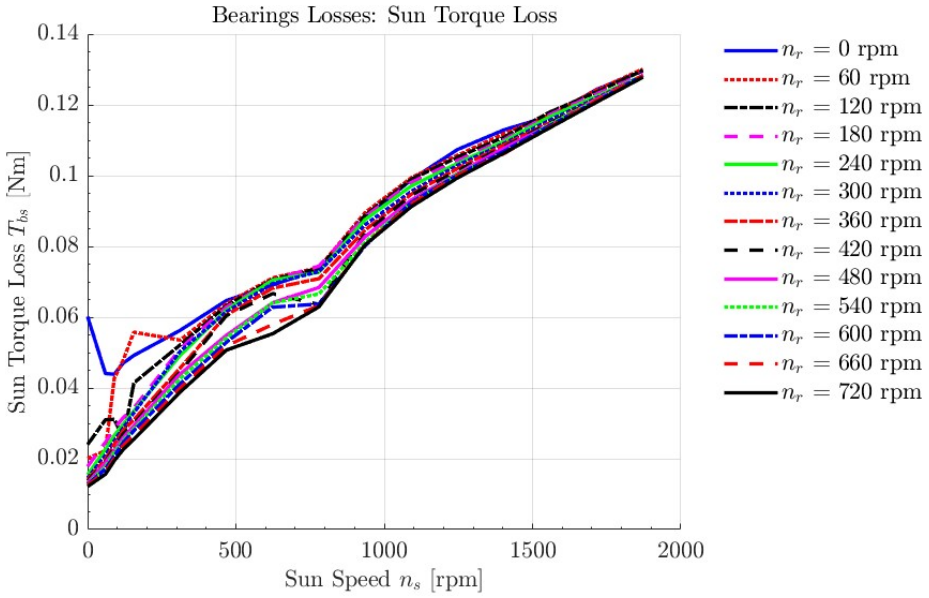

(b) New Neutral Tests

Figure 4.7: 2D Sun Shaft Torque Loss T_{bs} vs n_s, varying n_r.

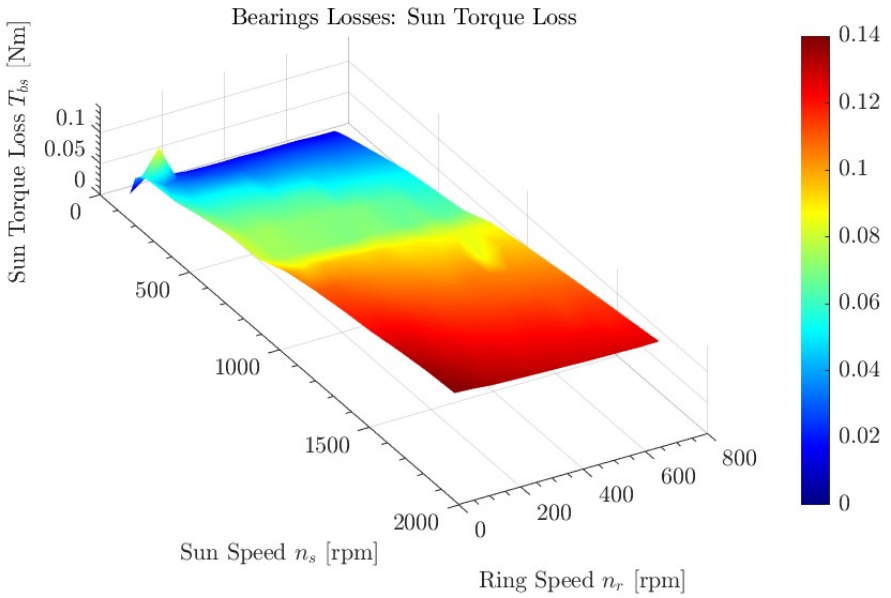

(a) Old Neutral Tests

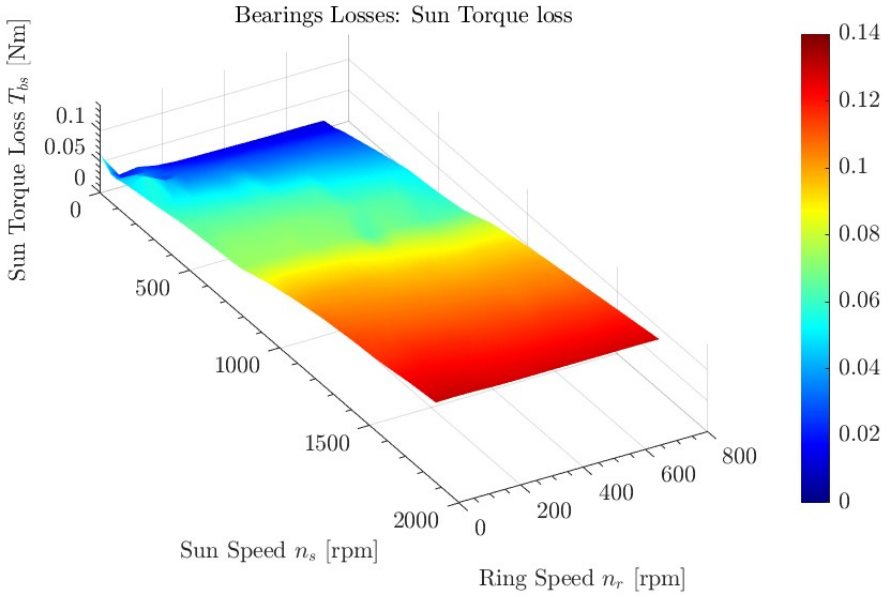

(b) New Neutral Tests

Figure 4.8: 3D Sun Shaft Torque Loss Surface T_{bs} as function of n_s and n_r.

The interpolation results for these tests are shown in Figure 4.9. The general trend is more or less the same across the two datasets, with the torque loss increasing as speeds increase. The values intersected by the fitting curves are almost identical, meaning that, while the second newer set of tests provided better results accuracy, both tests are acceptable for depicting neutral torque losses in the sun shaft side.

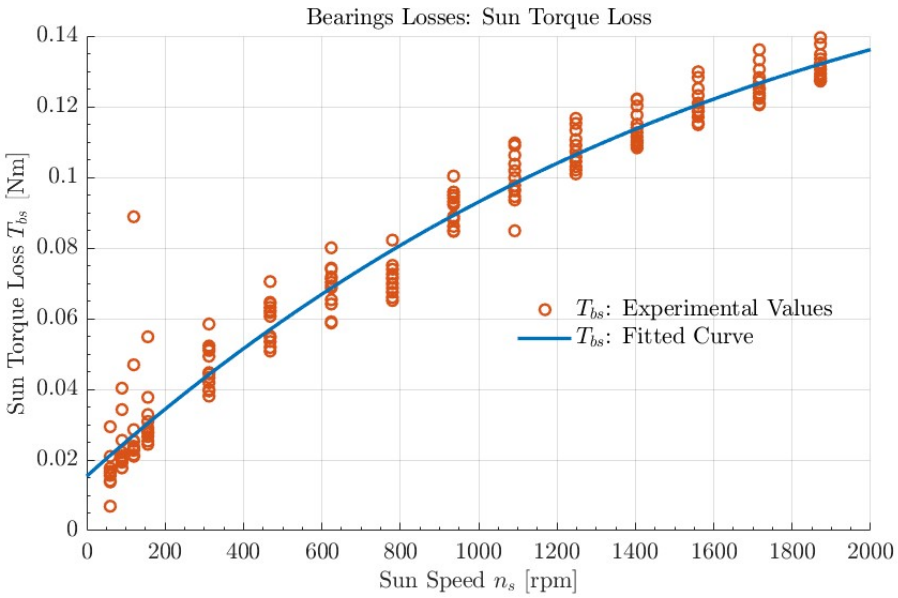

(a) Old Neutral Tests

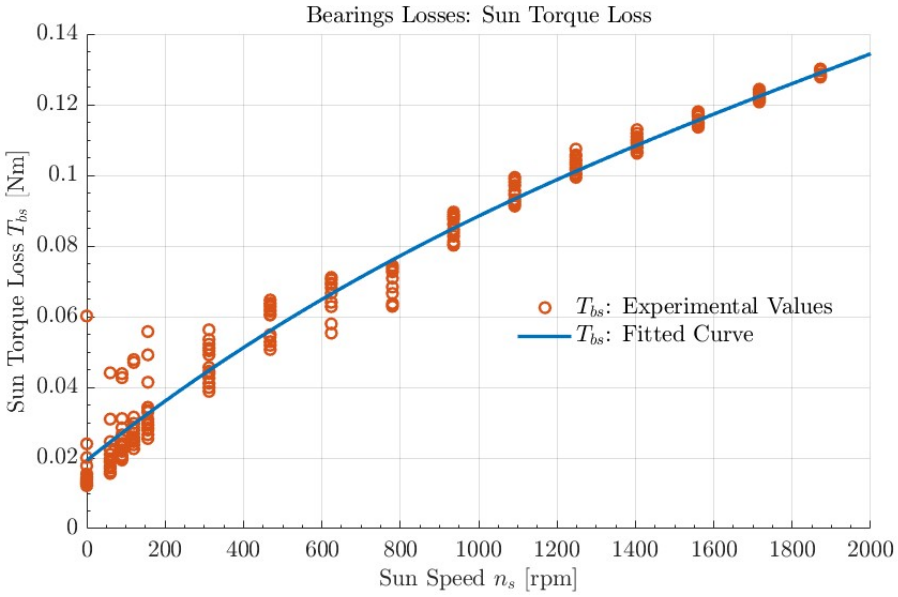

(b) New Neutral Tests

Figure 4.9: Interpolation Results of the Sun Shaft Torque Loss T_{bs} vs n_s.

4.3.2 Ring Shaft Torque Losses Results

Contrary to the sun shaft results, for what concerns the ring shaft, the torque losses results are extremely different in the two datasets. The results are shown in 2D in Figure 4.10, plotting the registered torque losses over the ring speed varying the sun shaft speed, and

in 3D in Figure 4.11. In the older set of neutral tests, the torque losses showed a non monotonic wave-like trend: as the ring speed increased, the losses initially increased up to a peak at $n_r = 300rpm$, then decreased up to $n_r = 660rpm$, before rising again at higher speeds. This phenomenon is absent in the newer configuration of neutral tests, which instead shows a more physically consistent monotonic trend like the one encountered for the sun shaft.

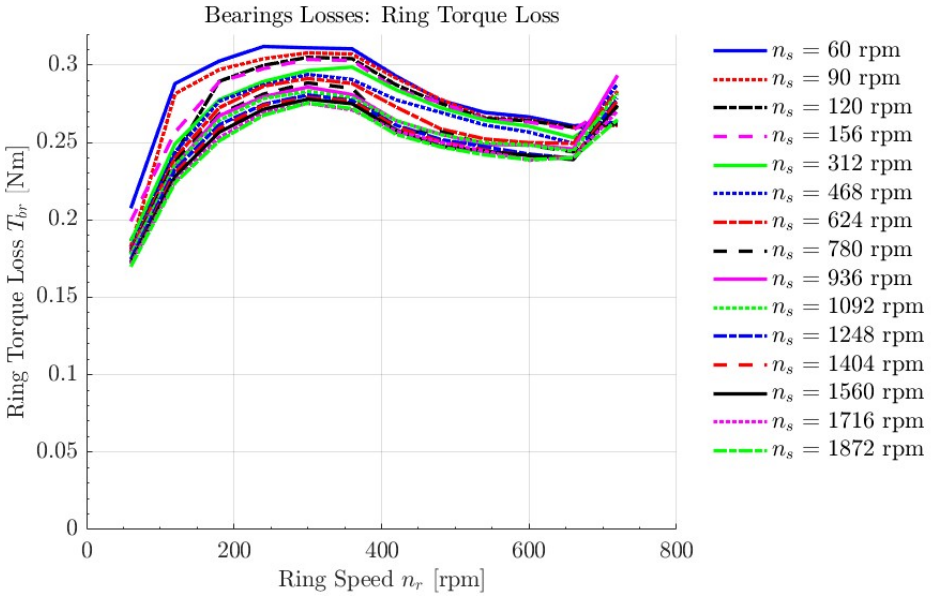

(a) Old Neutral Tests

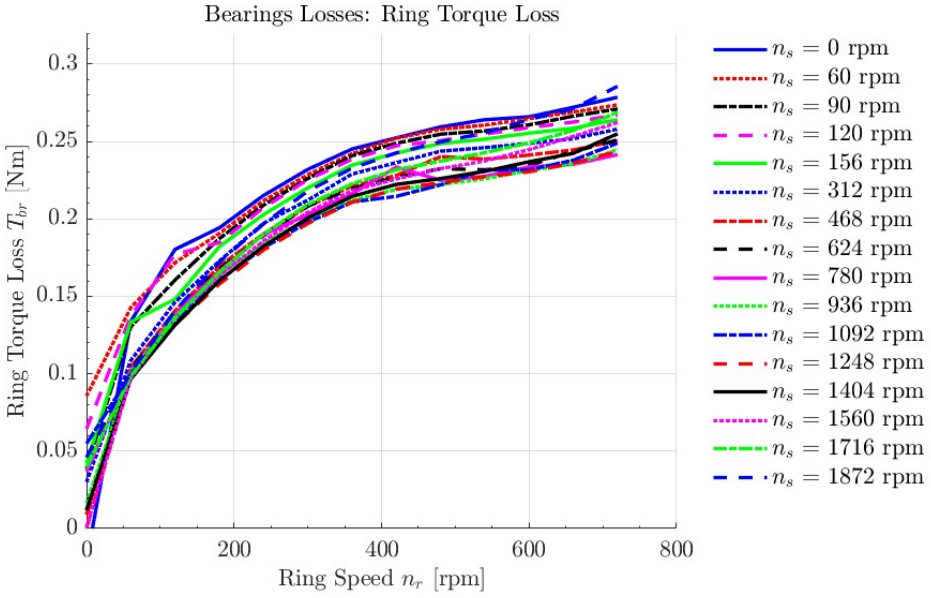

(b) New Neutral Tests

Figure 4.10: 2D Ring Shaft Torque Loss T_{br} vs n_r, varying n_s.

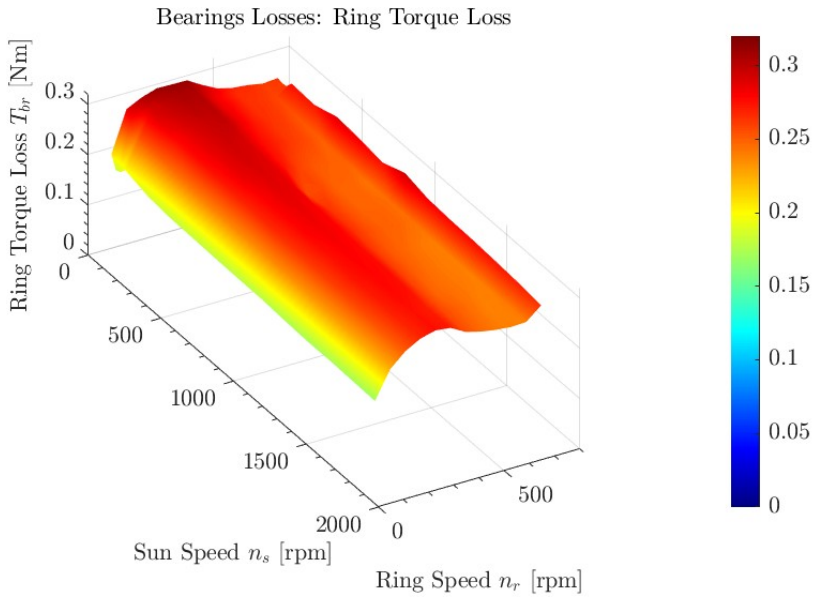

(a) Old Neutral Tests

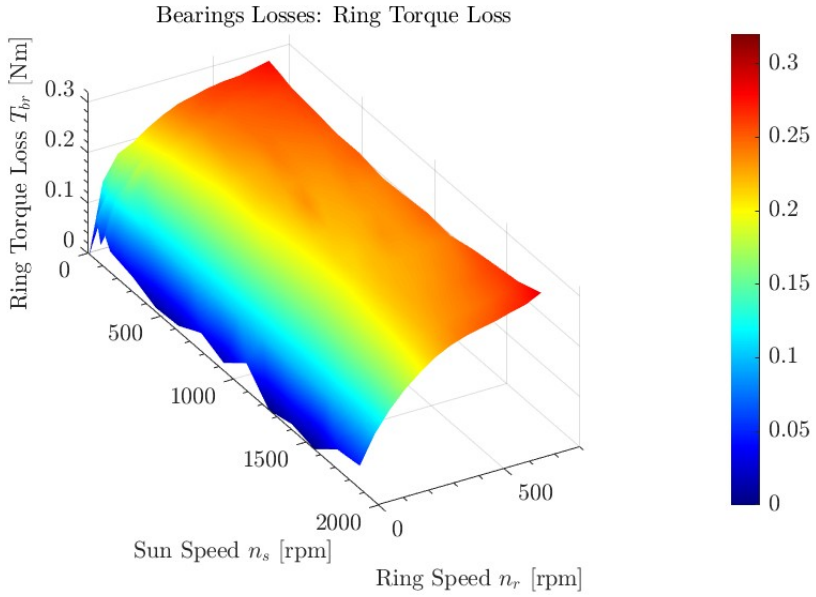

(b) New Neutral Tests

Figure 4.11: 3D Ring Shaft Torque Loss Surface T_{br} as function of n_s and n_r.

The interpolation results for these tests are shown in Figure 4.12. The new set of neutral tests shows a much more physically consistent trend for the torque losses on the ring shaft. The possible reason for the erroneous acquisitions in the older dataset could be attributable to the absence of thermal regulation in the machine during data acquisition. At lower temperatures, the bearing's lubricant shows a higher viscosity, resulting in

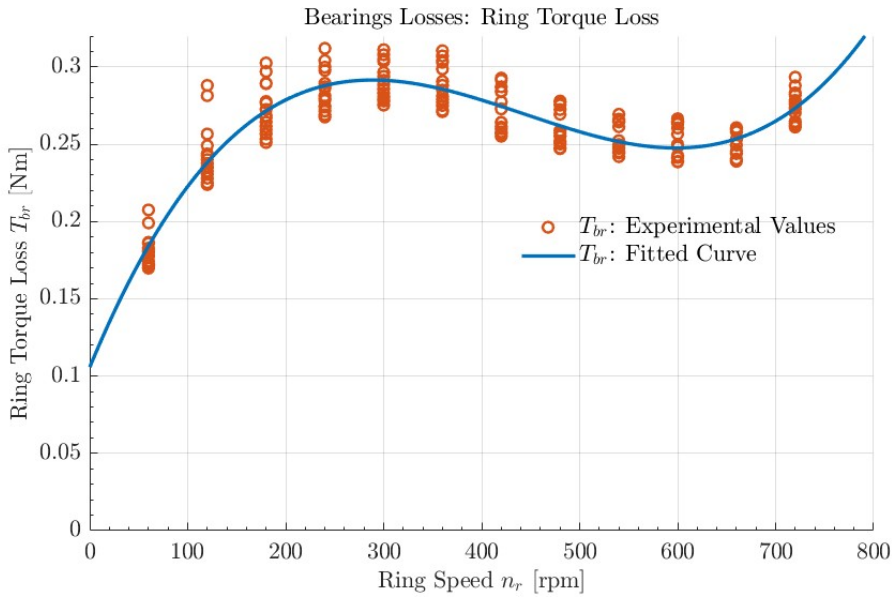

(a) Old Neutral Tests

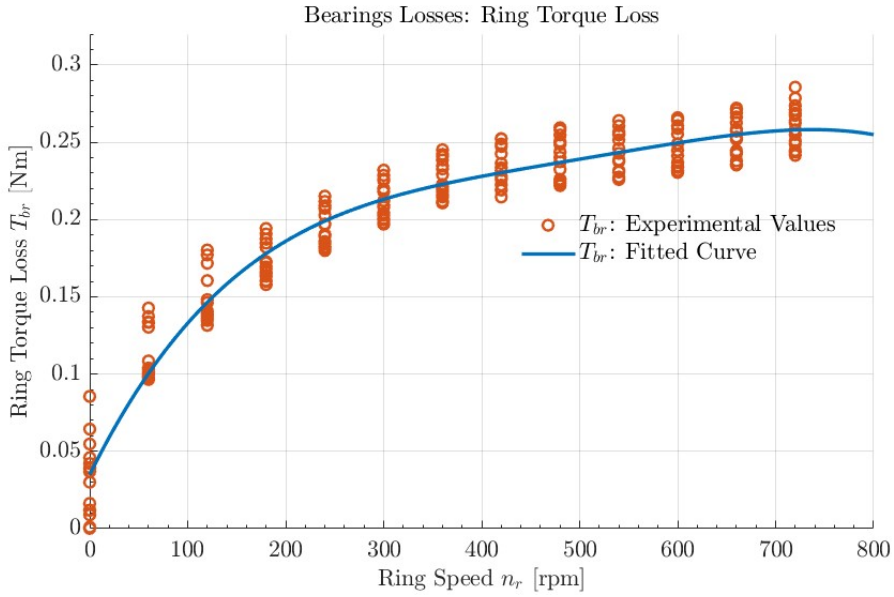

(b) New Neutral Tests

Figure 4.12: Interpolation Results of the Ring Shaft Torque Loss T_{br} vs n_r.

increased friction and, hence, elevated torque losses. As the system heats up, the viscosity decreases, reducing mechanical dissipation. This thermal effect is particularly visible on the ring shaft, where lower speed tests have been performed to match those of the engaged tests, delaying the thermal equilibrium of the bearings. In contrast, the sun shaft bearings, tested at higher rotational speeds, reached thermal stability more rapidly. As

a result, only after the ring speed exceeded approximately $n_r = 300rpm$, the properties of the lubricant started to normalise, showing a decreasing trend of torque losses.

4.3.3 Total Neutral Torque Losses

The sum of the torque losses in both sets of tests is shown in Figure 4.13.

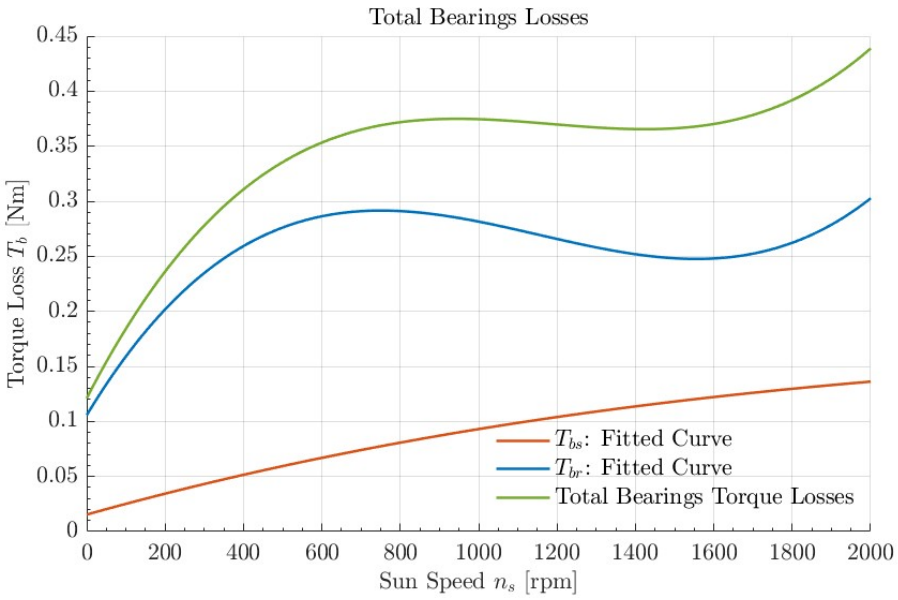

(a) Old Neutral Tests

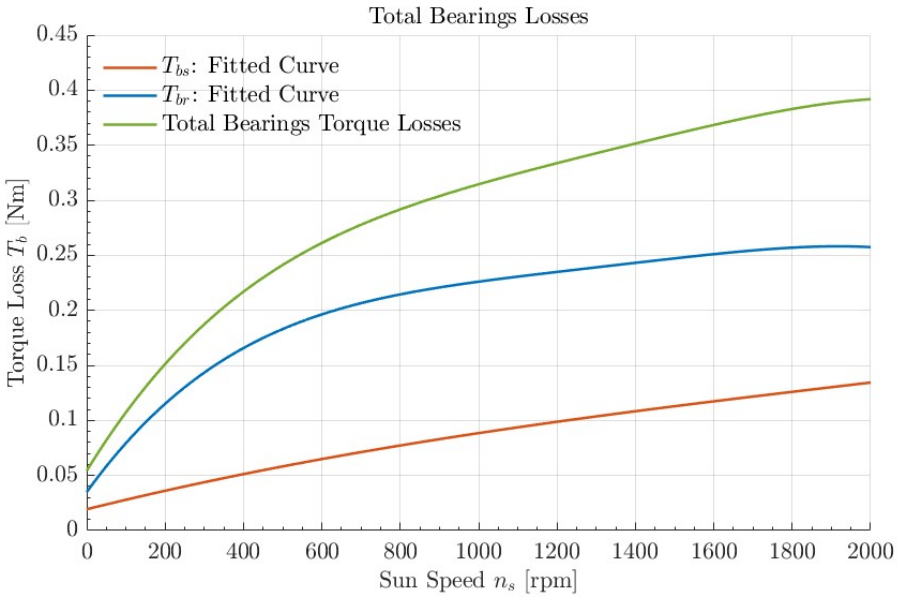

(b) New Neutral Tests

Figure 4.13: Total Bearings Torque Losses Results T_b vs n_s.

The reference used to graph the curves has been set to be the sun speed, meaning that the torque losses evaluated on the ring side have been transposed from the ring speed, at which they have been evaluated, by the use of the gear ratio for the first gear configuration, $|\tau| = 2.6$. This allows to obtain the total neutral losses to be accounted for in the later engaged tests.

It is clear that the overall trends obtained with the new methodology applied to the new set of neutral tests are much more compliant with the expected torque losses. The values obtained with the acquisition on the ring side in the older set of tests completely skew the results, making them not physically valid.

The torque losses measured in the new set of neutral tests are going to be used as the foundation for the following analysis.

4.4 Engaged Tests Results

The engaged tests were designed to measure the power losses within the Planetary Magnetic Gearbox and its transmission efficiency across a range of resistant torque scenarios. For this purpose, the carrier is axially positioned along the first set of sun and ring gears, allowing for torque to be magnetically transmitted from the input shaft to the output shaft.

In these tests, the sun shaft motor was controlled in speed, while the ring shaft motor was controlled in torque, in order to simulate different user loads. By measuring the rotational velocities and torques of both shafts, it was possible to calculate the input and output mechanical powers, allowing for the computation of the total power losses in the system. Additionally, by subtracting the mechanical losses previously computed in the neutral tests, it was possible to determine the magnetic losses inside the PMG during operating conditions, enabling the computation of both mechanical and magnetic efficiencies.

Following the same procedure used for the neutral tests, two different sets of engaged tests were analysed: an older one acquired prior to this thesis work and a newer set obtained using the improved methodology that was described in section 4.1. The necessity of acquiring a new set of engaged tests was due to some inconsistencies found in the previous acquisitions, and in particular in the lack of precision and repeatability of the losses, as well as instances of magnetic efficiencies running above the unit value. The combination of updated methodology and the application of a corrective factor to take into account the residual magnetic losses hidden in the neutral test losses will prove to solve said inconsistencies.

It is important to specify that both datasets have been analysed using the updated mechanical losses values obtained with the new sets of neutral tests, while any combination that included the old neutral losses models is ignored because of it being not physically valuable. All engaged tests results are summarised to provide a detailed comparison, leading to the choice of the suitable dataset that will be used in chapter 6 to test the simulation results of the PMG's digital model.

4.4.1 Power losses and Efficiency computations

In order to compare the two different datasets, it is necessary to first define the equations to compute the different power losses and efficiency values.

For what concerns the total power losses, they are dependent on the specific engaged tests set that is being analysed. Their computation is obtained by the subtraction of the input power and the output power, as follows:

$$P_{tot,loss} = \omega_s T_s - \omega_r T_r \tag{4.2}$$

For what concerns the mechanical torque losses T_{bs} and T_{br}, they have been already defined with the neutral tests, and in particular with the interpolating curves relative to the new set of data. To compute the bearings power losses, it is possible to simply add the bearings power loss from both sides:

$$P_{b,loss} = \omega_s T_{bs} + \omega_r T_{br} \tag{4.3}$$

The bearings power losses are exclusively dependent on the neutral tests results and will be used for both sets of engaged tests results.

The last, and most important, power loss to consider is the magnetic power loss. This variable is again dependent on the analysed engaged tests sets under analysis. It can be computed by subtracting the bearings power loss from the total power loss, leading to the following equation:

$$\begin{aligned} P_{m,loss} = P_{tot,loss} - P_{b,loss} = (\omega_s T_s - \omega_r T_r) - (\omega_s T_{bs} + \omega_r T_{br}) = \\ = (T_s - T_{bs})\,\omega_s - (T_r + T_{br})\,\omega_r \end{aligned} \tag{4.4}$$

It is also possible to get to the same result by analysing the FBD of the engaged system, by separating the bearings from the PMG assembly, as shown in Figure 4.14.

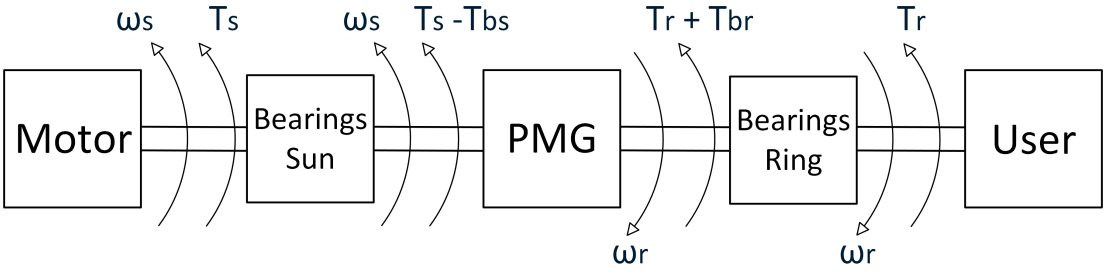

Figure 4.14: FBD of the engaged test bench.

Following the FBD, it is also possible to easily compute all the relevant efficiencies of the system.

The total efficiency takes into account both the PMG and the bearings on either side. In formulas, it is defined as the ratio between the output power sent to the user and the input power provided by the main motor:

$$\eta_{tot} = \frac{T_r\,\omega_r}{T_s\,\omega_s}\,(\cdot 100\%) \tag{4.5}$$

The magnetic efficiency is instead defined by considering the PMG by itself, as the ratio between its output power (equal to the input power of the ring shaft bearings) and its input power (equal to the output power from the sun shaft bearings):

$$\eta_m = \frac{(T_r + T_{br})\,\omega_r}{(T_s - T_{bs})\,\omega_s}\,(\cdot 100\%) \tag{4.6}$$

Finally, the bearings efficiency can be computed by dividing the total efficiency by the magnetic efficiency as follows:

$$\eta_b = \frac{\eta_{tot}}{\eta_m}\,(\cdot 100\%) \tag{4.7}$$

An important consideration is that all values of power losses and efficiencies are punctually defined and depend on the shaft speeds. Since the engaged tests were conducted under steady state conditions, the ring shaft speed is directly linked to the sun shaft speed through the gear ratio of the engaged configuration (i.e. $|\tau| = 2.6$). As a result, the system behaviour can be characterized using a single degree of freedom, which can be either the sun speed, the ring speed, or the relative speed difference between the two. For what concerns this analysis, power losses are expressed as a function of the ring shaft speed, while efficiencies are referenced to the speed difference between the sun and ring shafts.

4.4.2 Old Engaged Tests vs New Engaged Tests

For what concerns the total power losses, a direct comparison between the older and newer sets of engaged tests is presented in Figure 4.15.

The results from the old set of engaged tests show a noticeable dispersion of values depending on the applied User Torque T_u. However, the power losses computed in the system should only be dependent on the reference rotational speed utilised, and not on the applied load. This dispersion suggests that, as also seen in the older neutral tests, the erroneous methodology applied for the data acquisition led to an inaccurate representation of the power losses in the system.

The results of the new methodology are evident in Figure 4.15 (b), where the total losses curves acquired for the same range of user torques are much more overlaid. These results show a lack of dependency on the load, being the power losses only depend on the reference speeds. This reveals that the improvements made in the new engaged tests acquisitions lead to a higher degree of precision and repeatability of the analysed phenomena.

Despite these improvements, it can be noticed that for certain ranges of speed, the total losses curves fall below the bearings losses curve. This indicates that the magnetic losses would be negative,as shown in Figure 4.16, which is physically unacceptable. This is the main reason that leads to believe that the bearings losses computed in the neutral tests have residual magnetic losses within them, meaning that they are not purely due to mechanical frictions, as well as the introduction of a correction coefficient.

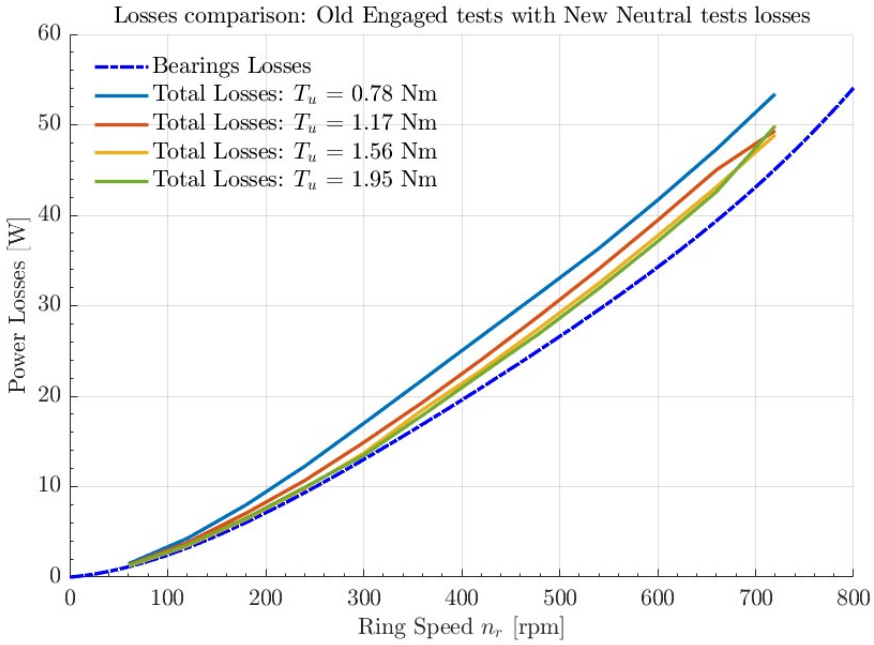

(a) Old Engaged Tests

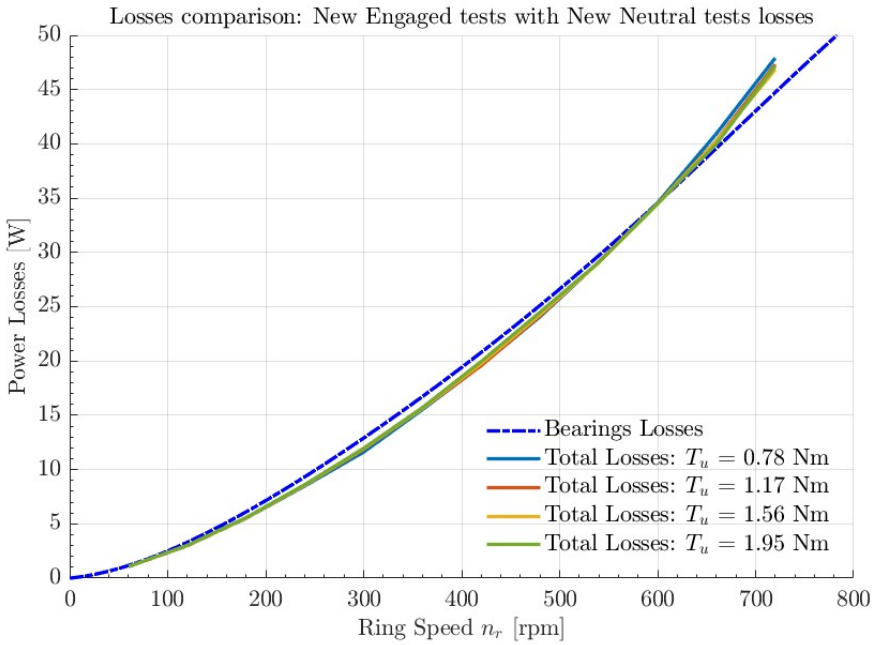

(b) New Engaged Tests

Figure 4.15: Total Power Losses Results $P_{tot,loss}$ vs n_r.

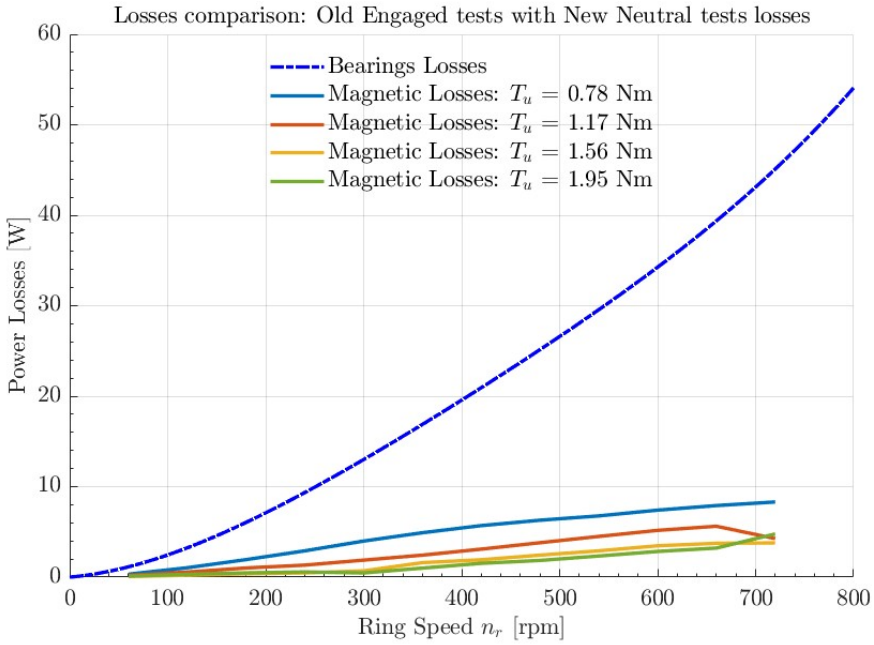

(a) Old Engaged Tests

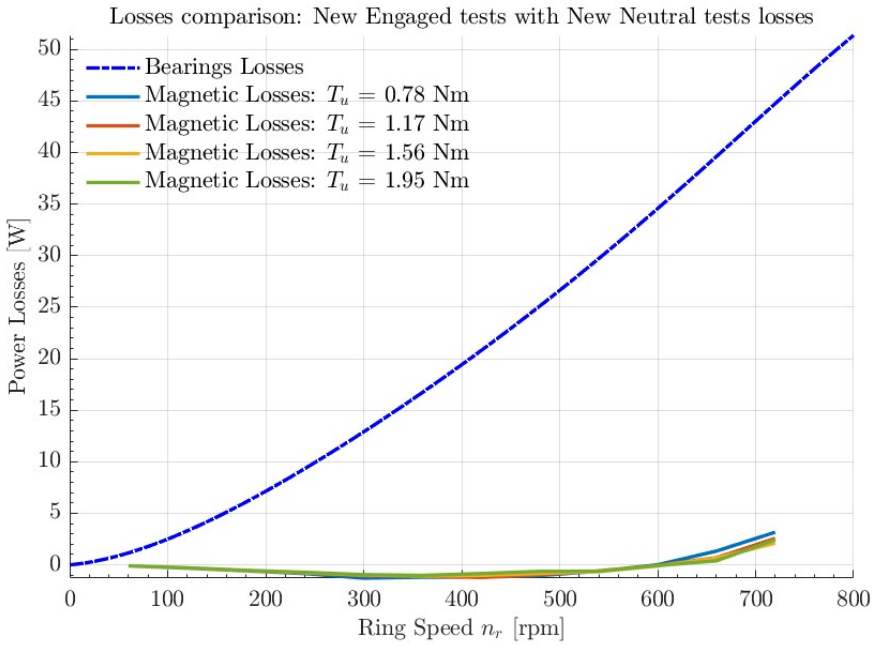

(b) New Engaged Tests

Figure 4.16: Magnetic Power Losses Results $P_{m,loss}$ vs n_r.

4.4.3 New Engaged tests with Correction Factor

As previously analysed in subsection 4.2.4, it was found out that the application of a 0.9 factor to the neutral losses acquired with the new tests would guarantee that the magnetic losses would always be positive and the magnetic efficiency would be below 100%. Further analysis that will be performed later in this work showed that the application of a lower correction factor would increase the accuracy of the Simulink model of the prototype. For this reason, a coefficient of 0.8 was selected, being it a compromise between accurate enough digital model and low magnetic losses contribution.

The results of the neutral tests correction factor on the total power losses and magnetic losses is shown in Figure 4.17 and Figure 4.18 respectively. In particular, the newly introduced coefficient leads to a reduction of the bearings losses curve, as well as an increase of the magnetic losses curves, obtained from a difference between the total and bearings losses.

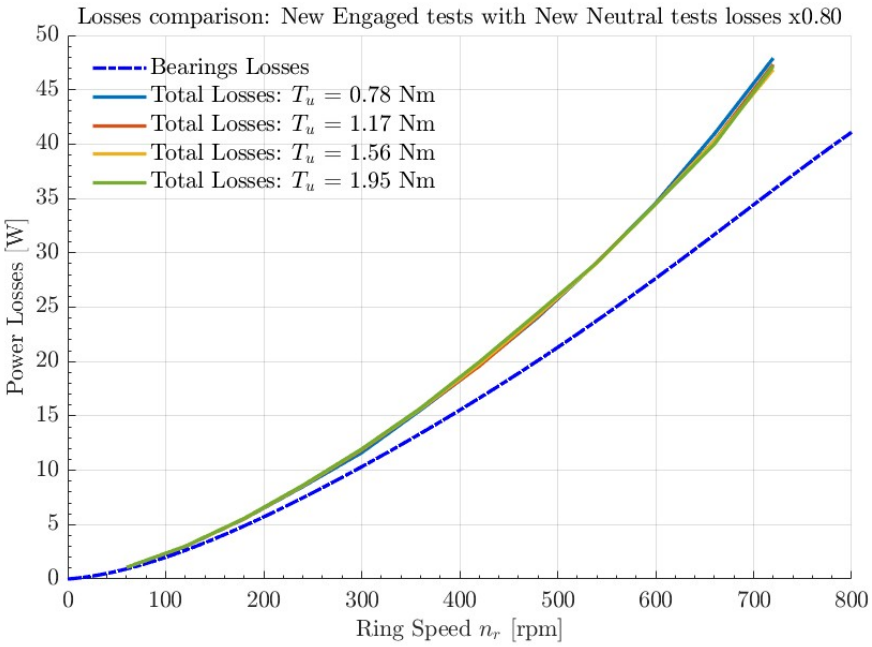

Figure 4.17: Total Power Losses Results with Correction Factor.

The efficiencies computed with this final tests configuration are shown in Figure 4.19, Figure 4.20 and Figure 4.21.

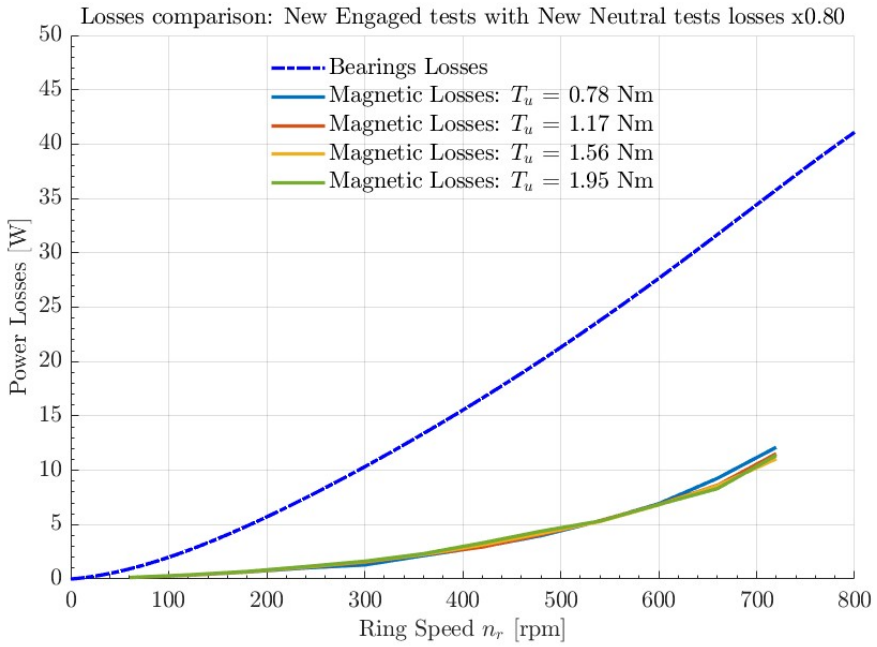

Figure 4.18: Magnetic Power Losses Results with Correction Factor.

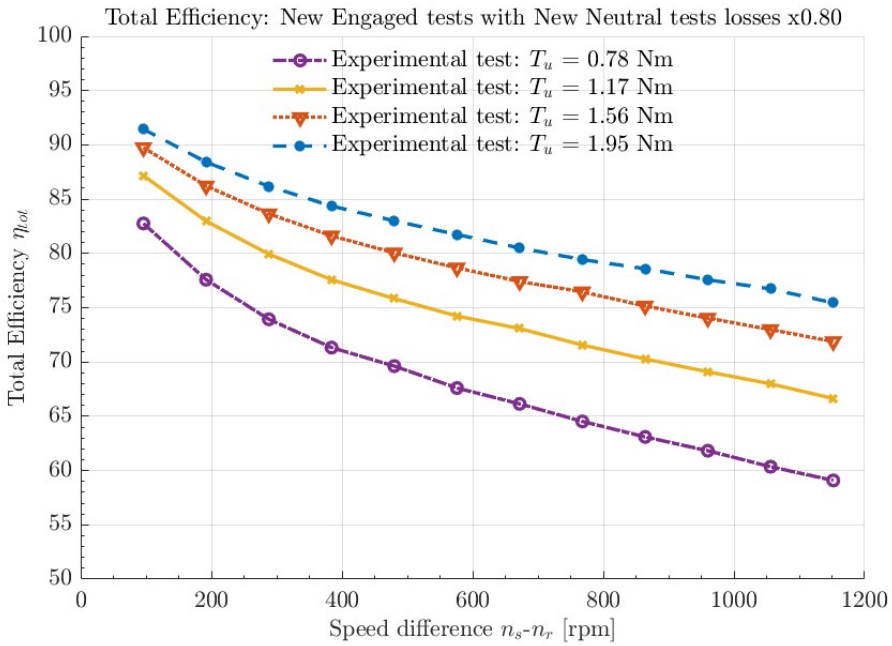

Figure 4.19: Total Efficiency Results with Correction Factor.

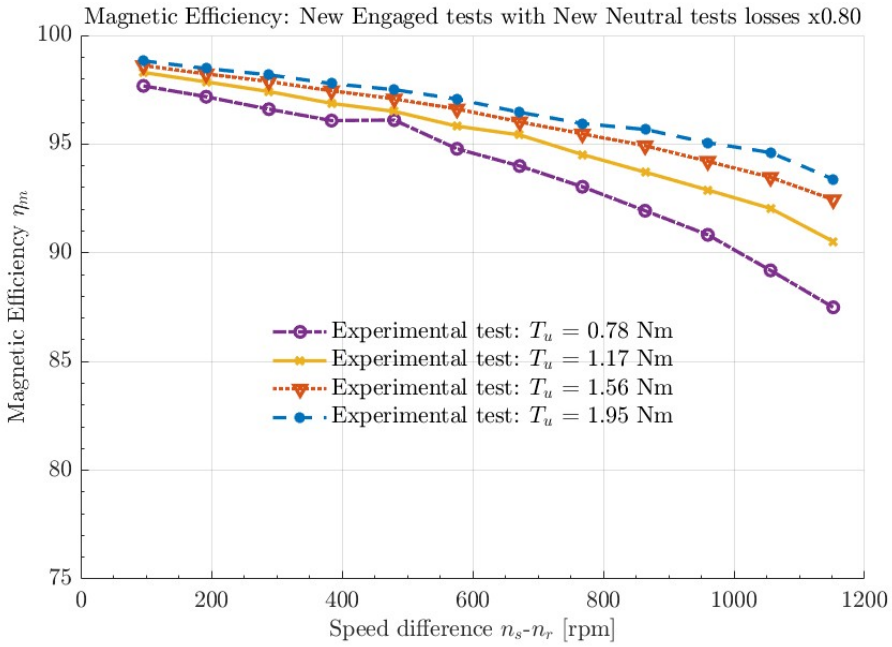

Figure 4.20: Magnetic Efficiency Results with Correction Factor.

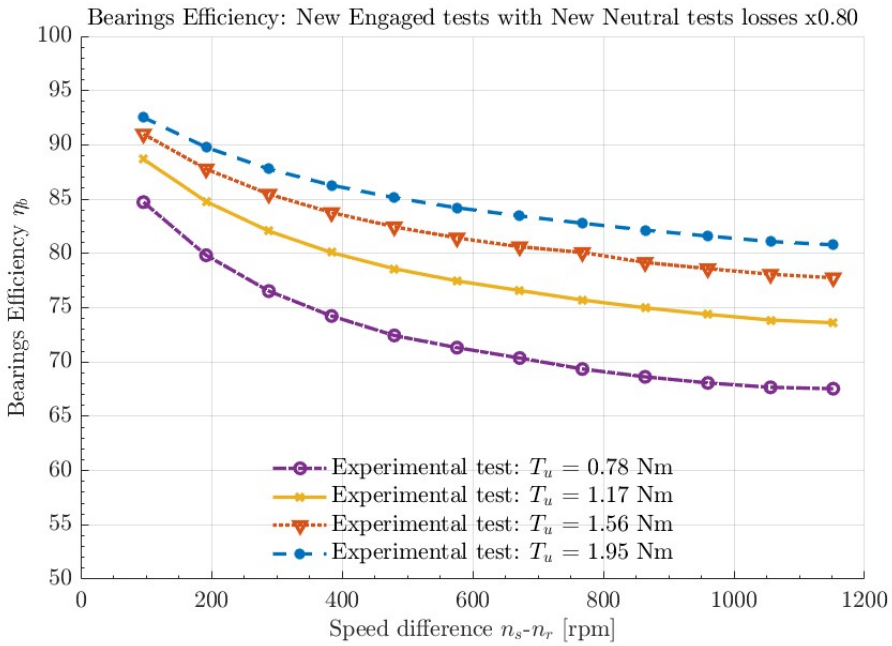

Figure 4.21: Bearings Efficiency Results with Correction Factor.

4.4.4 Engaged Tests Summary and Comparison

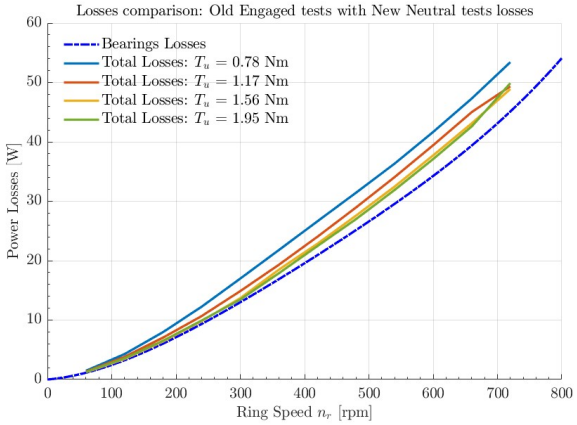

(a) Old Engaged tests with New Neutral losses.

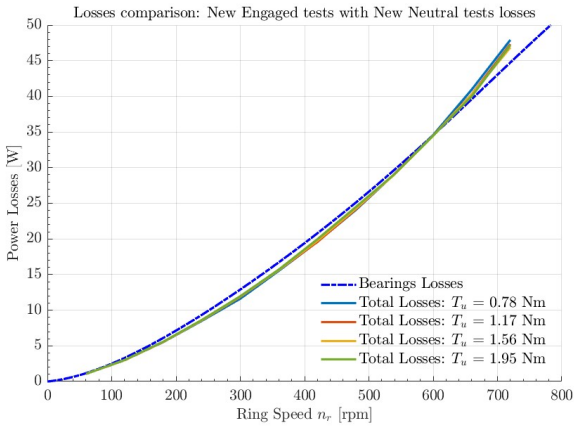

(b) New Engaged tests with New Neutral losses.

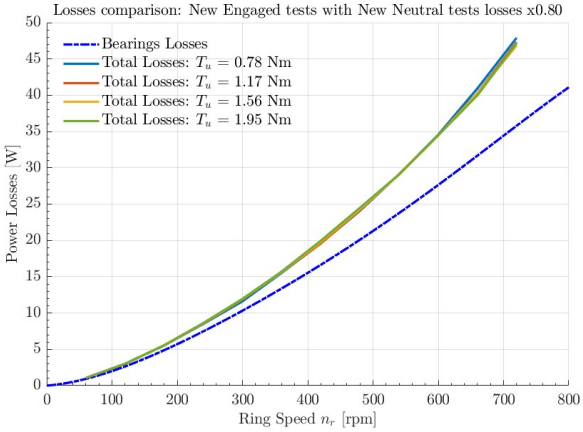

(c) New Engaged tests with New Neutral losses x0.8.

Figure 4.22: Total Power Losses comparison across all engaged datasets.

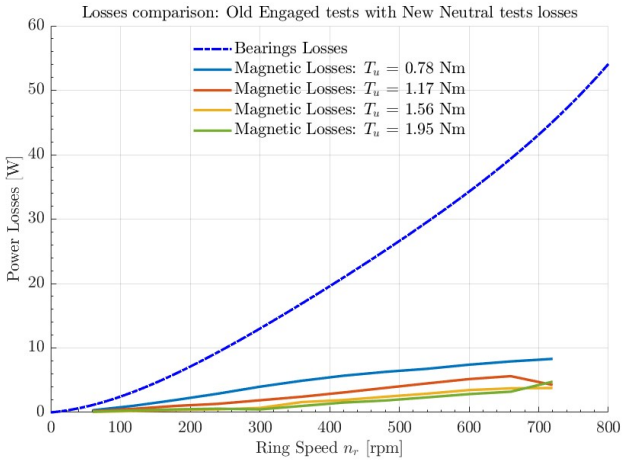

(a) Old Engaged tests with New Neutral losses.

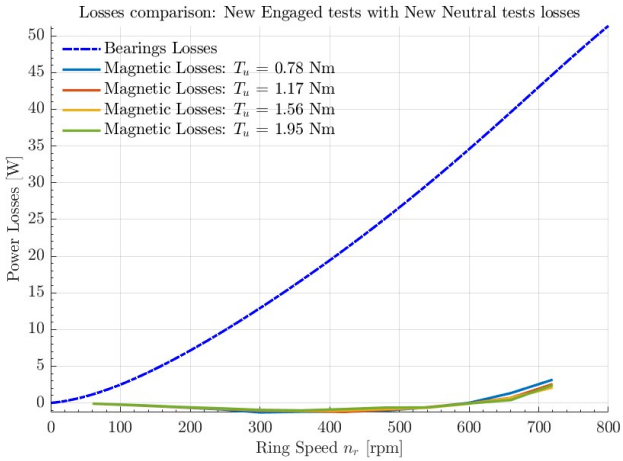

(b) New Engaged tests with New Neutral losses.

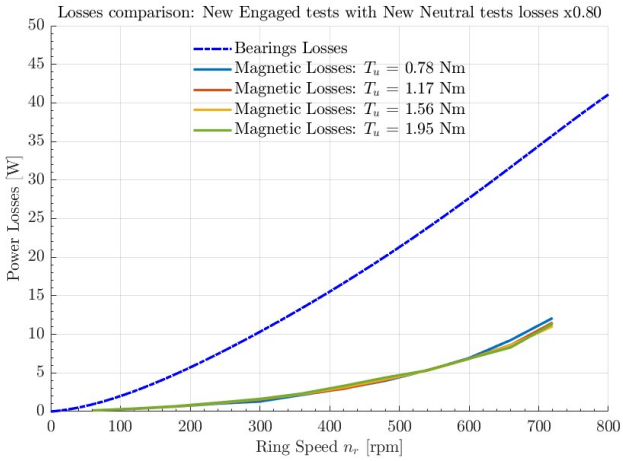

(c) New Engaged tests with New Neutral losses x0.8.

Figure 4.23: Magnetic Power Losses comparison across all engaged datasets.

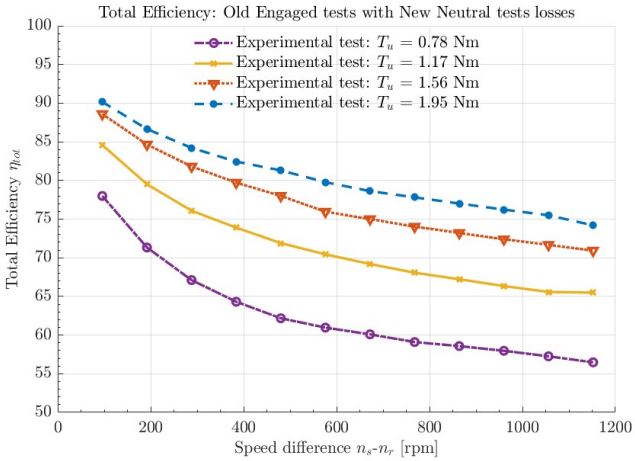

(a) Old Engaged tests with New Neutral losses.

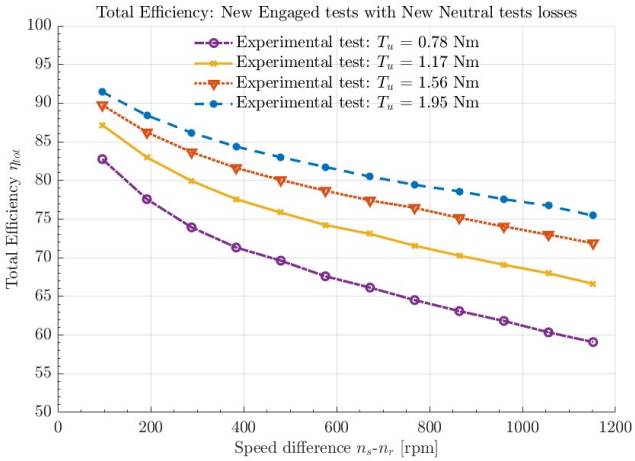

(b) New Engaged tests with New Neutral losses.

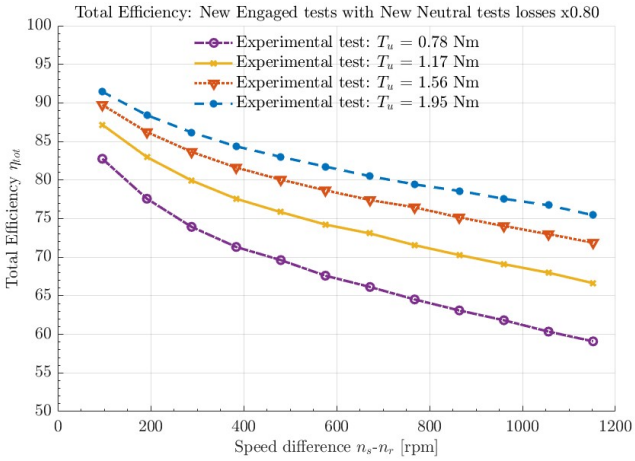

(c) New Engaged tests with New Neutral losses x0.8.

Figure 4.24: Total Efficiency comparison across all engaged datasets.

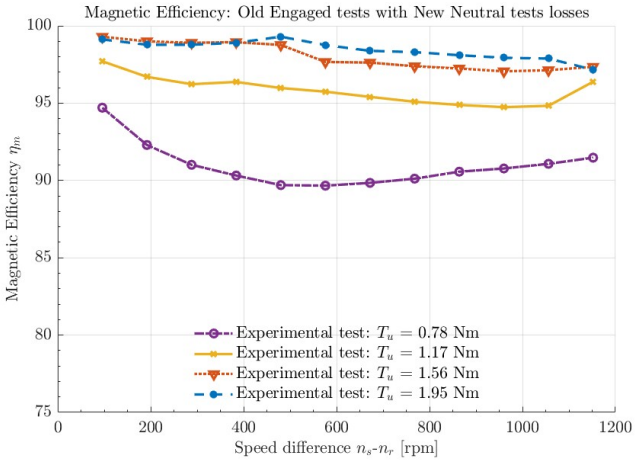

(a) Old Engaged tests with New Neutral losses.

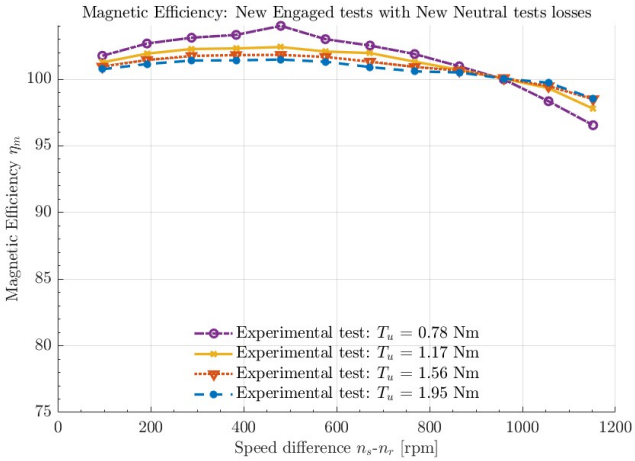

(b) New Engaged tests with New Neutral losses.

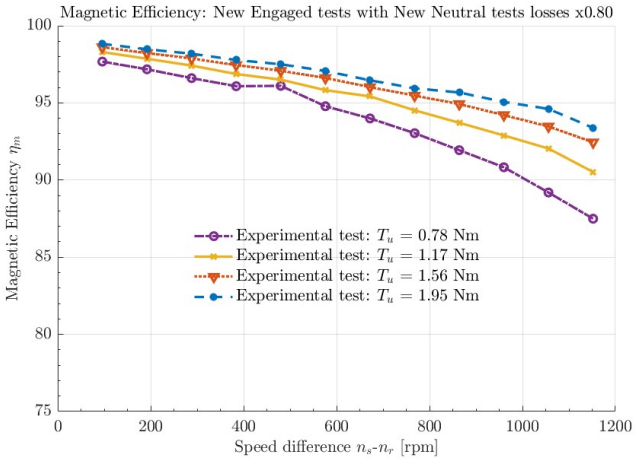

(c) New Engaged tests with New Neutral losses x0.8.

Figure 4.25: Magnetic Efficiency comparison across all engaged datasets.

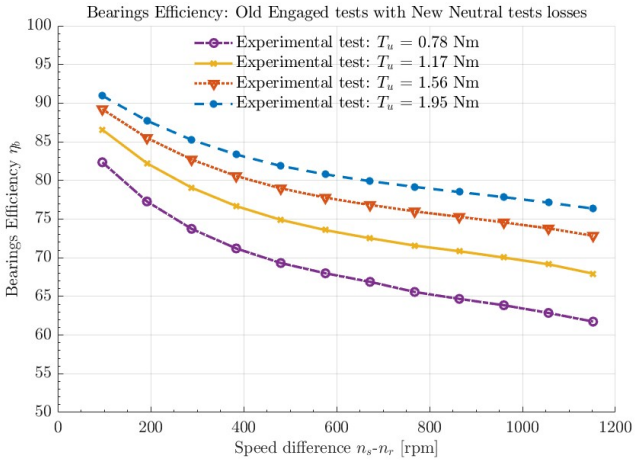

(a) Old Engaged tests with New Neutral losses.

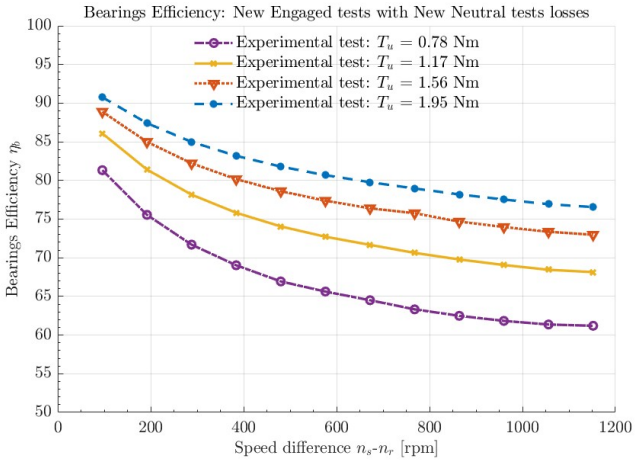

(b) New Engaged tests with New Neutral losses.

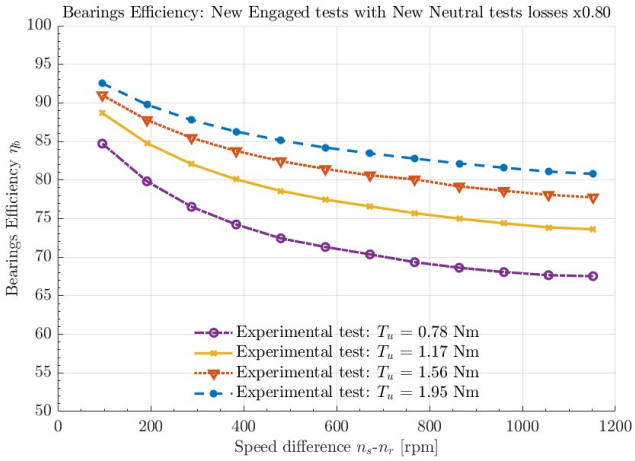

(c) New Engaged tests with New Neutral losses x0.8.

Figure 4.26: Bearings Efficiency comparison across all engaged datasets.

Chapter 5

Dynamic Model of the Prototype

In the previous chapters, the physical prototype of the Planetary Magnetic Gearbox (PMG) and the related experimental tests performed were analysed. While chapter 3 described the general architecture of the gearbox and of the test bench, chapter 4 detailed the losses and performances of the physical system through the analysis of neutral and engaged tests, finalised to a separation of the mechanical and magnetic contributions.

In this chapter, the focus is shifted towards the development of the dynamic model of the PMG in Simulink software, in order to replicate the system behaviour under real operating conditions, without having to physically interact with the real prototype. To do so, the model was designed to represent the test bench under analysis with a high degree of fidelity, incorporating the real physical and dynamic parameters of the prototype's components. The result is a simulation environment that allows to explore the system's response under different inputs and loads configurations, in order to further validate the theoretical assumptions and experimental results, as well as predict the PMG performance in conditions that are not easy to directly analyse on the test bench.

In section 5.1 the whole Simulink model is shown and described to provide a general view of the system, highlighting the main interactions between its different subsystems and its signal flow. The most important subsystem is the magnetic gearbox itself, which is described in section 5.2. The bearings mounted on the PMG assembly are modelled in section 5.3, where the results of the neutral tests are used to tune the torque and power loss parameters. In section 5.4 the model of the actuators on the test bench is defined, while the inertia and transmission subsystems are analysed in section 5.5 to complete the structure of the model.

The Simulink model described in this chapter will be used to perform the simulation analysis presented in the chapter 6, where the behaviour of the model will be compared with the experimental results obtained in chapter 4.

5.1 Complete Dynamic Model Overview

The design of a dynamic model of the Planetary Magnetic Gearbox prototype is the main topic of this work. This model was developed in Simulink environment with the objective to build a one-to-one replica of the test bench described in chapter 3, creating

a digital copy of the prototype. The biggest advantage derived from the creation of this digital twin is the ability to simulate the real system behaviour under various operating conditions, making it possible to replicate and validate the experimental tests, as well as allowing the analysis of additional operating scenarios which study would prove difficult to perform on the physical test bench.

In order to achieve these goals, the Simulink model was designed to resemble both visually and mathematically the architecture of the test bench. All the parameters used in the model were taken from the real components' datasheets or from the results of the experimental tests previously shown in chapter 4. Some parameters, however, proved difficult to acquire, and fitting procedures with the experimental results had to be performed to make an estimated guess of them.

A simplified schematic of the Simulink dynamic model, deprived of any auxiliary control panel that would increase the level of complexity of the figure, is shown in Figure 5.1.

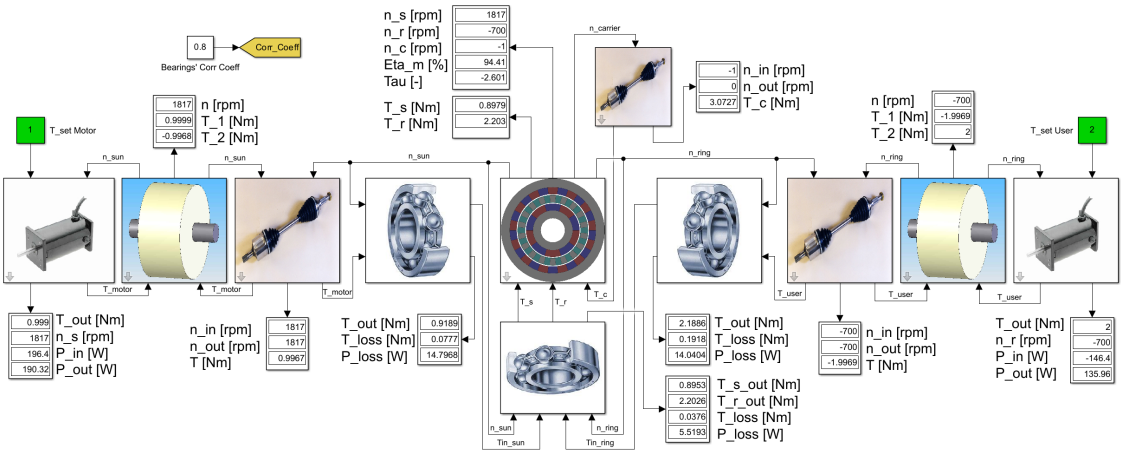

Figure 5.1: Simplified scheme of the Simulink model representing the PMG test bench.

The main subsystems that are present in the model architecture are summarised in Table 5.1, where their purpose and modelling approach are also highlighted.

Subsystem	**Purpose**	**Modelling Approach**
Motors	Apply input and resistive torque	Standard mechatronic dynamic model
Inertias	Represent rotating masses	Lumped parameter blocks
Transmissions	Transfer torque and speed	Ideal torque-speed links
Bearings	Model mechanical losses	Lookup tables from neutral tests
PMG	Simulate magnetic torque transmission	FEM-based lookup table + dynamic model interaction

Table 5.1: Simulink model subsystems overview.

To better highlight the signal flow between the components, a cleaned up version of the complete dynamic model is shown in Figure 5.2.

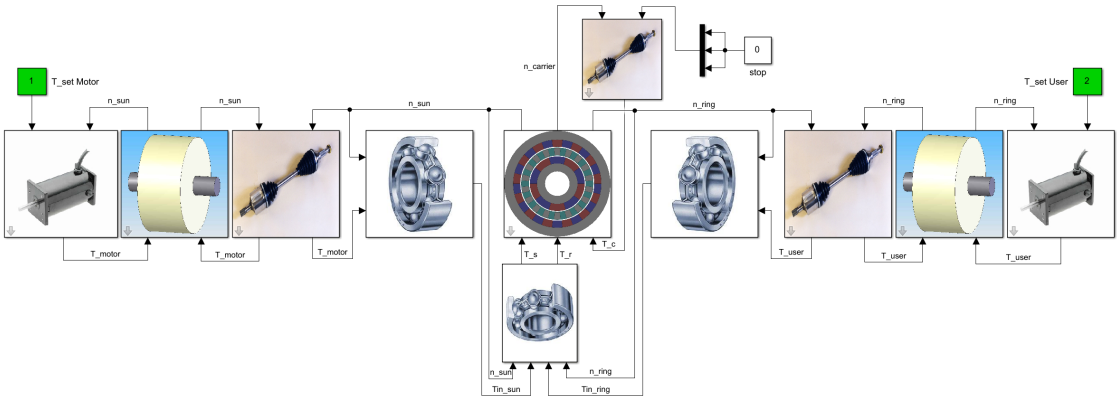

Figure 5.2: Simplified signal flow visualisation of the Simulink model.

The overall signal direction is from the left side of the model, where the motor mounted on the sun side receives the input torque signal, and across all the system's blocks, reaching the user motor positioned on the right, where the user torque load is applied. This left-to-right direction is also reflected by the overall power cascade of the system.

To provide a more detailed overview of the system, the whole model architecture can be divided into three main branches: the sun side, the ring side and the carrier side.

5.1.1 Sun Branch

The sun side of the model, where the input torque is applied, is shown in Figure 5.3.

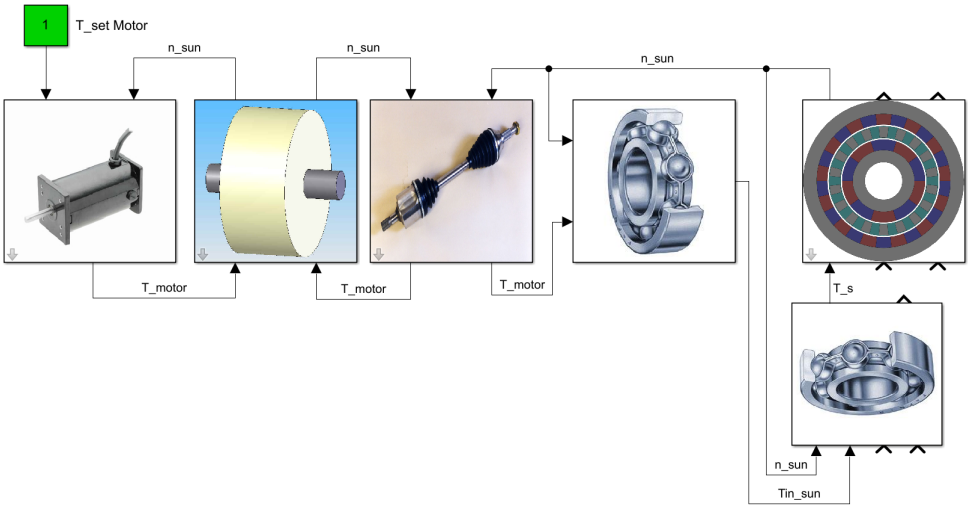

Figure 5.3: Sun side of the Simulink model.

The torque signal flow starts from the green block $T_{set}Motor$, representing the torque set provided to the motor on the sun shaft, designed in torque control mode, and proceeds on the bottom path passing through the inertia, transmission, sun bearings, and relative bearings blocks, up to the PMG subsystem. Here, the output speed n_{sun} is computed as a function of the dynamic and magnetic interaction between the gears, and is propagated backwards on the upper path, passing through all blocks in the opposite direction and reaching the motor subsystem as a feedback signal.

5.1.2 Ring Branch

The ring side of the model is instead shown in Figure 5.4.

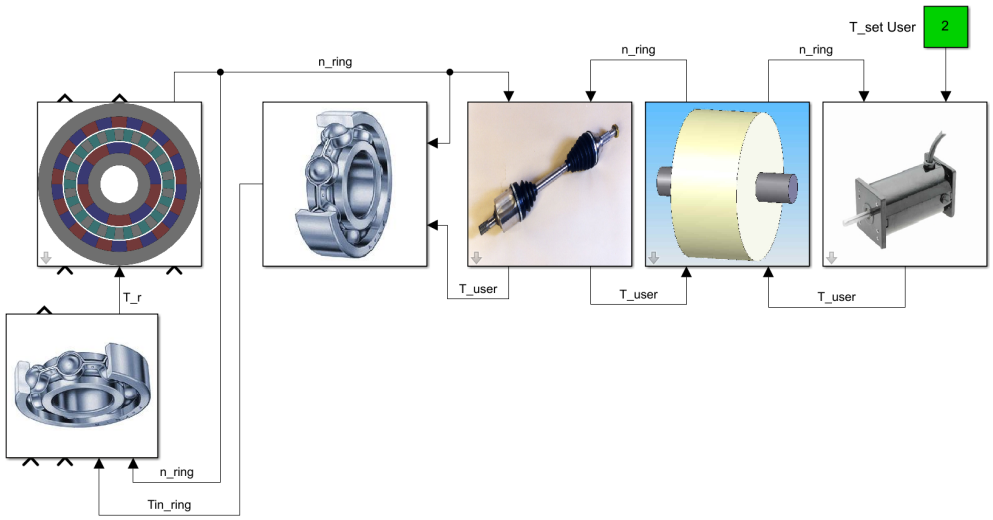

Figure 5.4: Ring side of the Simulink model.

This section represents the output branch of the system, where the torque transmitted by the magnetic gears interaction is used by the ring shaft motor, designed once again in torque control and acting like a user load.

In particular, following the bottom torque signal path, the input to this side is provided to the motor block by means of a $T_{set}User$ block, which defines the resistive load applied to the ring gear. The motor block is then actuated to follow this requirement and sends this load signal T_{user} across inertia, transmission, ring bearings, and relative bearings blocks up to the PMG subsystem. The interaction between the sun and ring gears provides a magnetic torque that, if higher than the user load requested, puts the ring side into movement, providing the speed signal n_{ring} that runs through the upper path. In the same way as described on the sun side, this speed signal runs in the opposite direction to the torque signal and ends up being the feedback signal for this side's motor.

5.1.3 Carrier Branch

The last branch that makes up this dynamic model's architecture is the carrier side, which is shown in Figure 5.5.

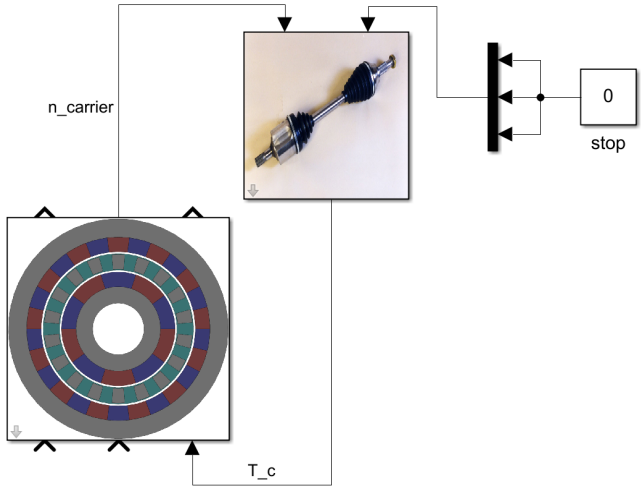

Figure 5.5: Carrier side of the Simulink model.

In the physical prototype of the Planetary Magnetic Gearbox, the carrier is kept in a fixed, non-rotating position to enable the torque transmission between the sun and ring gears. This constraint is replicated in the Simulink model by the adoption of a transmission block that presents a boundary condition to one of its rotational degrees of freedom. The result is a T_c torque applied to the PMG subsystem that is exactly what's needed to keep the carrier speed $n_{carrier}$ constantly null in its dynamic equations.

5.2 Magnetic Gearbox Subsystem

The main component of the Simulink dynamic model is the Planetary Magnetic Gearbox subsystem. This block represents the most complex subsystem to design, due to the highly non-linear interactions and dynamic coupling between its main components: the sun, ring, and carrier gears. Its schematic representation is shown in Figure 5.6.

The PMG subsystem receives three input torques, represented by the green blocks, each applied to one of the three gears. These torques are then sent to a Matlab function block called "Dynamic PMG", where alongside the magnetic torques transmitted between the gears and the feedback velocities signals, as well as the PMG parameters such as inertias and damping coefficients, the dynamic equations of the system are computed. The result of these dynamic equations is represented by the angular acceleration of each gear, that are then integrated to angular speed and angular position. These three characteristic signals of each gear are then combined and make up the output of the PMG block.

The angular velocities of the gears are sent back into the Matlab function block, while the angular position of sun and ring gear are sent back in the loop, transformed into

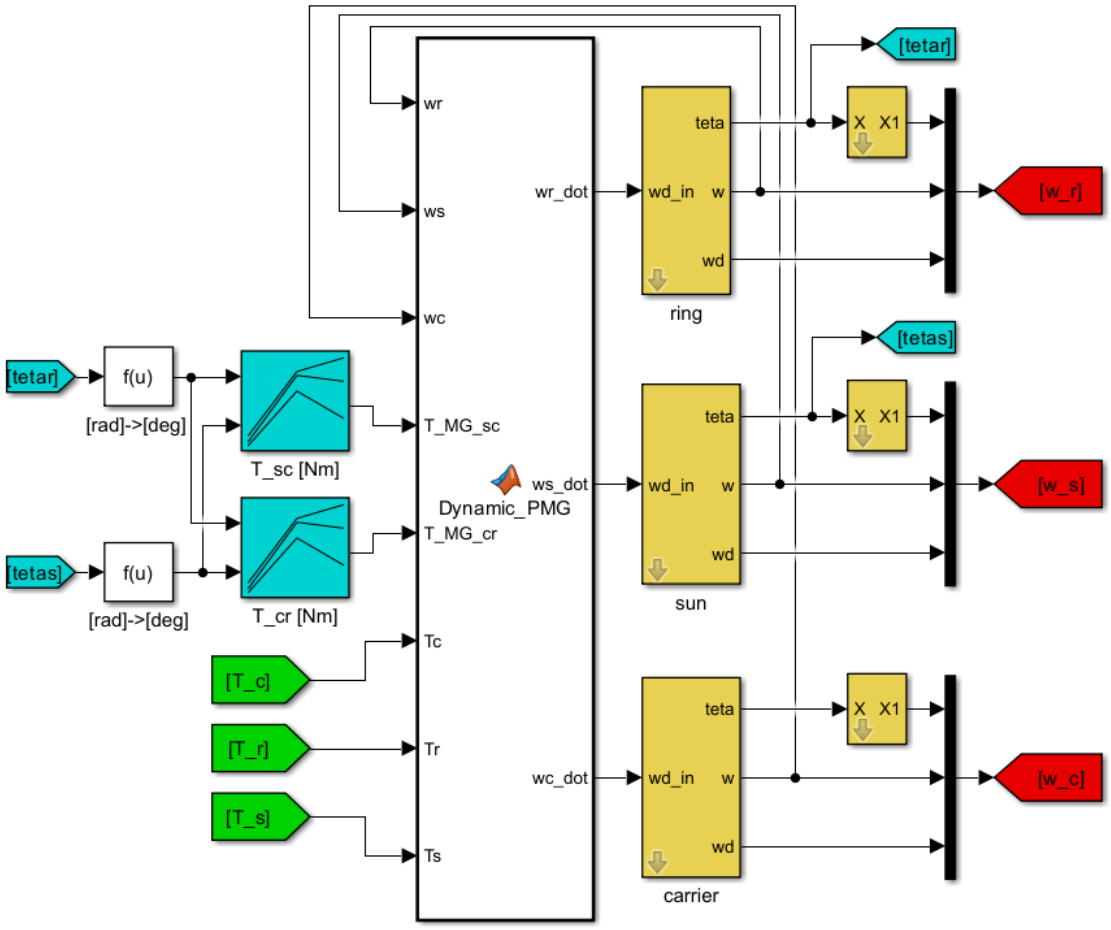

Figure 5.6: Simulink structure of the PMG subsystem.

degrees and passed through LookUp Tables to compute the magnetic torques transmitted between the gears, which are used in the previously described dynamic computations.

To fully understand how the working principle of this block, it is necessary to further investigate how the magnetic torques and the dynamic equations are computed.

5.2.1 Magnetic Torque Computation

The way the magnetic torque transmission is modelled inside the PMG subsystem is the result of the theoretical knowledge that was introduced in subsection 2.3.4, where the use of the Maxwell Stress Tensor, supported by punctual FEM analysis, provided two different torque maps as a function of the angular position of the sun and ring gears, as seen in Figure 2.10.

In this Simulink model, the same concept has been implemented by the use of scaled down versions of the same torque maps previously mentioned, purposely tuned to represent the actual torque interactions happening in the physical prototype. These maps have been introduced into the LookUp tables present in the PMG model (the T_{sc} and T_{cr}

blue blocks on the left side of Figure 5.6) and are shown in both 2D and 3D configuration in Figure 5.7 and Figure 5.8 respectively to highlight their dependence to the angular position of the sun and ring gears.

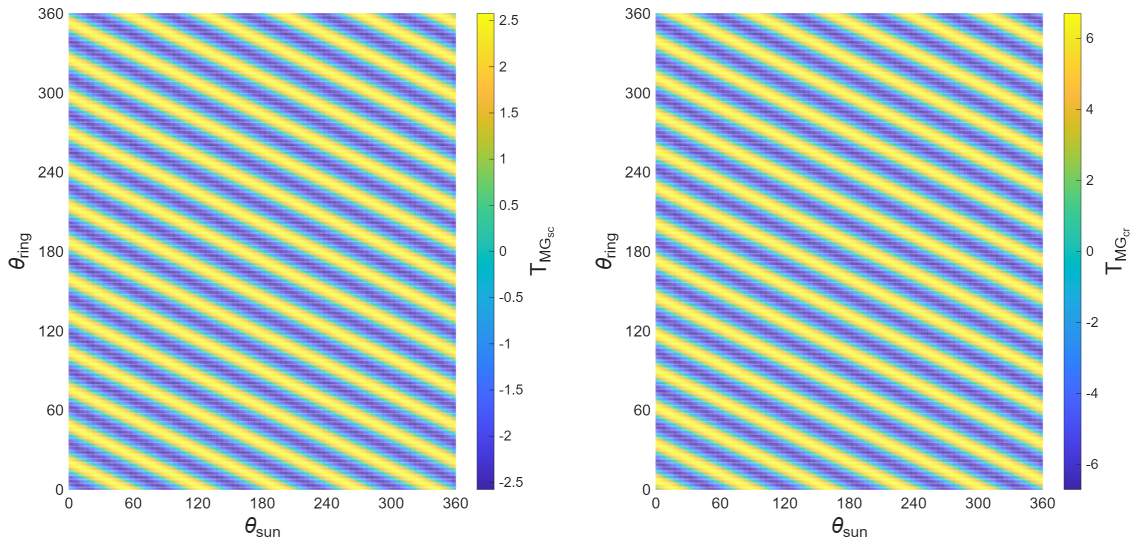

Figure 5.7: 2D representation of the magnetic stiffness torque transmitted between sun and carrier (left) and between carrier and ring (right).

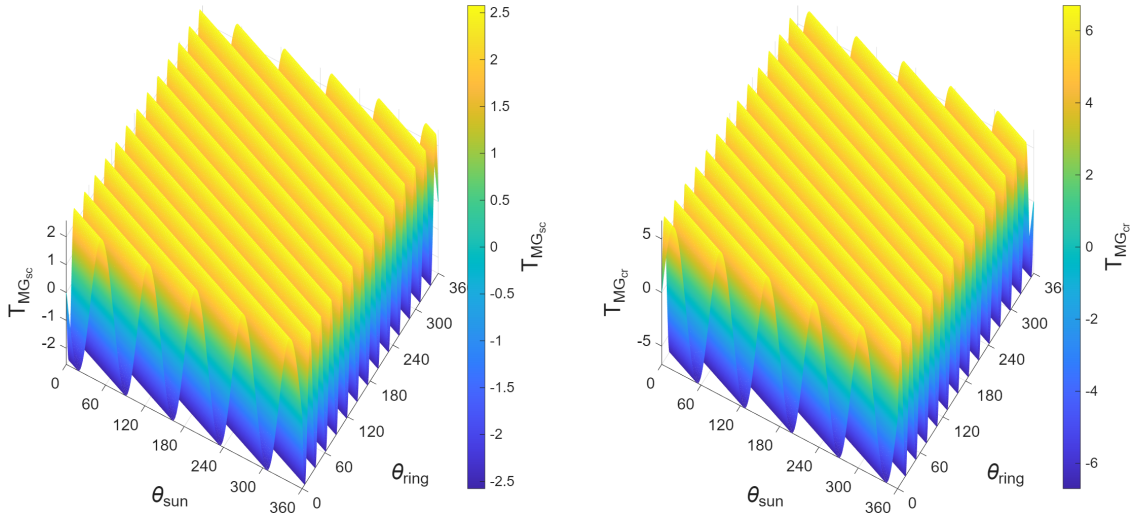

Figure 5.8: 3D representation of the magnetic stiffness torque transmitted between sun and carrier (left) and between carrier and ring (right).

The torque maps show a periodic and non-linear trend and represent the magnetic stiffness present in the system between the sun and carrier and between the carrier and the ring. They are computed at each simulation cycle based on the angular position of sun and ring and play a major role in the computation of the dynamic equations of

motion of the PMG block.

5.2.2 Dynamic Equations Computation

The theory behind the dynamic modelling of the PMG subsystem was already presented in section 2.4, where the Free Body Diagrams (FBD) of the sun, carrier and ring gears were built and the Equations of Motion (EoM) were derived. For clarity, the FBD is shown once again in Figure 5.9, as well as the derived EoM in Equation 5.1.

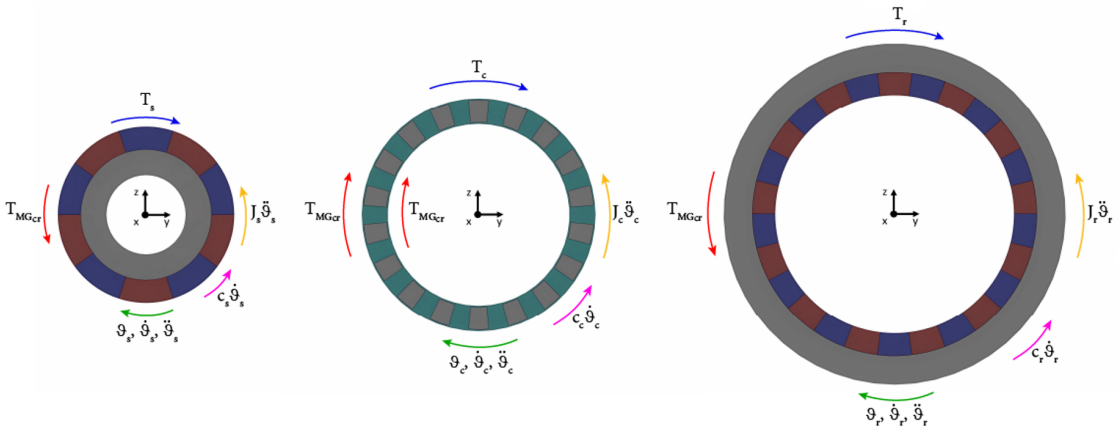

Figure 5.9: Free Body Diagram of the three gears.

$$\begin{bmatrix} J_s \\ J_c \\ J_r \end{bmatrix} \begin{Bmatrix} \ddot{\theta}_s \\ \ddot{\theta}_c \\ \ddot{\theta}_r \end{Bmatrix} = \begin{Bmatrix} T_s \\ T_c \\ T_r \end{Bmatrix} - \begin{bmatrix} c_s \\ c_c \\ c_r \end{bmatrix} \begin{Bmatrix} \dot{\theta}_s \\ \dot{\theta}_c \\ \dot{\theta}_r \end{Bmatrix} - \begin{Bmatrix} T_{MG_{sc}} \\ -T_{MG_{sc}} - T_{MG_{cr}} \\ T_{MG_{cr}} \end{Bmatrix} \tag{5.1}$$

The magnetic torques derived from the torque maps were introduced as the coupling stiffness terms of the equations, while the inertia and damping contributions made up the remaining terms of the dynamic system alongside the input torques.

In the Simulink model, these equations are expanded by the inclusion of a more detailed damping modelling, which will further increase the accuracy of the dynamic results. In particular, the damping losses are made up of three different components for each gear, which are:

- Hysteretic damping: a constant torque term that is not dependent on the speed and that models the internal material friction and deformation of the material.
- Eddy current damping: a term proportional to the angular speed and that models the losses due to the induced currents in ferromagnetic components.
- Excess loss damping: a term that is proportional to the square root of the speed and that models the additional losses at higher speeds that are caused by magnetic interactions.

These damping contributions are not easily determinable and a fitting procedure was necessary for their correct evaluation. This fitting process was performed on the engaged tests results shown in subsection 4.4.3, and on Figure 4.18 in particular. The simulated magnetic power losses were superposed on the experimental curves and, by means of an iterative process, the damping coefficients were adjusted to minimise the difference between the two sets of values. The results of this procedure is a model that can better approximate the magnetic energy dissipation encountered in the physical prototype. This fitting procedure will be further explained in chapter 6.

Adding these contributions and solving for the angular acceleration of the three gears, the equations found in 5.1 can be rewritten as follows:

$$\dot{\omega}_s = \frac{T_s - T_{MG,sc} - b_s - c_s\omega_s - d_s\omega_s^{0.5}}{J_s} \tag{5.2}$$

$$\dot{\omega}_c = \frac{T_c + T_{MG,sc} + T_{MG,cr} - b_c - c_c\omega_c - d_c\omega_c^{0.5}}{J_c} \tag{5.3}$$

$$\dot{\omega}_r = \frac{T_r - T_{MG,cr} - b_r - c_r\omega_r - d_r\omega_r^{0.5}}{J_r} \tag{5.4}$$

where:

- T_s, T_c and T_r are the external torques applied to sun carrier and ring gears;
- $T_{MG_{sc}}$ and $T_{MG_{cr}}$ are the magnetic stiffness torques transmitted from sun to carrier and from carrier to ring respectively;
- ω_s, ω_c, ω_r and $\dot{\omega}_s$, $\dot{\omega}_c$, $\dot{\omega}_r$ are the angular speeds and accelerations of the gears;
- J_s, J_c and J_r are the inertias of the three gears;
- b_s, b_c and b_r are the Hysteretic damping contribute to the overall damping losses;
- c_s, c_c and c_r are the Eddy current damping contribute to the overall damping losses;
- d_s, d_c and d_r are the Excess loss damping contribute to the overall damping losses.

These equations are implemented in the Matlab function block called "Dynamic PMG" and allow the computation of the necessary rotational acceleration outputs that are integrated and sent as outputs of the PMG subsystem.

5.3 Bearings Subsystem

An essential subsystem that makes up the dynamic model architecture is the Bearing subsystem, which introduces the mechanical losses measured during the neutral tests performed on the test bench. As previously described in subsection 3.1.3, and as shown in Figure 5.10, the physical prototype includes a set of bearings distributed along the sun and ring shafts, as well as a relative bearing positioned between them.

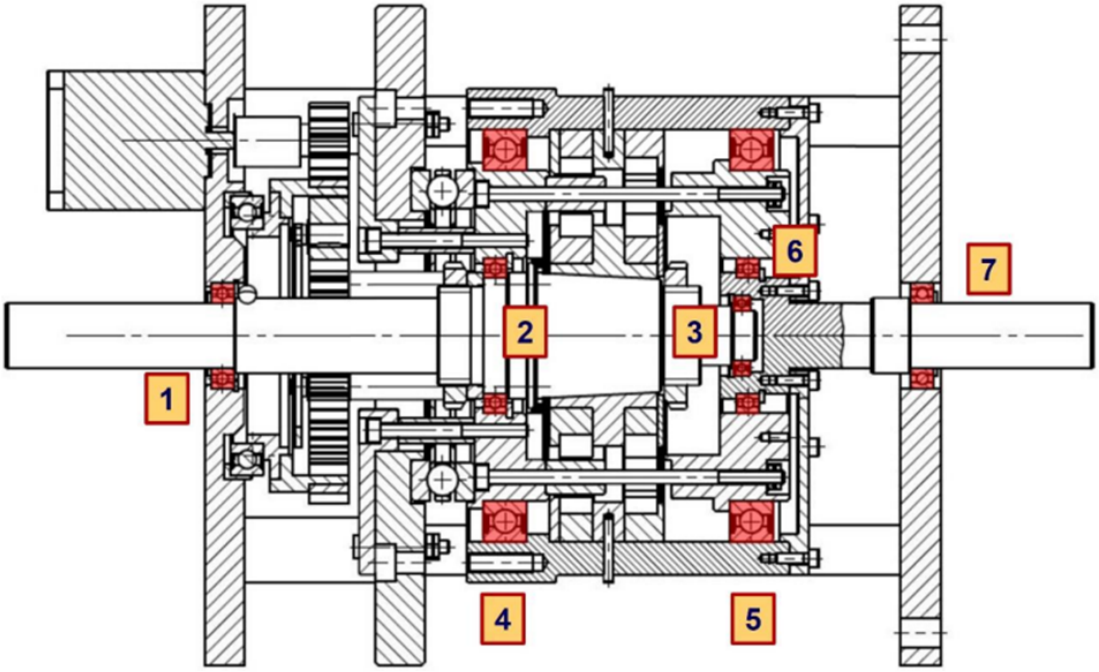

Figure 5.10: Bearings identification in the prototype assembly.

All 7 bearings making up the assembly have been singularly analysed, and a torque loss value has been attributed to each of them. To achieve so, it was necessary to find a way to divide the losses obtained during the neutral set of tests among them. The method used in this work was a division based on the dimension of the bearings, i.e. their diameter. This subdivision is schematised in Table 5.2 and will be used to further detail the Bearings subsystems in study.

ID	**SKF Model**	**Position**	**Diameter**	**% of Sun Neutral Losses**	**% of Ring Neutral Losses**
1	W 61804-2Z	Sun	32mm	31.1%	
2	W 61807-2Z	Sun	47mm	45.6%	
3	W 61802-2Z	Relative	24mm	23.3%	6.8%
4	61820-2RZ	Ring	125mm		35.4%
5	61820-2RZ	Ring	125mm		35.4%
6	W 61807-2Z	Ring	47mm		13.3%
7	W 61804-2Z	Ring	32mm		9.1%

Table 5.2: Bearings torque losses subdivisions.

These 7 bearings have been grouped up in the Simulink model across three separate blocks: sun side Bearings block, ring side Bearings block and relative bearing block.

5.3.1 Sun Side Bearings Block

The schematic representation of the bearing block situated on the sun branch is shown in Figure 5.11. This block models the mechanical losses associated with the bearings mounted on the sun shaft of the assembly, that correspond to bearings 1 and 2 of Figure 5.10.

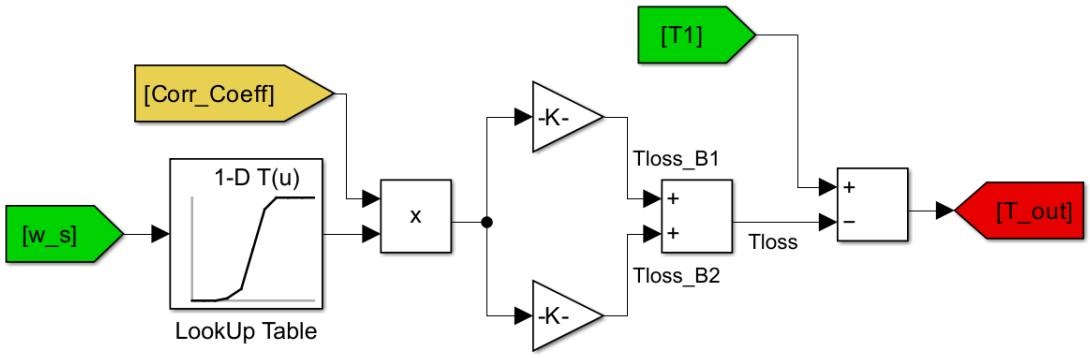

Figure 5.11: Simulink structure of the Sun side Bearings subsystem.

This subsystem has two inputs, the sun shaft speed w_s and input torque T_1, corresponding to the torque provided by the sun side motor, and one output consisting of the residual torque T_{out}. The shaft speed enters a LookUp Table which output is the torque loss on the sun side as a function of the input speed. This value represents the total torque losses registered on the sun side during the neutral tests performed in subsection 4.3.1. To account for the correction factor introduced to eliminate the contribution of the residual magnetic losses from the mechanical bearings losses, this output is multiplied by the "Corr Coeff" block, whose value is lower than 1.

This corrected torque loss is then split into two separate branches bearing 1 and 2. The distribution of the torque loss on each of them has been determined based on the relative size of every bearing that contributed to the neutral losses results for the sun side, as presented in Table 5.2, which is:

- Bearing 1: 31.1% of total sun-side losses;
- Bearing 2: 45.6% of total sun-side losses.

The remaining 23.3% is accounted for by bearing 3, which is modelled separately in another block. The torque losses from bearings 1 and 2 are then summed to obtain the total torque loss of this subsystem and subtracted to T_1 to obtain the output torque value.

5.3.2 Ring Side Bearings Block

For what concerns the bearings 4, 5, 6 and 7, mounted on the ring shaft, their torque loss contribution was modelled as shown in Figure 5.12. The overall structure of this block is the same as the sun-side counterpart, but with some key differences.

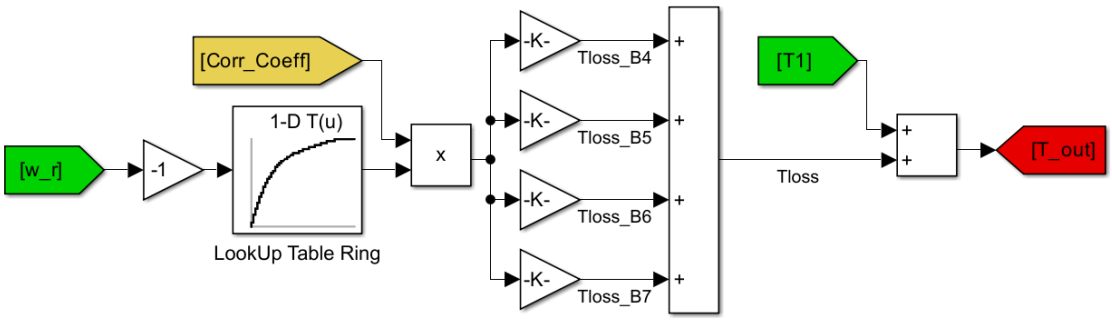

Figure 5.12: Simulink structure of the Ring side Bearings subsystem.

The two inputs that the block receives are the ring shaft speed w_r and the requested user torque T_1, while the output is the required torque T_{out}. Due to the sign convention adopted in the model, under normal operating conditions, the ring shaft speed is negative because it rotates in the opposite direction of the sun shaft, assumed positive by choice. Since the LookUp Table used to compute the ring side bearings losses was built with positive speed values during the neutral tests, the input speed has to first be corrected by a -1 factor. The output of the LookUp Table is once again scaled down using the same correction coefficient adopted to isolate the mechanical torque losses, which is then distributed among the four bearings as seen in Table 5.2:

- Bearing 4: 35.4% of total ring-side losses;
- Bearing 5: 35.4% of total ring-side losses;
- Bearing 6: 13.3% of total ring-side losses;
- Bearing 7: 9.1% of total ring-side losses.

Once again, bearing 3, which contribution amounts to 6.8% of the ring-side losses, is not considered in this block and will be modelled separately. The torque losses of the four bearings are then summed up and they are added to the user requested torque to obtain the output requested torque, unlike what has been done on the sun-side counterpart, where they were detracted instead. This difference comes from the fact that the ring gear has to overcome the user load as well as the friction losses present on its shaft, in order to keep the desired working condition.

5.3.3 Relative Bearing Block

The relative bearing has been modelled separately from the other bearings configurations. This is due to its position, between the sun and ring shafts, meaning that it contributes

to the mechanical losses of both sides of the system. Its schematic structure is shown in Figure 5.13.

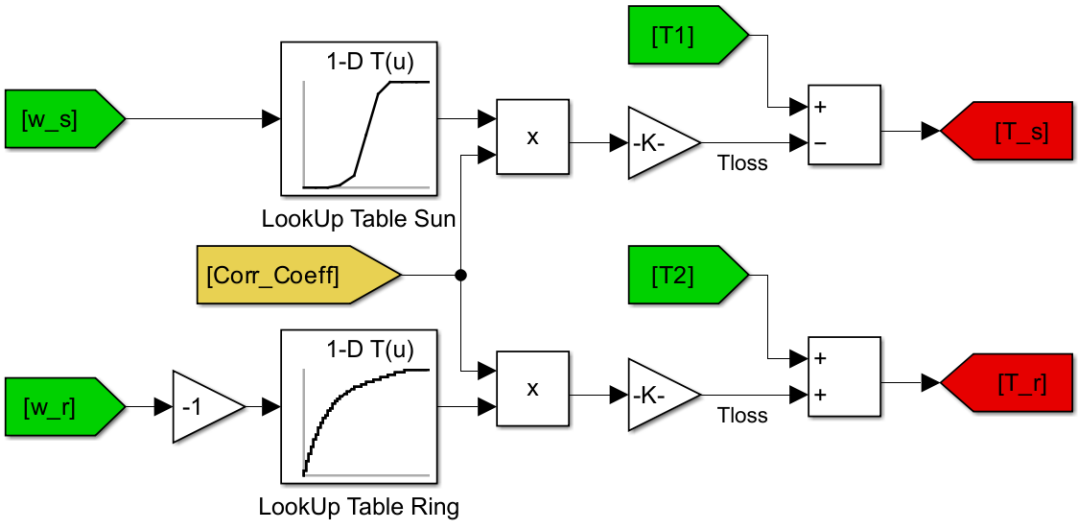

Figure 5.13: Simulink structure of the Relative Bearing subsystem.

To reflect its build, the relative bearings has four different inputs, the two shaft speeds w_s and w_r as well as the two input torques T_1 and T_2. The outputs are the two torques T_s and T_r that correspond to two of the inputs of the PMG subsystem. The peculiarity of this block is that it is divided into two independent branches: the upper one is for the sun side losses while the bottom one accounts for the ring side ones. Each branch is passed through the respective LookUp table and multiplied by the same corrective coefficient and by the relative contribution of bearing 3, as presented in Table 5.2, which is:

- 23.3% of total sun-side losses;
- 6.8% of total ring-side losses.

Then, the torque losses relative to the sun branch are deducted from the torque provided to the sun gear, while the losses relative to the ring branch are instead added to the torque requested from the ring gear.

On a final note, the modelling of bearing 3 could have been included separately in the sun side and ring side blocks for simplicity. However, it was designed separately to allow for the independent evaluation of its torque and power losses, making possible a more detailed comparison with the other bearings groups.

5.4 Motors Subsystem

The dynamic model includes two motor blocks, each one representing on of the brushless DC motors that are installed on the physical test bench. One motor is connected to the sun shaft and acts as the system's driver, while the other is connected to the ring shaft

and acts as the system's user load. Although it would have been ideal to operate the sun shaft motor in speed control and the ring shaft motor in torque control, as done during the engaged experimental tests, both motors were designed in torque control due to modelling constraints. However, this choice allowed to adopt a consistent and unified control strategy that greatly simplified the overall system's architecture.

5.4.1 Sun Shaft Motor

The simplified structure of the motor connected to the sun shaft is shown in Figure 5.14.

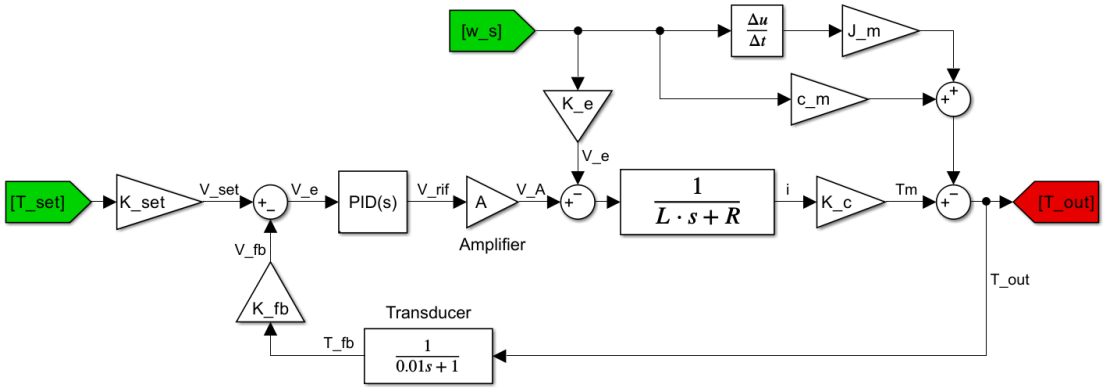

Figure 5.14: Simulink structure of the Sun shaft Motor subsystem.

The two inputs are the set torque T_{set} defined by the user and the feedback shaft speed ω_s, while the output is the motor torque T_{out} that drives the sun shaft and the overall dynamic model.

The motor is modelled following the typical DC motor mechatronic representation, which includes both electrical and mechanical subsystems, as well a PID control strategy in a closed loop environment. In particular, the user torque T_{set} is first converted into a voltage signal V_{set} by the adoption of a gain block K_{set} and then compared to the feedback voltage V_{fb} to obtain the voltage error V_e:

$$V_e = V_{set} - V_{fb} \tag{5.5}$$

The feedback is measured from the output torque by a first order transducer to obtain the feedback torque T_{fb} and then transformed into a voltage signal V_{fb} by the adoption of the feedback gain K_{fb}, designed using the same gain value as the set. The adoption of a first order transfer function to model the feedback transducer simulates the delay and the filtering effect that a real torque sensor would provide.

The voltage error V_e is then processed by a PID controller, which adjusts the control signal to send to the motor in order to minimise the error over time. The main components of the PID controller are:

- Proportional control K_p: component that reduces the current error.
- Integral control K_i: component that reduces the steady-state error.

- Derivative control K_d: component that reduces future error based on its change rate.

The PID controller's output is the reference voltage V_{rif}, that is computed as:

$$V_{rif}(t) = K_p \cdot V_e(t) + K_i \cdot \int_0^t V_e(t) \cdot dt + K_d \cdot \frac{dV_e(t)}{dt} \tag{5.6}$$

that in Laplace Domain is:

$$V_{rif}(s) = V_e(s) \cdot \left(K_p + \frac{K_i}{s} + K_d \cdot s \right) \tag{5.7}$$

The reference voltage passes through the amplified block to obtain the amplified voltage V_a which drives the motor.

This amplified voltage is reduced by the Back Electromotive Force (back-EMF), a voltage that is generated by the rotation of the motor, proportional to its rotation, and acts as a disturbance in the voltage supply, reducing the voltage available to the motor. The resulting voltage is then passed through a first order transfer function that represents the Electromagnetic System equation of the motor. In formulas:

$$V_a - K_e \omega_s = R \cdot i + L \frac{di}{dt} \tag{5.8}$$

Using Laplace Transforms and solving for the current i, the final formulation is:

$$i = (V_a - K_e \omega_s) \cdot \frac{1}{L \cdot s + R} \tag{5.9}$$

where:

- R is the motor's resistance;
- L is the motor's inductance;
- K_e is the back-EMF constant;
- s is the Laplace variable.

The motor current is then converted in torque using the DC Motor Characteristic equation, by using the torque constant K_c:

$$T_m = K_c \cdot i \tag{5.10}$$

The final output torque is finally computed taking into account the Mechanical System equation:

$$T_{out} = T_m - J_m \cdot \frac{d\omega_s}{dt} - c_m \cdot \omega_s \tag{5.11}$$

where:

- J_m is the motor's inertia;
- c_m is the motor's damping coefficient.

The generated T_{out} is what provides the driving torque to the sun shaft.

5.4.2 Ring Shaft Motor

The simplified structure of the motor connected to the ring shaft is shown in Figure 5.15.

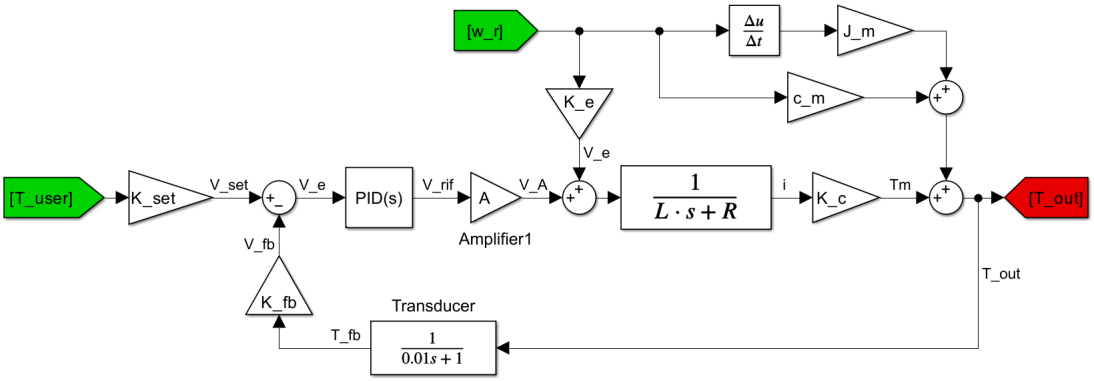

Figure 5.15: Simulink structure of the Ring shaft Motor subsystem.

This motor is responsible for the user load to be applied to the ring shaft of the PMG system. The architecture is structurally identical to the one described for the other motor, but some differences are present to highlight its function as a load rather than as a driver.

The two inputs are, in this case, the requested load T_{user}, defined by the user, and the ring shaft speed ω_r, while the output is the torque T_{out} requested by the ring to satisfy the load requirements. The user torque is once again transformed into a voltage signal, compared to the feedback, and then controlled by a PID having the same structure as previously discussed.

The signal is amplified and, differently from the sun motor case, the back-EMF voltage is now added. This difference with the sun shaft motor exists because the ring motor acts like a load generator, and, therefore, the output torque has to withstand the losses inside the motor itself to provide the requested load.

The newly computed voltage enters once again the electromagnetic transfer function block and is multiplied by the torque constant K_c. Then, unlike what seen in the sun motor, where the motor torque is reduced by the mechanical losses to compute its output torque, in the ring motor those mechanical losses are added to the torque the motor provides to meet the user load request output.

5.5 Inertias and Transmissions Subsystem

The last two subsystems that make up the Simulink dynamic model of the prototype under study are the inertia and transmission blocks. While they are not as important as the other subsystems in the construction of the of the digital model, they still play an essential supporting role in completing its architecture. The inclusion of these blocks makes possible to replicate the dynamics of the system with a higher level of realism, especially for what concerns torques and speeds propagations

5.5.1 Inertias Subsystem

The inertia subsystem models the rotational inertia of the sun and ring shafts. A total of two inertia blocks are present in the model, one on the sun shaft and one on the ring shaft, and their simplified architecture is shown in Figure 5.16.

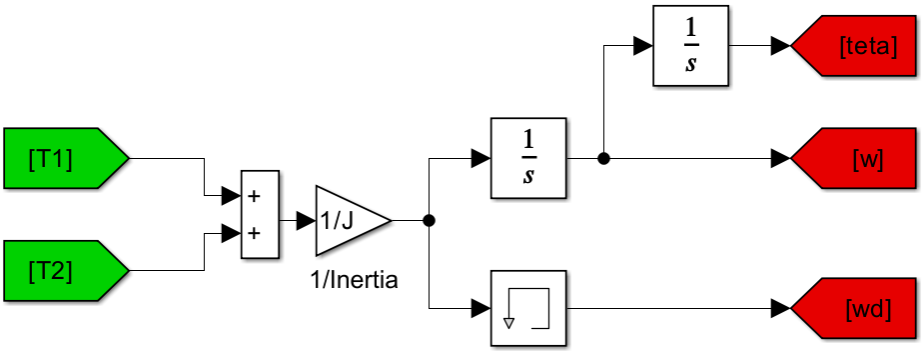

Figure 5.16: Simulink structure of the Inertia subsystem.

The two inputs are the torques received at both hands of the block, while the outputs are the resulting angular acceleration, velocity and position of their shaft.

Their design approach is very simple: the net torque acting on the inertia is computed as the algebraic sun of the two input torques (the two torques have opposite signs as they're applied with opposite directions) and then divided by the inertia value to compute the angular acceleration. The acceleration is also integrated once to obtain the angular position and a second time to calculate the angular position of the shaft.

The inertia J value used in the sun and ring inertia blocks was computed by summing the individual inertias of all the rotating masses associated with the corresponding shaft in the physical prototype. This verifies that the simulations can accurately reflect the transient behaviour of the system.

5.5.2 Transmission Subsystem

The transmission subsystems are used to simulate the elastic and damping behaviour of the torsional joints of the prototype. Additionally, their implementation also allows to decouple the dynamic response of each inertia block, improving the numerical stability of the simulation environment. The simplified structure of the transmission blocks used on the sun and ring sides is shown in Figure 5.17.

Each block receives four inputs, the two angular positions and velocities at both ends of the transmission, and one output that is the torque transmitted through the elastic joint. The transmitted torque is computed as follows:

$$T = k_t \cdot (\theta_1 - \theta_2) + c_t \cdot (\omega_1 - \omega_2) \tag{5.12}$$

where:

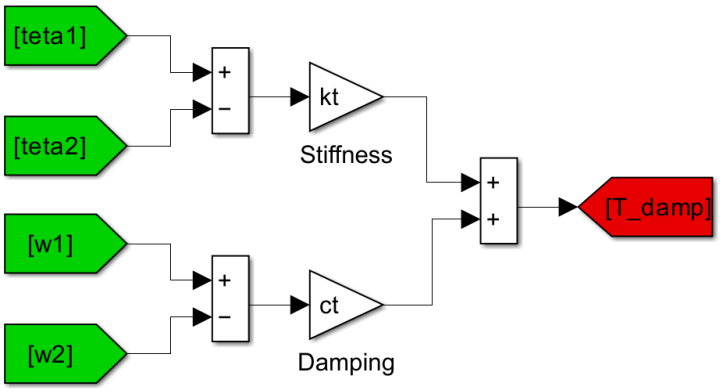

Figure 5.17: Simulink structure of the Transmission subsystem.

- k_t is the torsional stiffness coefficient;
- c_t is the torsional damping coefficient.

This equation allows to compute both the elastic response of the joint due to its angular displacement and the viscous damping due to its speed differential. The resulting torque value is then applied to both ends of the transmission block, securing a smooth torque transmission.

Carrier Transmission Constraint

In addition to the more conventional transmission blocks situated on the sun and ring side of the model, an additional block was used to block the carrier gear. Unlike the other two blocks, this block is not used as an elastic joint to transfer torque on the signal paths, but rather to apply a boundary constraint to the carrier. The structure of this block is shown in Figure 5.18.

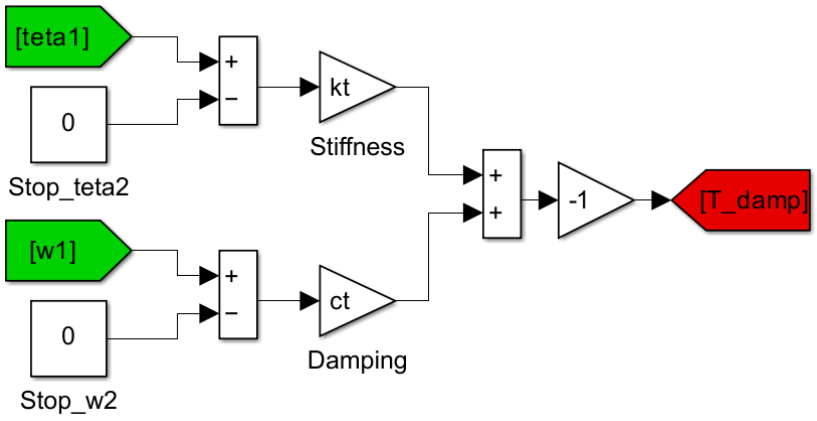

Figure 5.18: Simulink structure of the Carrier Transmission subsystem.

The main differences in the design of this block are that the second degree of freedom, made up by the second set of inputs θ_2 and ω_2, is fixed at zero, and that the final torque sign is changed. The result is a torque acting as a reaction torque, that prevents any movement of the carrier.

Chapter 6

Model Simulated Tests

In the previous chapter, the main architecture of the Simulink dynamic model of the Planetary Magnetic Gearbox (PMG) was described. The main components that made up the model were the magnetic torque maps used in the PMG block, derived from previous FEM analysis, to extract the transmitted magnetic torque necessary for the computation of the block's dynamic equations, the torque loss maps introduced in the bearings blocks to implement the mechanical losses measured in the neutral tests, and the electromagnetic-mechanical equations of the motors. The model has then been completed by the adoption of sub-components, such as inertias and transmissions, that would help the correct functioning of the system.

This chapter completes the description of the designed dynamic model of the PMG by presenting the results obtained by the simulations performed on it, as well as a comparison with the experimental results previously displayed in chapter 4. The main goals are to simultaneously check the accuracy of the model in reproducing the dynamic behaviour of the prototype in its first gear configuration under various operating conditions, as well as validate the experimental tests performed. In order to achieve these objectives, a very important step was the research of the correct fitting of the damping coefficients of the PMG block, a very important set of parameters that directly affect the losses and performance results of the dynamic model. Additionally, the correct evaluation of the correction factor used to account for the residual magnetic losses in the neutral configuration was found to be mandatory, as it was studied that the best fitting of the damping coefficients was dependent on it.

In section 6.1 the setup adopted to perform the simulations is described as well as the test scenarios used to replicate the experimental tests. Section 6.2 describes the fitting procedure adopted for the computation of the PMG's damping coefficients, as well as the final evaluation of the correction factor. In section 6.3, the transient results of the PMG's transmitted torques, speeds and powers of a reference simulation are investigated, while in section 6.4 the steady state values of the main quantities are analysed, and in particular the power losses, efficiencies and power transmission chain. Finally, section 6.5 presents the comparison between the simulated and experimental results, highlighting the level of accuracy of the model and discussing any remaining errors.

The correct design of the model, demonstrated by an accurate representation of the

working conditions of the prototype in the analysed first gear configuration, would prove to be essential to allow its use for additional testing scenarios in future studies.

6.1 Simulation Setup

The simulation environment adopted in this work is based on the Simulink dynamic model of the Planetary Magnetic Gearbox presented in chapter 5 and shown in Figure 6.1. The model has been tailored to replicate the behaviour of the prototype in its first gear configuration. Although its architecture allows for reconfigurations to simulate the second gear scenarios, the current analysis deals exclusively on its first gear, to replicate the experimental tests previously performed in chapter 4.

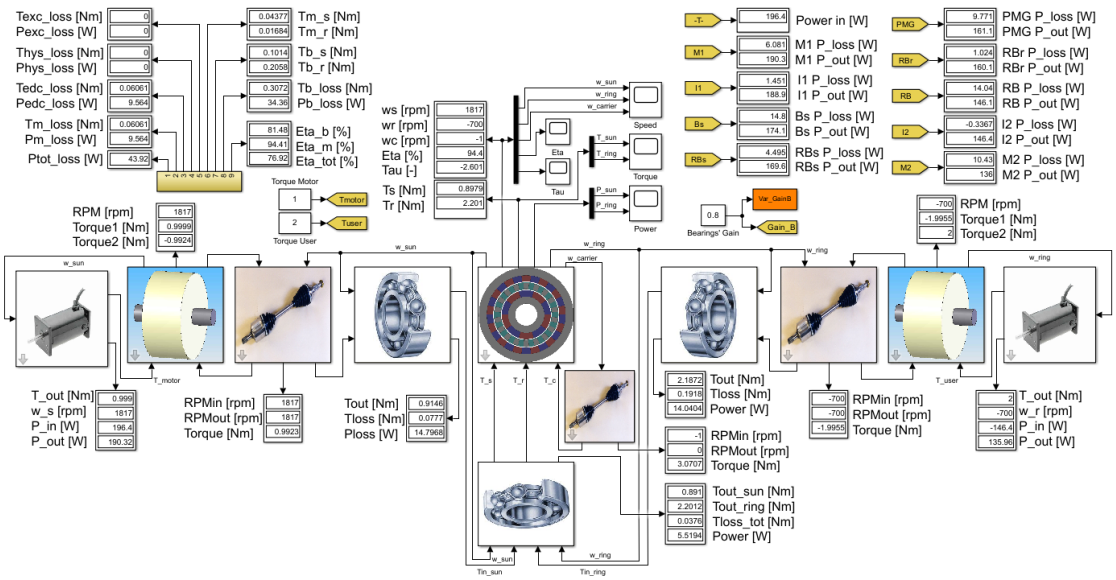

Figure 6.1: Complete architecture of the Simulink model, including main structure and control panel.

The simulation is designed to evaluate the system under steady-state conditions, to replicate the experimental methodology. Each simulation is set to a duration of 100 seconds, which is the sufficient time amount needed to reach steady state conditions for every configured scenario. Additionally, all initial state variables in the model have been set to zero to minimise its dependency on initial conditions.

Due to the very stiff dynamic equations present in the model, the choice of the suitable solver was of great importance for the correct convergence of the simulations. The more standard ode45 solver was in fact unable to run and solve the simulation environment. The choice fell on the ode23tb, a trapezoidal solver that is specifically suitable for very stiff problems. The use of this solver ensures that a numerical stability and a reliable convergence to steady state conditions is reached, which is a necessary condition for the accurate validation of the model.

While the primary focus of this work is the study of the steady state results of the simulations, for a comparative analysis with the experimental tests results, the simulation environment is also capable of capturing and analysing the transient dynamics of the system, a study that would be very hard to be replicated on the test bench. This capability could be adopted by future works to further study the PMG and test bench performances.

6.1.1 Control Strategy

The control strategy adopted in the dynamic model is quite simple, with both sun and ring motors controlled in torque mode. However, the implementation of this torque commands follows a personalised strategy designed to more accurately replicate the experimental conditions.

For what concerns the torque that is applied to the ring motor, simulating the user load, its value is directly taken from the experimental test acquisitions. In particular, the actual torque values measured by the transducers positioned on the ring shaft were used for these simulations, rather than the nominal torque commands inputted to the prototype via LabView. This ensures that the simulations depict the real loads that are experienced by the PMG prototype in the test bench. To adopt this simulation design choice, it was necessary to make sure that the ring motor would have as torque output the exact value inserted by the user at any time, and particularly at steady-state conditions, adjusting the PID controller gains accordingly.

On the other side, the torque applied to the sun motor is not directly taken from the sun shaft transducer, as seen on the ring side. Instead, it is iteratively fitted to make sure that the sun shaft, and hence the ring shaft, rotates at the same speed that was captured with the corresponding experimental test. The difference encountered between the two values of motor torques are very subtle, but the application of this control strategy ensured that the comparison between the two sets of simulated and experimental results would be simpler to visualise. This adopted control strategy on the sun motor effectively ends up being a speed control mode, through fitting of the required torque. Once again, the correct adjustment of the PID controller gains was required to ensure that the applied torque would instantly be available to the sun shaft without particular delay or steady-state errors.

To clarify the control scenario, an example case is analysed in Table 6.1.

Test Reference	**Sun Speed**	**Sun Torque**	**Ring Speed**	**Ring Torque**
Exp Tests - reference input	-	-	240 rpm	1.56 Nm
Exp Tests - measured values	624 rpm	0.7141 Nm	240 rpm	1.5155 Nm
Sim Tests - nominal input	-	0.7141 Nm	-	1.5155 Nm
Sim Tests - fitted input	624 rpm	0.7143 Nm	240 rpm	1.5155 Nm

Table 6.1: Control logic adopted for simulation tests: from experimental input to fitted simulation input values.

To simulate the test condition corresponding to a ring speed of 240 rpm, and a sun speed of 624 rpm, at a user torque of 1.56 Nm, the simulation implements the ring torque of 1.5155 Nm, that was measured in the corresponding experimental test by the ring side transducer, and a sun torque of 0.7143 Nm, fitted from an initial measured value of 0.7141 Nm by the sun side transducer, to accomodate the required speed matching.

This control approach resulted in uniquely defined scenarios, purposely adjusted for each test. As a result, the simulation environment does not longer rely on fixed test matrices, as previously presented in subsection 4.1.2, but rather on reconstructed operating points extracted from the real behaviour of the prototype, as shown in Table 6.2 and Table 6.3.

Ring Speed	**Sun Torque**	**Ring Torque**
60 rpm	0.3722 Nm	0.8121 Nm
120 rpm	0.4050 Nm	0.8219 Nm
180 rpm	0.4320 Nm	0.8314 Nm
240 rpm	0.4550 Nm	0.8414 Nm
300 rpm	0.4739 Nm	0.8477 Nm
360 rpm	0.4930 Nm	0.8600 Nm
420 rpm	0.5103 Nm	0.8707 Nm
480 rpm	0.5232 Nm	0.8717 Nm
540 rpm	0.5386 Nm	0.8800 Nm
600 rpm	0.5549 Nm	0.8911 Nm
660 rpm	0.5705 Nm	0.9019 Nm
720 rpm	0.5875 Nm	0.9179 Nm

(a) Simulation test points for reference ring torque of 0.78 Nm.

Ring Speed	**Sun Torque**	**Ring Torque**
60 rpm	0.5027 Nm	1.1509 Nm
120 rpm	0.5352 Nm	1.1606 Nm
180 rpm	0.5623 Nm	1.1704 Nm
240 rpm	0.5846 Nm	1.1782 Nm
300 rpm	0.6040 Nm	1.1860 Nm
360 rpm	0.6220 Nm	1.1952 Nm
420 rpm	0.6402 Nm	1.2083 Nm
480 rpm	0.6536 Nm	1.2105 Nm
540 rpm	0.6687 Nm	1.2181 Nm
600 rpm	0.6845 Nm	1.2283 Nm
660 rpm	0.6999 Nm	1.2384 Nm
720 rpm	0.7165 Nm	1.2535 Nm

(b) Simulation test points for reference ring torque of 1.17 Nm.

Table 6.2: Control Strategy for simulated tests (pt.1).

6.1.2 Operating Conditions and Limitations

In the engaged set of tests, the prototype was designed to operate as a speed reducer and torque multiplier, which is the configuration here adopted and studied in the corresponding set of simulated tests. In this setup, the sun shaft acts as the input, while the ring shaft as the output, rotating at reduced speed and delivering the required user torque. However, the model can be easily adapted to simulate in the opposite operating condition, as a speed multiplier and torque reducer, reversing the direction of the power

Ring Speed	**Sun Torque**	**Ring Torque**
60 rpm	0.6320 Nm	1.4873 Nm
120 rpm	0.6650 Nm	1.4983 Nm
180 rpm	0.6922 Nm	1.5080 Nm
240 rpm	0.7143 Nm	1.5155 Nm
300 rpm	0.7338 Nm	1.5232 Nm
360 rpm	0.7510 Nm	1.5307 Nm
420 rpm	0.7684 Nm	1.5415 Nm
480 rpm	0.7841 Nm	1.5500 Nm
540 rpm	0.7981 Nm	1.5547 Nm
600 rpm	0.8138 Nm	1.5645 Nm
660 rpm	0.8290 Nm	1.5742 Nm
720 rpm	0.8455 Nm	1.5887 Nm

(a) Simulation test points for reference ring torque of 1.56 Nm.

Ring Speed	**Sun Torque**	**Ring Torque**
60 rpm	0.7614 Nm	1.8233 Nm
120 rpm	0.7944 Nm	1.8344 Nm
180 rpm	0.8214 Nm	1.8437 Nm
240 rpm	0.8435 Nm	1.8510 Nm
300 rpm	0.8627 Nm	1.8586 Nm
360 rpm	0.8797 Nm	1.8654 Nm
420 rpm	0.8962 Nm	1.8739 Nm
480 rpm	0.9117 Nm	1.8818 Nm
540 rpm	0.9268 Nm	1.8894 Nm
600 rpm	0.9424 Nm	1.8989 Nm
660 rpm	0.9574 Nm	1.9080 Nm
720 rpm	0.9738 Nm	1.9223 Nm

(b) Simulation test points for reference ring torque of 1.95 Nm.

Table 6.3: Control Strategy for simulated tests (pt.2).

flow. In that case, some minor adjustments would have to be implemented in both motors, inverting the signs of the back-EMF and mechanical contribute equations, and on the bearings' equations, reducing the available torque on the ring side and increasing the required torque on the sun side. While this alternative use case scenario is not adopted in the current thesis, the simulation environment allows for supporting such analysis with appropriate modifications, if deemed useful in additional future studies.

Some limitations present in the model are the not inclusion of a thermal model in the system and the absence of a degradation model. The former is particularly important when describing the bearings losses, which are assumed to reflect the conditions measured during the experimental tests, where a thermal equilibrium was reached. That means that the bearings are, by assumption, always in thermal regime in this model. The absence of the degradation model, instead, doesn't allow to take into account long term degradation of the prototype parameters, such as variations in magnetic properties or eventual mechanical wear of the joints and bearings. While not important for the scope of this work, the modelling of these contributions could prove useful for the correct prediction of the prototype's behaviour additional scenarios.

6.1.3 Model Parameters

The main parameters adopted for the following simulation tests are summed up in tables 6.4÷6.7. These parameters are grouped by the functional block which they belong, and are completed by their value and source, that could be coming from either computation, datasheet or design choice.

Variable Name	**Value**	**Value Origin**
Set, F/b Gain [K_{set} $K_{f/b}$]	[0.5 0.5] V/Nm	Design Choice
PID Gains [K_p K_i K_d]	[80 80 1]	Design Choice
Amplifier Gain K_A	300	Design Choice
Inductance L	12.8 mH	Datasheet
Resistance R	1.86 Omh	Datasheet
Torque Gain K_c	1.19 Nm/A	Datasheet
Back-EMF Gain K_e	1.0219 Vs/rad	Datasheet
Damping c_m	0.001 Nms/rad	Assumption
Inertia J_m	0.00108 kgm^2	Datasheet

Table 6.4: Simulations Parameters for the Motor blocks.

Block Name	**Variable Name**	**Value**	**Value Origin**
Inertia	Inertia Sun J_{sun}	0.0005 kgm^2	Computation
Inertia	Inertia Ring J_{ring}	0.0214 kgm^2	Computation
Transmission	Torsional Stiffness K_t	4000 Nm/rad	Datasheet
Transmission	Torsional Damping c_t	42 Nms/rad	Datasheet

Table 6.5: Simulations Parameters for Inertia and Transmission blocks.

It is important to note that, while most of the parameters used in the simulation model are already populated in these tables, the damping coefficients associated with the magnetic losses in the PMG block are not predefined. In fact, these coefficients representing the hysteretic, eddy currents and excess damping losses have to be calibrated prior to the start of the simulation tests by a dedicated fitting procedure, to ensure that the dynamic model accurately represents the magnetic losses of the prototype. In a similar fashion, also the correction factor used in the bearings block has not been univocally determined yet in Table 6.6, because its value is directly tied to the damping coefficients fitting process, as it will be later discussed. The final determination of all these parameters is analysed in further detail in section 6.2.

Variable Name	**Value**	**Value Origin**
Sun Torque Losses T_{bs}	LookUp table	Neutral Exp. Tests
Ring Torque Losses T_{br}	LookUp table	Neutral Exp. Tests
Correction Coefficient K_{corr}	< 0.9 (tbd)	Engaged Exp. Tests

Table 6.6: Simulations Parameters for the Bearings blocks.

Variable Name	**Value**	**Value Origin**
Magnetic Poles number $[n_s\ n_r]$	[13 5]	Design Choice
Iron Poles number n_c	18	Design Choice
Inertia $[J_s\ J_c\ J_r]$	[0.00116 0.00024 0.001] kgm^2	Computation
Hysteretic Damping $[b_s\ b_c\ b_r]$	(tbd)	Fitting
Eddy Current Damping $[c_s\ c_c\ c_r]$	(tbd)	Fitting
Excess Damping $[c_s\ c_c\ c_r]$	(tbd)	Fitting

Table 6.7: Simulations Parameters for the PMG blocks.

6.2 Damping Coefficients Fitting and Correction Factor Final Evaluation

To ensure that the simulation environment accurately reflects the physical behaviour of the Planetary Magnetic Gearbox, it is first necessary to define its damping coefficients. A fitting procedure is implemented for the determination of these coefficients, based on the magnetic losses that have been observed from the experimental tests. These losses have been computed as the difference between the total losses measured from the engaged tests and the mechanical losses measured from the neutral tests, which are proportional to the correction factor introduced to remove the residual magnetic losses contribute from them. This means that the correction factor plays a major role in the calibration of the damping coefficients of the PMG, and the final evaluation of its value had to be defined to properly design the magnetic loss model.

6.2.1 Damping Coefficients Fitting Methodology

The three damping parameters belonging to the PMG block to be determined are the hysteretic losses coefficient b , the Eddy Currents losses coefficient c and the Excess losses coefficient d. These coefficients have been computed via fitting procedure that adjusts them to accurately reproduce the magnetic losses computed from the experimental tests. The fitting is performed by the use of a non-linear function that models these magnetic losses as a function of the sun shaft speed, denominated x for this task, which is:

$$P_{m_{loss}}(x) = \underbrace{\left(b + c \cdot x + \frac{d \cdot x}{\sqrt{1+|x|}}\right) \cdot x}_{\text{Sun Side}} + \underbrace{\left(-b + c \cdot \left(\frac{x}{-2.6}\right) + \frac{d \cdot \left(\frac{x}{-2.6}\right)}{\sqrt{1+\left|\frac{x}{-2.6}\right|}}\right) \cdot \left(\frac{x}{-2.6}\right)}_{\text{Ring Side}} \tag{6.1}$$

This equation is made up by two main sections: on the left side the model sourced on the sun gear are modelled, while the magnetic losses associated with the ring gear are modelled on the right side. Each contribution of magnetic torque loss computed in the main parenthesis on each side is then multiplied by the respective rotational speed. In particular, the rotational speed of the ring has not been used as an additional function variable, since it is directly correlated to the sun speed by the gear ratio factor of -2.6, specific to the first gear conditions. The magnetic losses associated with the carrier gear are not included in this fitting procedure, as it is kept fixed during the simulations, just as seen for the experimental tests, and contributes to no power losses due to its null speed.

The hysteretic torque losses are directly not dependent on the speed and have been modelled by the simple adoption of the coefficient b. The eddy current torque losses are, instead, proportional to the rotational speed of the gear, and are modelled with the $c \cdot x$ factor. Finally, the excess torque losses are dependent on the root square of the rotational speed of the gear, following a factor of $d \cdot \sqrt{x}$. However, to ensure numerical stability in Matlab, these excess torque losses modelling was reshaped as $d \cdot x/\sqrt{1+|x|}$, avoiding the non-differentiable point at $x = 0$ that can cause instability in the non-linear fitting algorithm.

Additionally, to simplify the model and to reduce the number of fitting equations and parameters to be computed, the same damping coefficients were applied to all three gears for each loss contribution. In formulas:

$$\begin{cases} b = b_s = b_c = b_r \\ c = c_s = c_c = c_r \\ d = d_s = d_c = d_r \end{cases} \tag{6.2}$$

This assumption avoids over-fitting these terms, which is not necessary or useful in this test case scenario as the experimental tests measurements didn't allow to measure for losses specifically attributed to one gear rather than the other.

The parameters on Equation 6.1 have been fitted using Matlab's non-linear curve fitting toolbox, which adopts a least squares approach to minimise the error between the reference data and the simulated results. The correct results of the fitting operation was evaluated using the coefficients of determination R^2, the mean square error $RMSE$, as well as visual overlay of the curves obtained.

6.2.2 Correction Coefficient Influence

The first fitting attempt was performed using a correction factor K_{corr} of 0.90 applied to the mechanical losses measured in the neutral configuration. As previously discussed

in subsection 4.2.4 and visualised in subsection 4.4.3, this 0.90 correction factor is the highest value that guarantees that the system will behave correctly from a physical standpoint, without any efficiency parameter having any value above the 100% mark. The schematised formula used to compute the magnetic losses as a function of the correction factor and on the values of power losses measured during the experimental tests on the prototype, both in engaged and neutral configuration, is the following:

$$P_{m_{loss}} = P_{tot_{loss}} - P_{b_{loss}} = P_{eng_{loss}} - K_{corr} * P_{neu_{loss}} \tag{6.3}$$

The result of this computation is a curve on the power - speed diagram, where for each value of speed delta between the sun and ring gear during operating conditions, a value of magnetic power loss has been computed. This resulting experimental curve has been used as the reference for the simulated losses, for the best fitting operation of the damping coefficients, as shown in Figure 6.2.

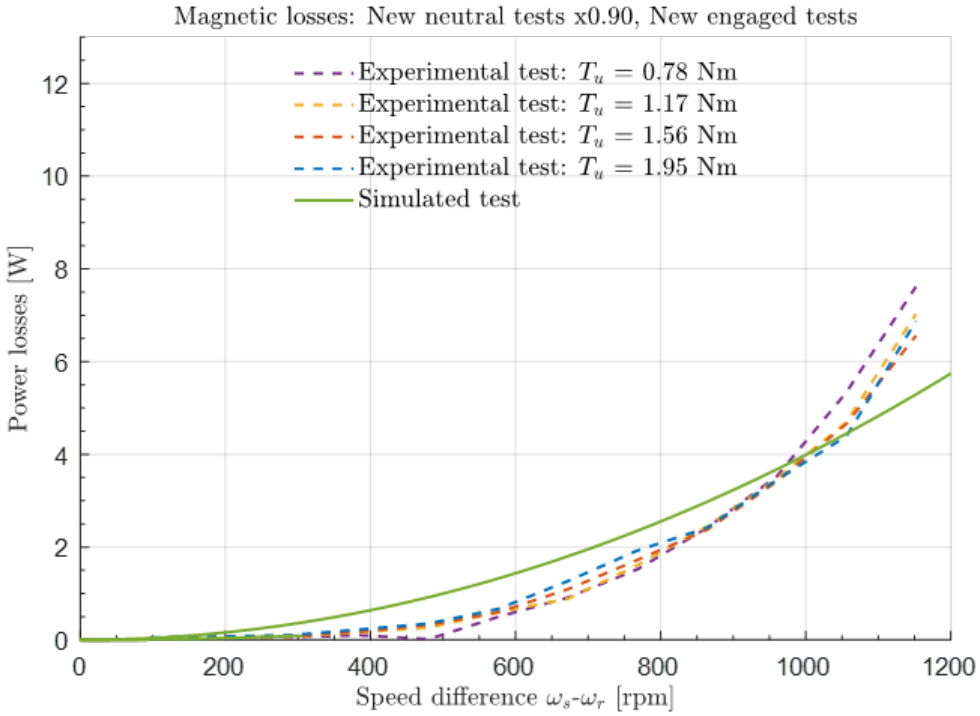

Figure 6.2: Magnetic Losses fitting results with $K_{corr} = 0.90$.

The result obtained through this first fitting scenario using Equation 6.1 is not very accurate, as the general trend of the simulated curve does not replicate that of the experimental tests. In particular, an overfitting is visible for low to medium speeds delta, while there is an underfitting for higher speeds.

Performing additional tests using other values of correction factor lower than 0.90, it was noticed that a general trend was followed, with the results of the fitting procedures being more and more accurate the lower the correction factor adopted was. This means

that, for what concerns the experimental tests performed in neutral conditions, the residual magnetic losses might have been underestimated, and that perhaps their contribution is larger than anticipated. The result of an adoption of a lower correction factor leads to an increase of the magnetic power losses obtained through Equation 6.3, leading to fitting curves that better follow the overall trend of the experimental curves.

In particular, the results of three main fitting trials are shown next, related to a fitting coefficient of 0.85, 0.80 and 0.75.

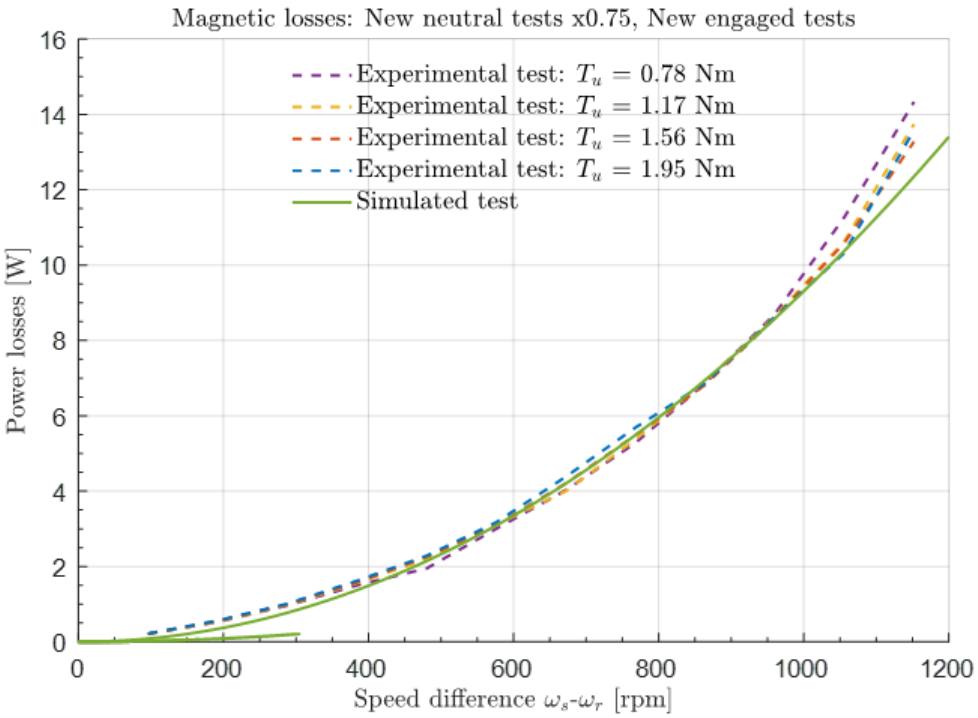

Figure 6.3: Magnetic Losses fitting results with $K_{corr} = 0.75$.

Confirming the statement made earlier, the curve obtained with the correction factor of 0.75, the lowest one adopted, is the best one for what concerns the overall capability of the simulation results to follow the experimental curves (Figure 6.3). However, the adoption of such a low correction factor might also lead to the risk of an overestimation of the magnetic loss contribution in the neutral configuration, potentially compromising the fitting effort and the physical realism of the model.

On the other hand, the correction factor of 0.85 leads to simulation results that still quite differ from the experimental ones, potentially being attributed to an underestimation of the magnetic loss, contrary to what discussed for the 0.75 value (Figure 6.4).

For these reasons, the best overall result that is both physically complaint and that represent a compromise for what concerns the overall losses measured in the prototype, is obtained with the adoption of a 0.80 correction factor, as previously anticipated in subsection 4.2.4 (Figure 6.5). The adoption of this value provides the correct balance between a good enough fitting accuracy while being conservative with the estimation of

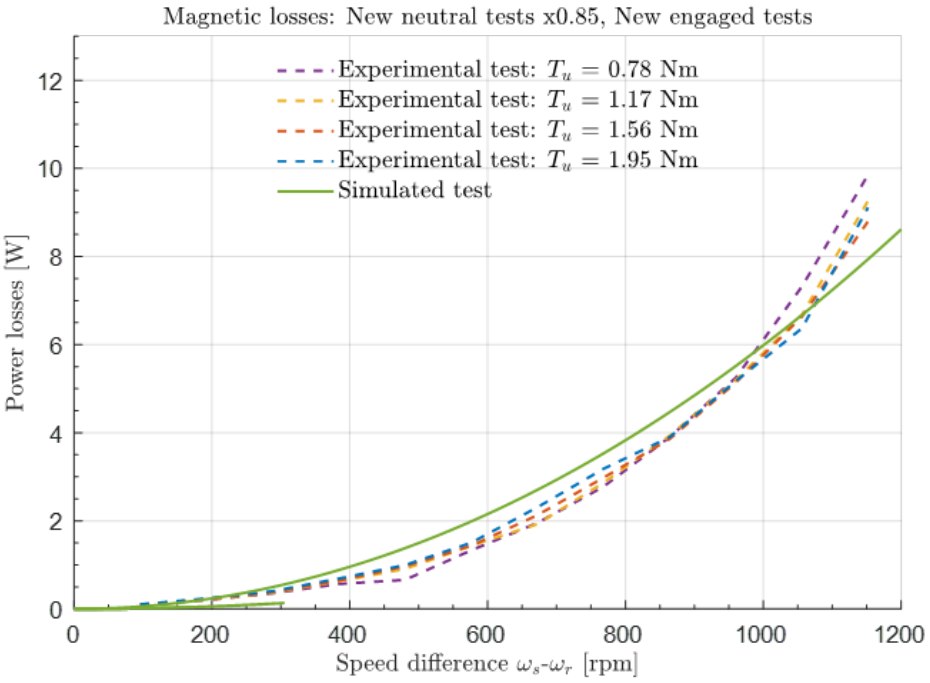

Figure 6.4: Magnetic Losses fitting results with $K_{corr} = 0.85$.

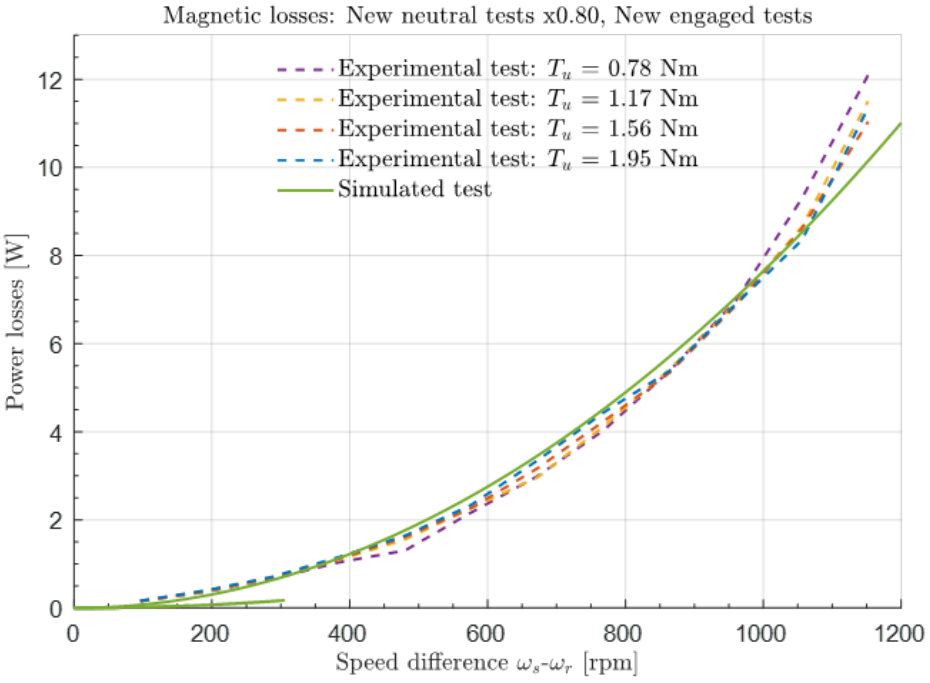

Figure 6.5: Magnetic Losses fitting results with $K_{corr} = 0.80$.

the residual magnetic losses.

For what concerns the fitting results of the damping coefficients, their values are recollected in Table 6.9, along with the coefficients of determination and the root mean square error of each fitting trial.

Parameter	$K_{corr} = 0.90$	$K_{corr} = 0.85$	$K_{corr} = 0.80$ **(selected)**	$K_{corr} = 0.75$
Hysteretic Coeff. b $[Nm]$	0	0	0	$5.70 \cdot 10^{-4}$
Eddy Current Coeff. c $[Nms/rad]$	$1.04 \cdot 10^{-4}$	$1.63 \cdot 10^{-4}$	$2.22 \cdot 10^{-4}$	$2.77 \cdot 10^{-4}$
Excess Coeff. d $[Nm(s/rad)^{0.5}]$	0	0	0	0
Coeff. of Determination R^2	0.9230	0.9739	0.9910	0.9960
Root Mean Square Error $RMSE$	0.6243	0.4747	0.3449	0.2757

Table 6.8: Fitting results. The damping values shown on the 0.80 correction factor column will be adopted in the Simulation model.

Parameter	$K_{corr} = 0.85$	$K_{corr} = 0.80$ **(selected)**	$K_{corr} = 0.75$
Hysteretic Coeff. b $[Nm]$	0	0	$5.70 \cdot 10^{-4}$
Eddy Current Coeff. c $[Nms/rad]$	$1.63 \cdot 10^{-4}$	$2.22 \cdot 10^{-4}$	$2.77 \cdot 10^{-4}$
Excess Coeff. d $[Nm(s/rad)^{0.5}]$	0	0	0
Coeff. of Determination R^2	0.9739	0.9910	0.9960
Root Mean Square Error $RMSE$	0.4747	0.3449	0.2757

Table 6.9: Fitting results. The damping values shown on the 0.80 correction factor column will be adopted in the Simulation model.

It is immediately noticeable that the excess damping coefficient is always negligible during the fitting operations, while the hysteretic damping coefficient only comes into play for the fitting curve related to a correction factor of 0.75. On the other hand, the Eddy current coefficient is always present in any simulation, which is a result that bears physical relevance given it is usually the most important contribution to the damping losses. For what concerns the Coefficient of determination, it is a measure of the proportion of variance in the dependent variable, the experimental data, that is predicted by the simulated model. Its maximum value is 1, and a value higher than 0.99 is usually

considered a good fitting result. This threshold is met by the fitting procedures operated with a K_{corr} of 0.80 and 0.75. Finally, the Root Mean Square Error measures the average difference between the values obtained by the fitting model and the actual experimental ones. The lower this parameter, the better the fitting procedure is successful, and the usual threshold adopted to verify the correct estimation of the parameters is lower than 0.4, which is again fully respected by the last two fitting results.

While this fitting procedure provided good results, it is important to note that the correction coefficient adopted is just an estimated value and it has not been experimentally validated. The validation of this coefficient is an important task that could be studied in future works, allowing for the computation of the true values of the residual magnetic losses in neutral configuration. This would provide a more precise calibration of the damping coefficients used in the simulation model and would improve the reliability and accuracy of the magnetic loss estimations.

6.3 Time-Domain Simulation Results

While the main objective of this work is the validation of the dynamic model of the Planetary Magnetic Gearbox by comparing the steady-state results of its simulations with the experimental data acquired on the test bench studied, it is also important to analyse the capability of the model to reproduce the dynamic behaviour of the prototype in the time domain. This provides a better understanding of the working principles of the Simulink model and its transient response.

A representative simulation scenario with predefined torque ramp signals on both the sun and ring shaft motors is analysed. In particular, the sun shaft motor receives an input torque ramp from $0Nm$ to $1Nm$ over the first second, resulting in a $1Nm/s$ trend, followed by a constant torque of $1Nm$ up to the end of the simulation time. The ring shaft motor is instead provided with an input resisting torque ramp from $0Nm$ to $2.3Nm$, resulting in a $2.3Nm/s$ trend, and then followed once again by a fixed constant torque at $2.3Nm$. The total simulation time has been set at 20 seconds, enough for the system to reach the steady state conditions. These torque signals are summed up in Figure 6.6.

The main focus of the analysis is the evolution in time of the three primary dynamic quantities related to the PMG block, which are the sun and ring speed, torque and power. Their evolution is studied both across the full simulation as well as with a focus on the first second of the simulation, to highlight their transient behaviour.

6.3.1 Time-Domain Results: Speed

The first quantities to analyse are the sun and ring shafts torques, which are the functional inputs of the PMG block. These torques should ideally reflect the exact torque inputs provided to the two motors present on the simulation model, which are modelled using a PID controller set up to provide the exact torque inputs required by the user. The results of the simulations are shown in Figure 6.7.

As expected, the torque signals present a transient behaviour in the first second of the simulation to then stabilise at their respective target values, which slightly differ in magnitude from the input torques due to the mechanical losses present on both sides

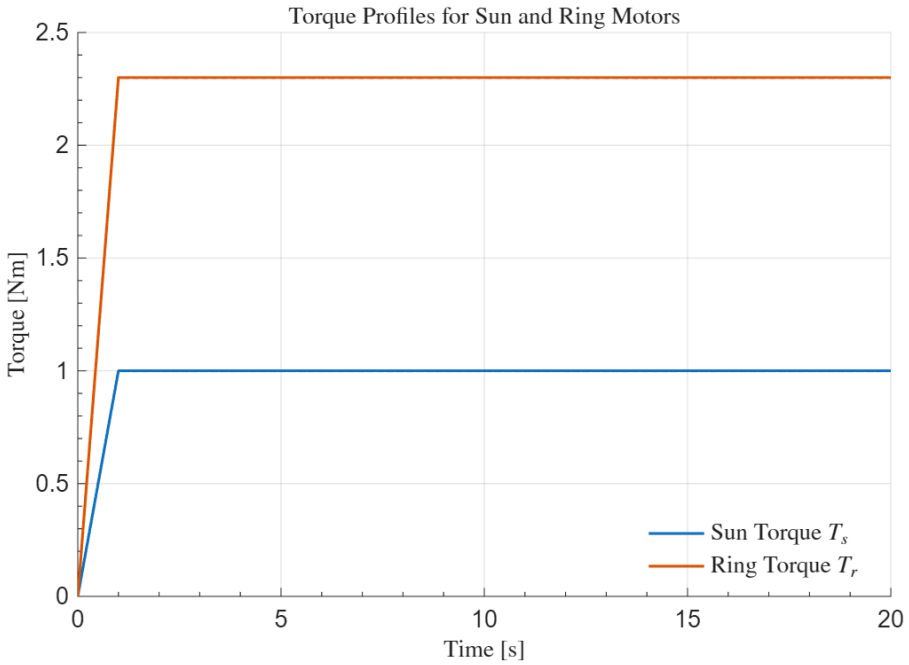

Figure 6.6: Sun motor and Ring motor Input Torque signals.

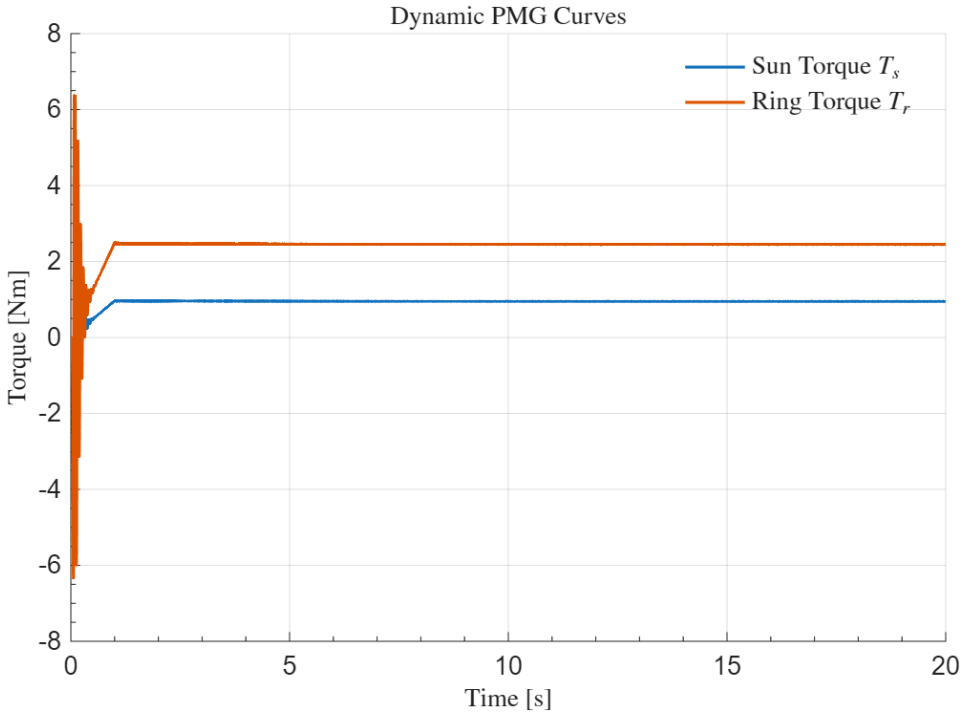

Figure 6.7: Gears Torque response over the full simulation window.

of the PGM block. The most interesting section to analyse is however the first second window, as shown in Figure 6.8, where the transient response is highlighted.

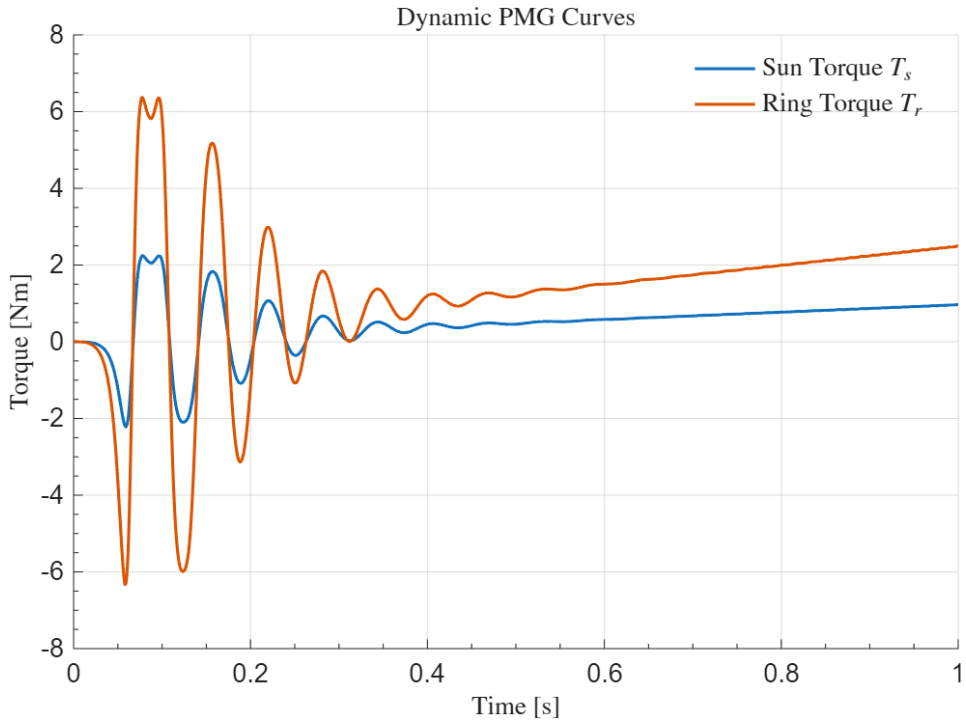

Figure 6.8: Gears Torque response during the transient phase.

In this close up view, the dynamic response of the two torque signals is more clearly visible. Both curves start from $0Nm$ and experience a quick overshoot and sharp oscillations around the null torque value due to the gears not being engaged at first, with the ring torque being much larger in magnitude compared to the sun torque due to the higher stiffness of the ring gear as well as the higher torque input. These oscillations quickly decay due to magnetic damping losses, and around the $0.3s$ to $0.4s$ time window the two gears start to feel the reciprocal interaction, leading to the complete engagement that happens in the $0.4s$ and $0.6s$ window. Once the gears are completely engaged, the torque signals simply overlay the input torques sent to the motors.

These results show the capability of the magnetic gears to transition from a generic disengaged position to a fully engaged position in a short period of time, highlighting the reliability of the system in this regard.

6.3.2 Time-Domain Results: Torque

The second quantities to analyse are the gears rotational speeds, which correspond to the functional outputs of the PMG block together with the rotational acceleration and position of the gears. The resulting speed signals are shown in Figure 6.9.

The major transient behaviour happens once again during the first second of simulation, as expected. However, unlike what has been observed for the torque curves,

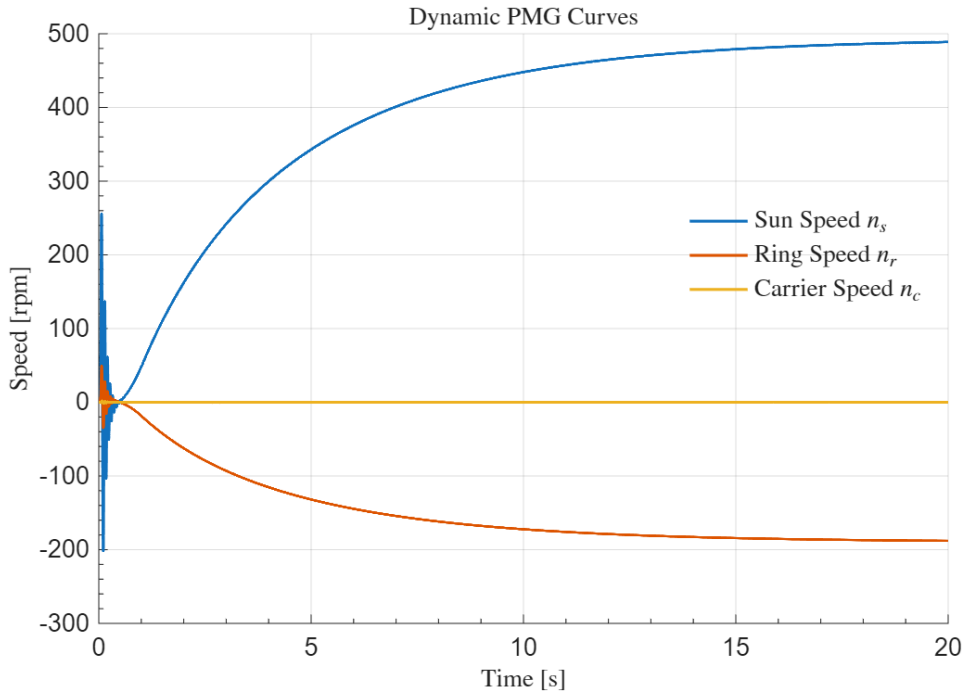

Figure 6.9: Gears Speed response over the full simulation window.

the rotational speeds don't reach the steady state conditions as soon as the first second transient is completed but tend to accelerate for the whole simulation window. This is once again supported by theory, as the speed signals are commanded by a first order response, slower compared to the zero order response of the torque signals. The equilibrium is reached only by the end of the simulation window, where the sun speed stabilised at 485rpm and the ring speed at -187, proportional to each other by the gear ratio $\tau = -2.6$. For what concerns the carrier speed, it is constant and equal to 0rpm, showing the correct results of the designed fixed condition of this gear. A more specific overview on the initial transient window is shown in Figure 6.10.

At the start of the simulation, all speed signals start from resting conditions. A quick acceleration on both the sun and ring gears is the result of the torque signal overshoot previously observed. Once again, these speed oscillations are dampened in time and, when the gears reach the engaged configuration around $t = 0.5s$, they start follow a parabolic trend in response to the respective torque ramps.

6.3.3 Time-Domain Results: Power

The final quantities to analyse are the gears transmitted powers. These parameters are computed by the product of each gear torque and rotational speed, and their correct transmission is the main goal of any mechanical machine. The power curves obtained from this simulation are shown in Figure 6.11.

For what concerns the overall trend of these curves, being them the result of the product between the previously analysed figures, they follow almost exactly the speed

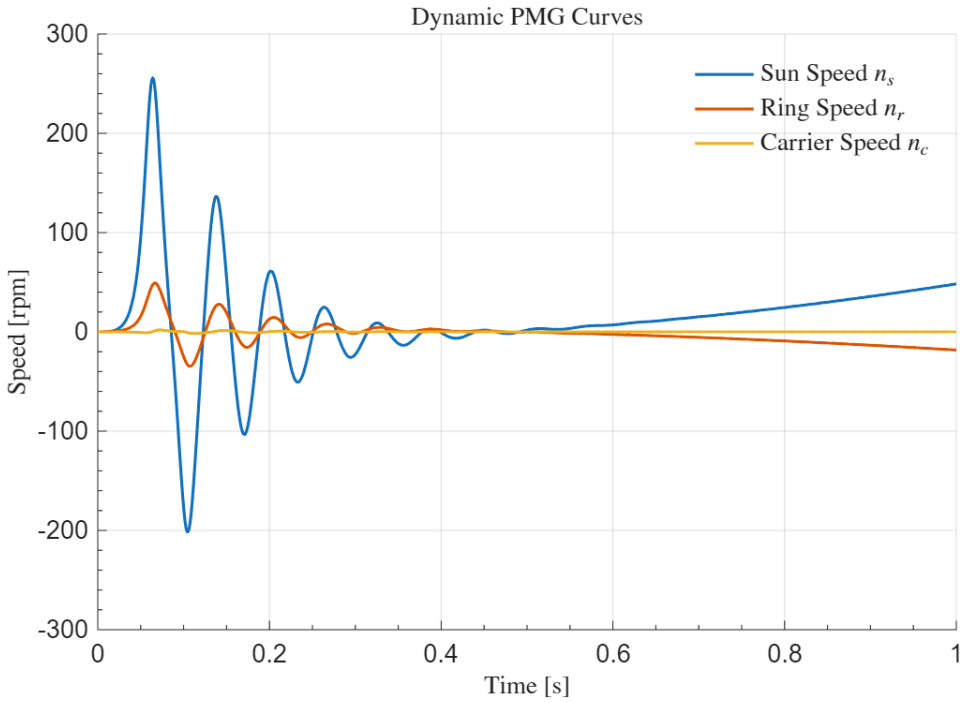

Figure 6.10: Gears Speed response during the transient phase.

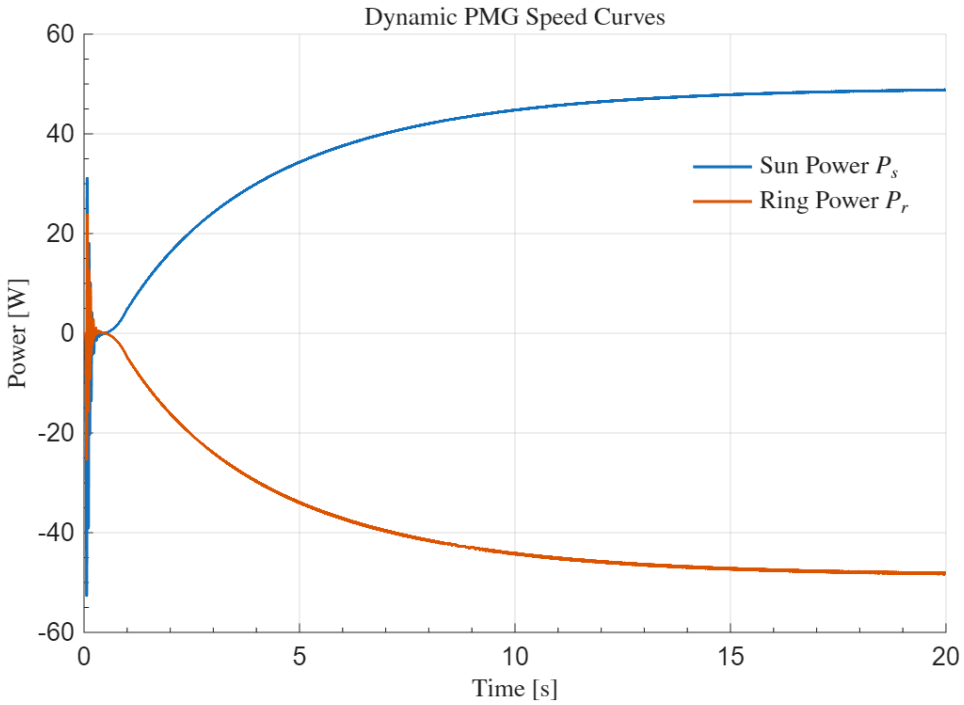

Figure 6.11: Gears Power response over the full simulation window.

signals. At steady state conditions, the sun provides $48.4W$ to the system, while the ring is able to transmit $47.7W$, meaning that $0.7W$ have been dispersed by damping actions. The different roles of these gears in the power transmission analysis are highlighted by their responses having opposite signs. A close up to the first second of simulation is shown in Figure 6.12.

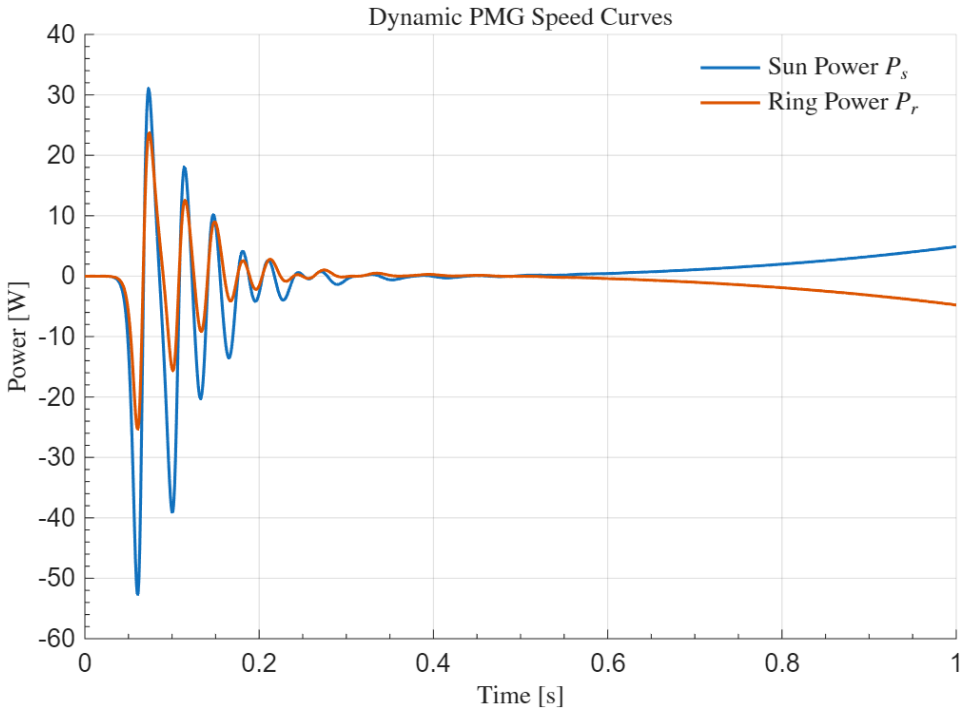

Figure 6.12: Gears Power response during the transient phase.

Once again, the response follows very similarly what seen in the previous figures, with sharp oscillations that dampen over time during the disengaged configuration of the gears, which turns into a smooth parabolic trend once the gears are in engaged position.

Overall, the results obtained with this reference simulation test indicate that the dynamic properties of the Simulink model follow the theoretical and expected trends, validating the physical consistency of the simulation environment.

6.4 Steady-State Simulation Results

Having provided a quick overview of the transient behaviour of the dynamic model for a reference simulation, the focus shifts to the evaluation of the main parameters' values once they have reached steady-state conditions, in order to build the database to be compared with the experimental test results.

Each simulation was performed following the same procedure seen in the last section, with torque inputs following a ramp up to a specific value for the first second of simulation, followed by a constant torque up to the end of the simulation window. The simulation

time adopted was set to be $100s$, to ensure that any transient phenomena would be completely disappear and that only the steady state component would be left.

The specific values adopted for the two torque inputs are the ones previously summarised in Table 6.2 and Table 6.3, built to follow the specific grid of speeds adopted during the experimental tests. This alignment allows for a better and more consistent comparison between the simulated and experimental results. The main parameters that have been studied are the torque and power losses, the magnetic, mechanical and total efficiencies trends, and the power transmission chain.

6.4.1 Torque and Power Losses

The evaluation of torque and power losses under multiple load scenarios at steady-state conditions allows to punctually evaluate the internal dissipations of the simulation model. While multiple losses sources are modelled in this model, the main ones are related to the mechanical friction modelled in the bearings blocks and the magnetic damping contribution of the PMG block.

For what concerns the torque losses contributes, they are presented in Figure 6.13 as a function of the speed difference between the sun and ring shafts.

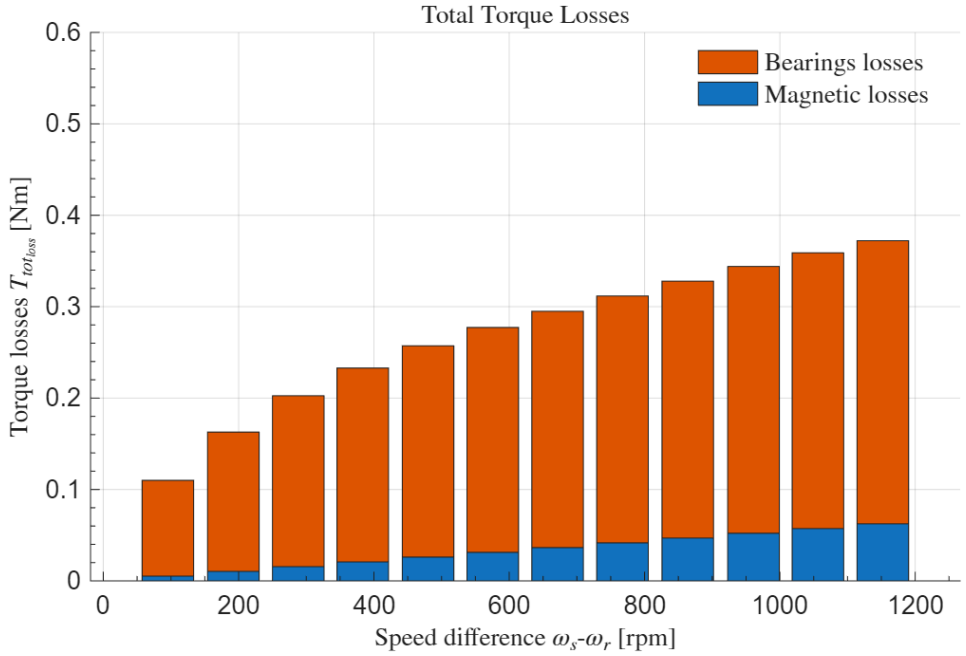

Figure 6.13: Torque Losses Breakdown.

Based on the updated correction coefficient and on the newly fitted damping coefficients adopted by the model, it is clearly visible how the vast majority of torque losses are attributable to the mechanical friction of the bearings, which consistently account for more than 85% of the total losses. Additionally, both of these loss contributions are dependent on the speed, with the bearings one showing an inverse parabolic trend while

the magnetic contribution has a linear trend, which is consistent with the physics of the problem.

To better comprehend the impact of these losses, the overall power losses are shown in Figure 6.14, computed as the product of the torque and angular velocity of the shaft they are referred to.

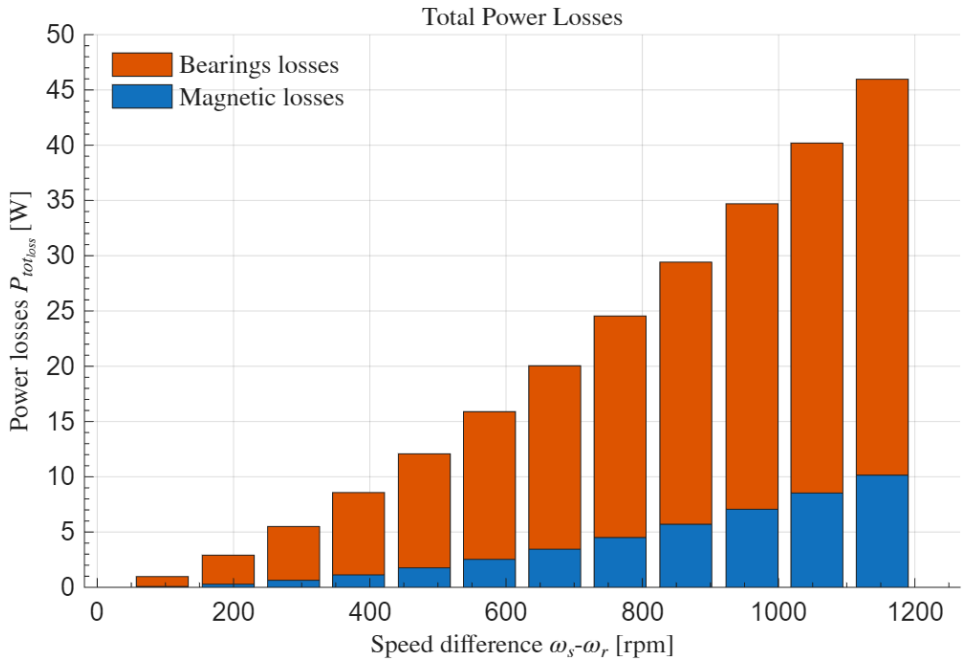

Figure 6.14: Power Losses Breakdown.

These losses show a quadratic growth, due to the way they have been computed, and consistent to the system's physics. To provide some reference values for comparison purposes, at the highest speed difference equal to $1152rpm$ combined with the highest torque load adopted equal to $1.95Nm$, the power required by the user is approximately $147W$, while the total power losses amount to $46W$, of which $36W$ are due to bearings friction and $10W$are due to damping phenomena in the PMG. This means that the input power the sun motor has to provide to the system, not accounting for the losses inside the motor itself, is $193W$, leading to a total efficiency of 76%.

While the bearings losses account for the majority of the power losses, this time around the magnetic losses grow with a higher rate, reaching contributions as high as 22%, compared to the maximum contribution of 15% registered on the torque losses graph.

Overall, these results are in line with the simulations expectations, providing additional insights into the validation of the dynamic model.

6.4.2 Efficiency Trends

The efficiencies related to the PMG system are evaluated by adopting the same formulas adopted for the efficiency computation of the experimental test bench, which are reported

below for better clarity, respectively used to compute the total, magnetic and bearings efficiency.

$$\eta_{tot} = \frac{T_r\,\omega_r}{T_s\,\omega_s}\,(\cdot 100\%) \tag{6.4}$$

$$\eta_m = \frac{(T_r + T_{br})\,\omega_r}{(T_s - T_{bs})\,\omega_s}\,(\cdot 100\%) \tag{6.5}$$

$$\eta_b = \frac{\eta_{tot}}{\eta_m}\,(\cdot 100\%) \tag{6.6}$$

where:

- T_r is the ring input torque;
- T_s is the sun input torque;
- T_{br} is the ring bearings torque loss contribution;
- T_{bs} is the sun bearings torque loss contribution;

As previously seen for the loss contributions, the points making up the efficiency curves have been evaluated once each simulation has reached steady conditions. These values were evaluated across four different load scenarios, corresponding to the reference torques of $0.78Nm$, $1.17Nm$, $1.56Nm$and $1.95Nm$, as seen for the experimental tests, following the grids designed for the simulations reported in Table 6.2 and Table 6.3. The results are once again presented as a function of the difference between the sun and ring shafts.

The results obtained for what concerns the total efficiency are shown in Figure 6.15.

The curves related to the total efficiency highlight a strong dependency on both the applied user load and on the speed. For what concerns the load dependency, the results show that, provided the system rotates at the same rotational speed across different load scenarios, an increase in the required load applied to the ring shaft leads to an increase of the total efficiency. A similar trend is observed for what concerns the speed dependency, with the total efficiency showing a peak at lower speeds and a gradual parabolic decrease with a speed increase, bearing minimum results at the highest speed configuration.

The second efficiency contribution is the magnetic efficiency, which results are shown in Figure 6.16.

This efficiency evaluates the performance of the PMG block by excluding from the computation the mechanical losses typical of the bearings. The results demonstrate consistently high values across all load scenarios and at every speed analysed, with the lowest contribution amounting to approximately 88%, and every other working point higher than 90%. A dependency on the rotational speeds of the gears and on the load setup is still visible, however in a lower magnitude compared to the total efficiencies. The dependence to the speed follows a linearly decreasing trend, while, once again, an increase in applied load at the same speed configuration leads to higher values of efficiency.

The last efficiency contribution is the Bearings or Mechanical efficiency. The curves related to this parameter are summed up in Figure 6.17.

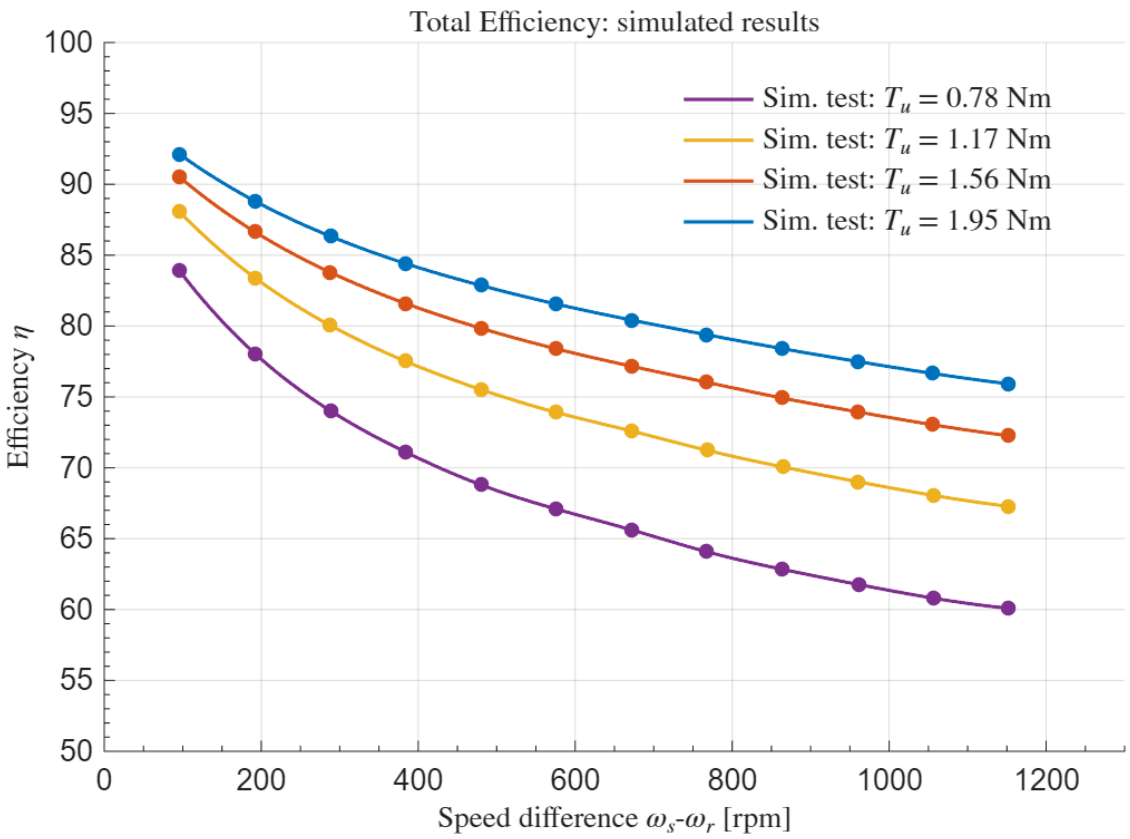

Figure 6.15: Total Efficiency Simulated Results.

Provided that these curves are simply obtained from the division between the total and magnetic efficiencies, and given the general linear trend of the magnetic contribution, the bearings efficiency curves highly resemble the total efficiency curves with just a slight decrease in their speed dependency. Focusing on their comparison with the magnetic counterparts, they show a much lower efficiency rate across the board, in line with the losses previously analysed.

6.4.3 Power Transmission Analysis

To complete the analysis of losses and performances of the simulation environment, the energy flow through each subsystem is studied and reported into a Sankey diagram, which is an effective representation of the internal power distribution and dissipation of the model.

To complement the analysis of losses and efficiency, this subsection focuses on the internal distribution of power within the PMG system under steady-state conditions. The objective is to quantify the energy flow through each subsystem and identify the primary sources of dissipation. This is achieved through a Sankey diagram representation, which visualises the power balance across the mechanical and magnetic components of the drivetrain.

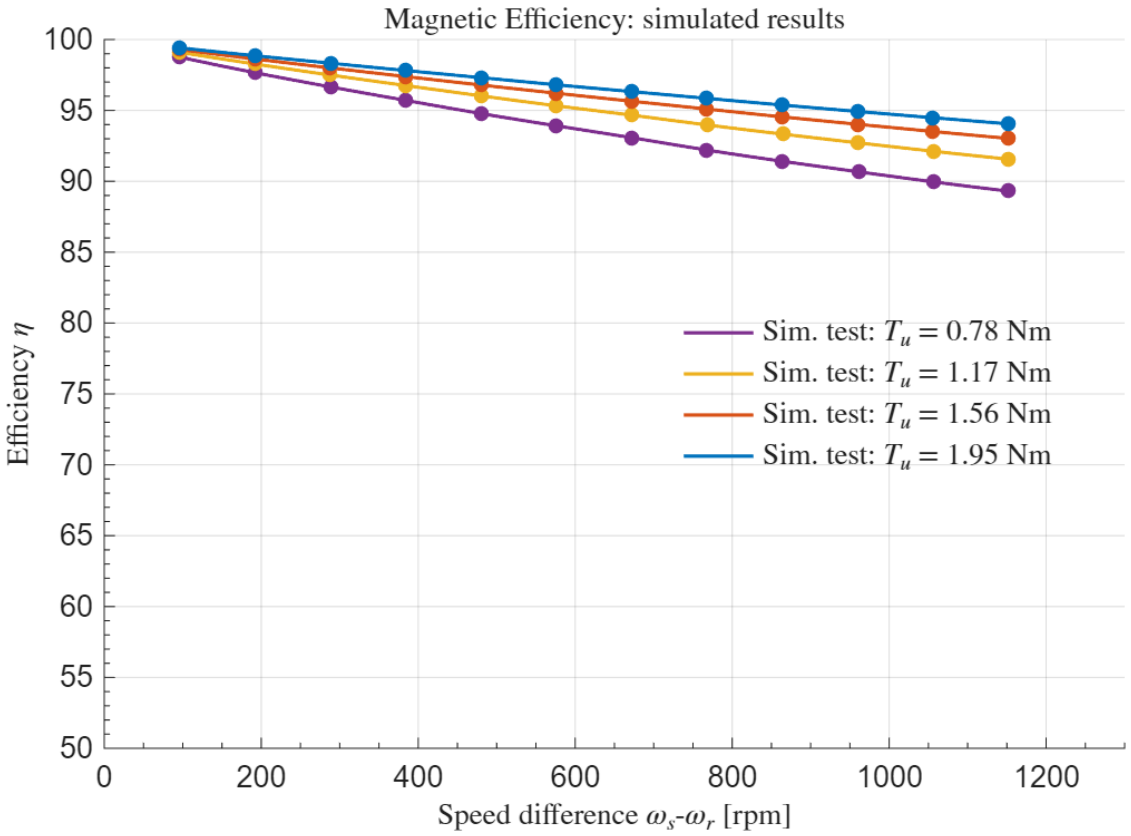

Figure 6.16: Magnetic Efficiency Simulated Results.

The analysis is based on a representative simulation corresponding to the highest available speed ($n_s = 1872\ rpm$, $n_r = 720\ rpm$) and highest applicable load ($T_s = 0.9738\ Nm$, $T_r = 1.9223\ Nm$) combination taken from the simulation grids previously adopted. This reference simulation allows for higher powers to be transmitted through the system and for a better visualisation of the distribution and losses in the system. Once again, the results are portrayed when the system has reached its steady state condition, and are visualised in Figure 6.18.

The power flow goes from the input sun shaft motor $M1$, passing through the sun side bearings, the PMG block and the ring side bearings, before reaching the output ring shaft motor $M2$. The input available power, corresponding to the electric power that puts the input motor into motion, is equal to $198.7W$. The first dissipation accounted for is due to the input motor itself, showing a $7.83W$ power loss. This means that the actual power available to the system ends up being $190.87W$. This value is set by design and comes directly from the simulation inputs provided to the system. In fact, the power set to the sun shaft simply comes from the product of the requested speed and torque combination, which is:

$$P_{in} = T_s \cdot \omega_s = 0.9738 \cdot 1872 \frac{2\pi}{60} = 190.89W \tag{6.7}$$

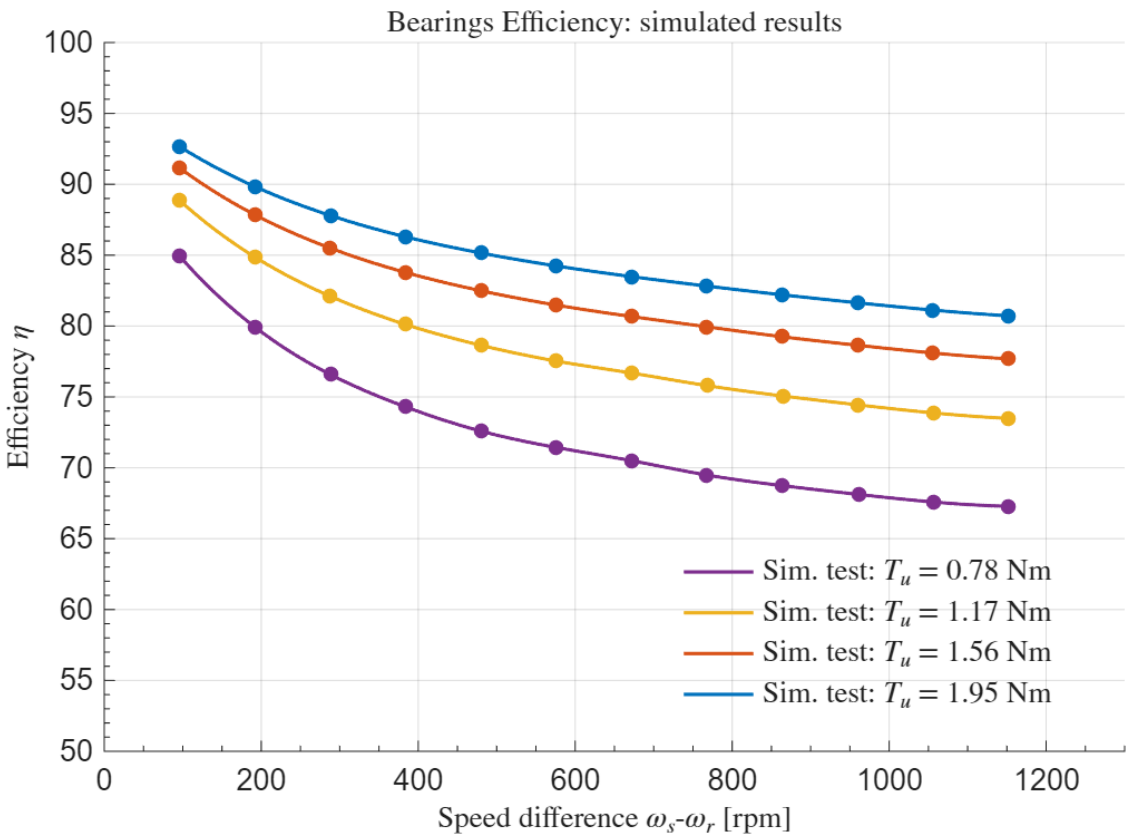

Figure 6.17: Bearings Efficiency Simulated Results.

The sun shaft motor, as well as the ring shaft motor as later demonstrated, is designed to provide the power required by design, and the actual electric power that it requires to supply said power requirements is higher to take into account its internal losses. The power provided to the system is then diminished by the friction losses encountered in the sun side bearings, which account for a loss of $20.25W$, before entering the PMG block. Here, the combined power loss of the gears amounts to $10.13W$. Then the transmitted power flows into the ring side bearings block where another power loss of $15.56W$ is registered. Finally, a total power of $144.93W$ enters the ring side motor, which acts as the load of the system. This value is the second power requirement set by design, being it the required power by the user load, computed as follows:

$$P_{out} = T_r \cdot \omega_r = 1.9223 \cdot 720 \frac{2\pi}{60} = 144.93W \tag{6.8}$$

Then once again the losses of the motor itself are taken into account, and they amount to $10.35W$. The final useful power, that is circulated back to the electric system, ends up being $134.58W$. These results show that while the magneto-mechanical system has a total efficiency of:

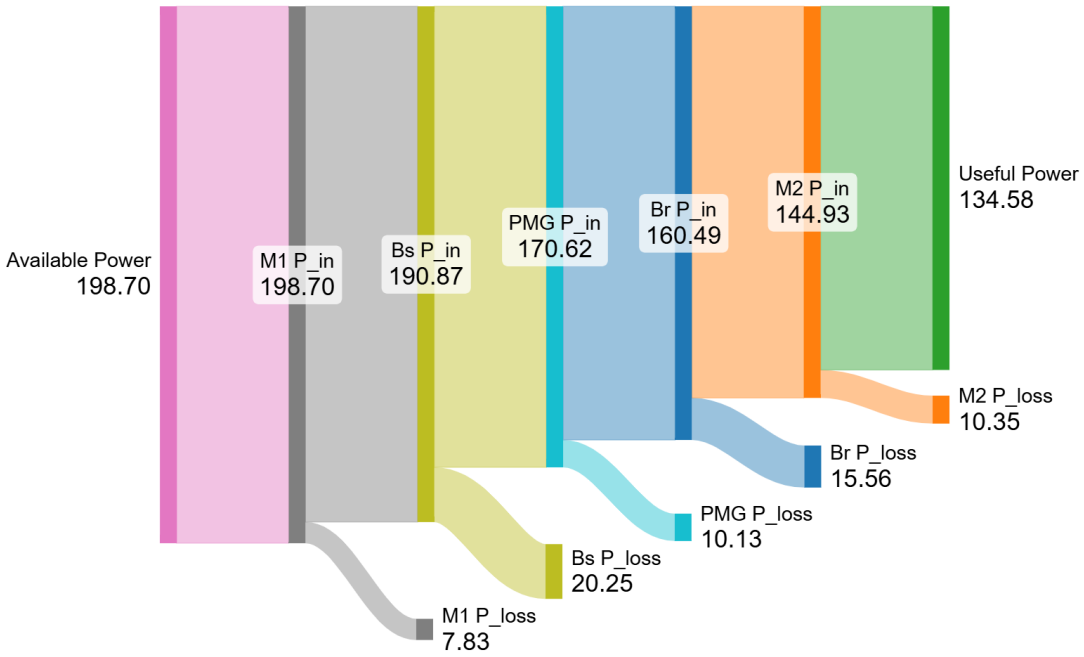

Figure 6.18: Power Transmission Flow: Sankey Diagram.

$$\eta_{tot} = \frac{P_{out}}{P_{in}} = \frac{144.93}{190.87} = 75.93\% \tag{6.9}$$

the electric system that takes into consideration the two motors has a total efficiency of:

$$\eta_{el} = \frac{Useful\ Power}{Available\ Power} = \frac{134.58}{198.7} = 67.73\% \tag{6.10}$$

The total power losses measured in the system account to $64.12W$, that split into percentages across all the contributing blocks leads to:

- Sun shaft motor: 12.21% of total losses.
- Sun shaft bearings: 31.58% of total losses.
- PMG block: 15.80% of total losses.
- Ring shaft bearings: 24.27% of total losses.
- Ring shaft motor: 16.16% of total losses.

It can be highlighted how the electro-magnetic components bear low values of power losses contributions, while the mechanical bearings blocks account for the majority of the losses.

The division of losses inside the bearings blocks can be further highlighted in Figure 6.19, where the contributions of the relative bearing is split from the other bearings contributions.

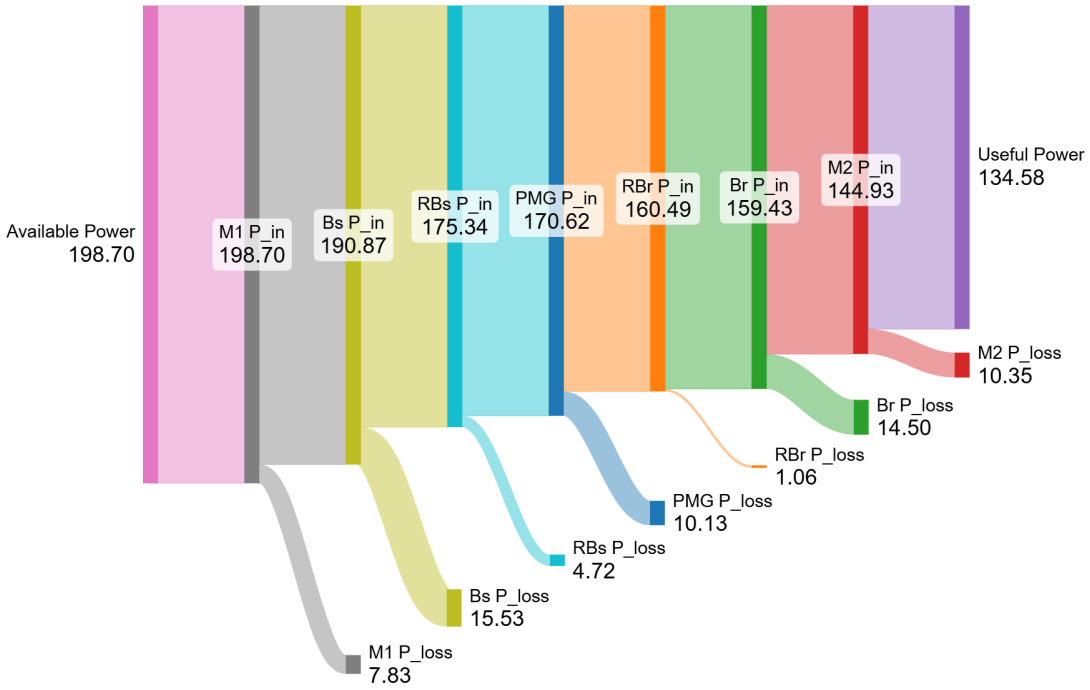

Figure 6.19: Power Transmission Flow: Sankey Diagram with relative bearings contribution.

The relative bearing accounts for $4.72W$ of losses on the sun shaft, while only $1.06W$ for what concerns the ring shaft. Summing these contributions and comparing them to the other bearings losses, the loss percentages are the following:

- Sun shaft bearings: 43.37% of total bearings losses.
- Relative Bearings: 16.14% of total bearings losses.
- Ring shaft bearings: 40.49% of total bearings losses.

The Sankey diagram results confirm that the mechanical losses associated with the bearings assembly represent the highest contributor to the overall losses inside the system. This is consistent with prior experimental analysis performed on the prototype, highlighting how a possible further optimisation of the bearings could improve the efficiency of the system.

6.5 Comparison with Experimental Tests

The full validation of the simulation model requires, other than theoretical consistency with the problem, of a detailed comparison of the results obtained with the experimental tests performed on the test bench, which results have been previously detailed in chapter 4. This comparison is necessary to assess the accuracy of the model under real operating conditions scenarios, as well as to verify the correct application of mechanical and magnetic losses mechanisms inside of it.

Once again, the values used for the comparison are taken from the simulations once the system has reached its steady state conditions, when the transient component is negligible. The useful-required torque combinations are the ones detailed in Table 6.2 and Table 6.3, that were purposely built to guarantee the correct alignment of the simulation results with the experimental ones.

The main expected result is the consistency across both sets of tests, both for what concerns the losses and the performances of the system, and especially at higher load scenarios configurations, where the influence of signal noise that could have been measured in the experimental tests is reduced.

6.5.1 Power Losses Comparison

The first set of parameters to fully compare between the experimental and simulated tests results is related to the power losses inside the system. For what concerns the power losses inside of the bearings' blocks, the comparison is shown in Figure 6.20.

The mechanical power losses attributed to the bearings measured on the simulation model are perfectly aligned with those registered via experimental testing on the prototype. This convergence is totally expected, as the mechanical losses inside the model have been implemented by the adoption of LookUp Tables derived directly from the neutral tests described in section 4.3, and by the adoption of the correction factor finalised in section 6.2. While trivial, this comparison is necessary to guarantee that the simulation environment perfectly reproduces the required mechanical losses, and to better understand the results provided by the other losses contributions.

In particular, the comparison between the total power losses obtained through the two sets of tests is reported in Figure 6.21, and are compared to the mechanical bearings losses just analysed.

In all four load scenarios configurations, the simulation model displays very clear agreement with the experimental data. The total power losses predicted by the model follow almost perfectly the experimental trends across the entire speed range under analysis. Additionally, unlike what has been seen in the experimental trends, which are slightly spread due to the sensors accuracy, this dependency is not reflected on the simulated tests results, whose measurements are instead ideal.

A particular trend is visible by conducting a one-to-one comparison of the results at each load scenario, which have been split for clarity in Figure 6.22 and Figure 6.23.

It can be seen how the accuracy of the simulation slightly improves along with the increasing user load torque. While the model performs well even at lower loads, the general overlay between the simulated and experimental total losses gets progressively

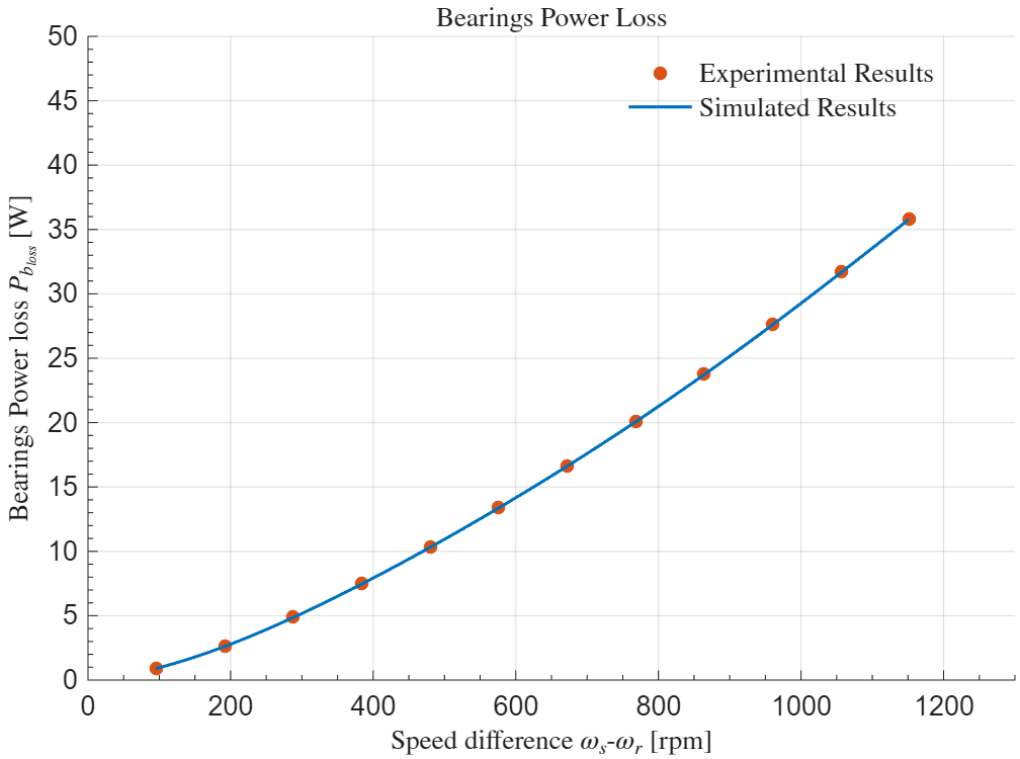

Figure 6.20: Bearings Power Losses: Experimental vs Simulated.

better as the load increases. This result could be due to the reduced noise registered by the torque sensors when higher set torques are applied, leading to an increased signal to noise ratio.

The same trend can be observed in the magnetic power losses results, shown in Figure 6.24, which were adopted to fit the magnetic damping coefficients and that are directly correlated to the total losses.

Overall, these results confirm a very good representation of the physical system by the simulation model, across all the analysed operating conditions and for the whole array of speed configurations tested.

6.5.2 Efficiency Comparison

To complete the model validation, a comparative analysis of the total, bearings and magnetic efficiencies obtained from the simulation environment and from the experimental tests is presented. The objective is to assess the capabilities of the model to replicate with high degrees of accuracy the performances of the PMG system under steady state conditions.

The first and main comparison to be discussed is related to the total efficiencies of the system under the four reference loading conditions. The results are shown in Figure 6.25.

The two sets of tests show very similar results, with the model being able to successfully replicate the shape and slope of the efficiency curves of the prototype. The main

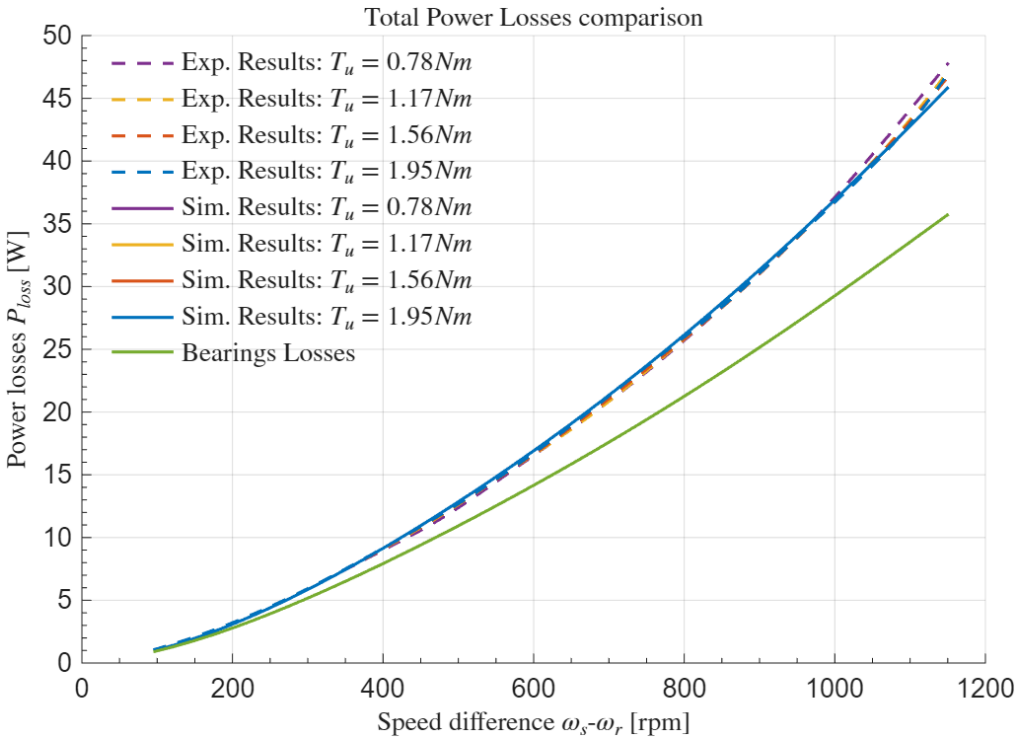

Figure 6.21: Total Power Losses: Experimental vs Simulated.

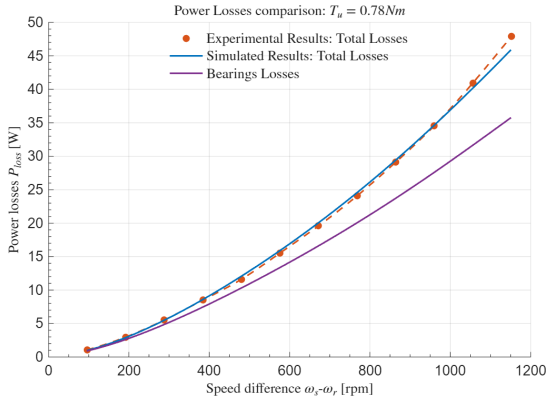

(a) Reference $T_u = 0.78Nm$

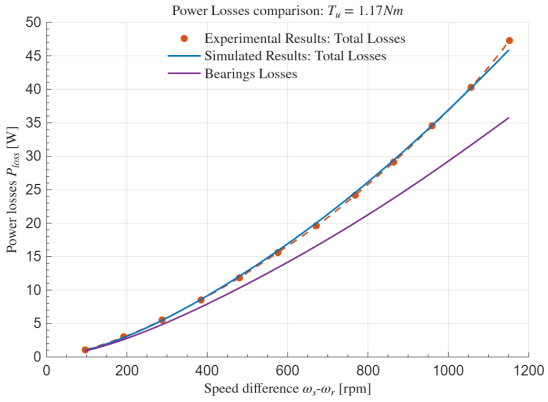

(b) Reference $T_u = 1.17Nm$

Figure 6.22: Detailed Total Power Losses Comparison: part 1.

divergence is found in the tests for the reference user torque of $T_u = 0.78\,Nm$, where the simulation tends to overestimate the efficiency at lower and higher speeds and underestimate them at medium speed configurations. The resulting average difference between the experimental and simulated is of 0.50% across the whole speed spectrum. As previously noted with the power losses comparisons, the results difference is reduced in magnitude as the user load increases. Numerically speaking, the average difference is of 0.33% for the

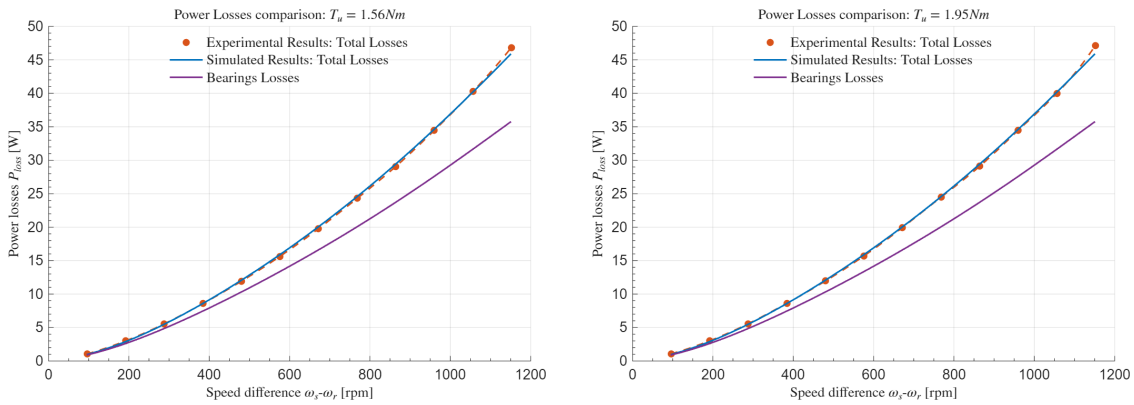

(a) Reference $T_u = 1.56Nm$ (b) Reference $T_u = 1.95Nm$

Figure 6.23: Detailed Total Power Losses Comparison: part 2.

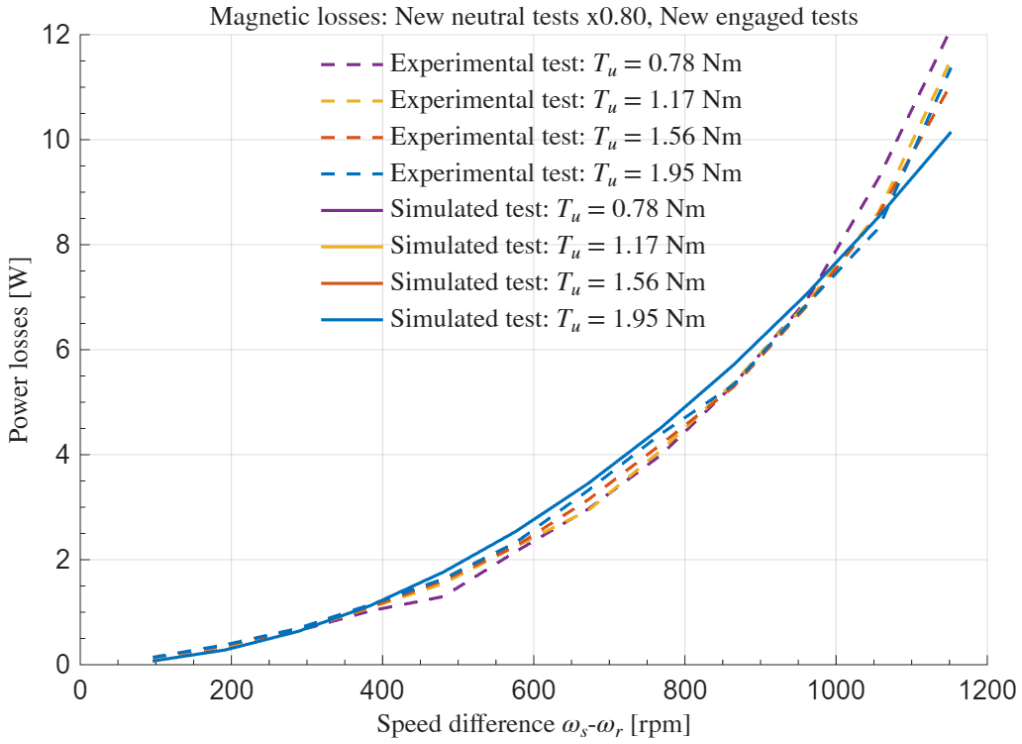

Figure 6.24: Magnetic Power Losses: Experimental vs Simulated.

reference torque of $T_u = 1.17\,Nm$, 0.27% for $T_u = 1.56\,Nm$ and 0.21% for $T_u = 1.95\,Nm$.

This trend is further confirmed in the detailed analysis of all the efficiencies contributions divided by reference user load scenarios, reported respectively in figures Figure 6.26, Figure 6.27, Figure 6.28 and Figure 6.29.

For what concerns the comparison of the efficiencies results at $T_u = 0.78\,Nm$, it is immediately visible how the main differences are due to the magnetic efficiency curves.

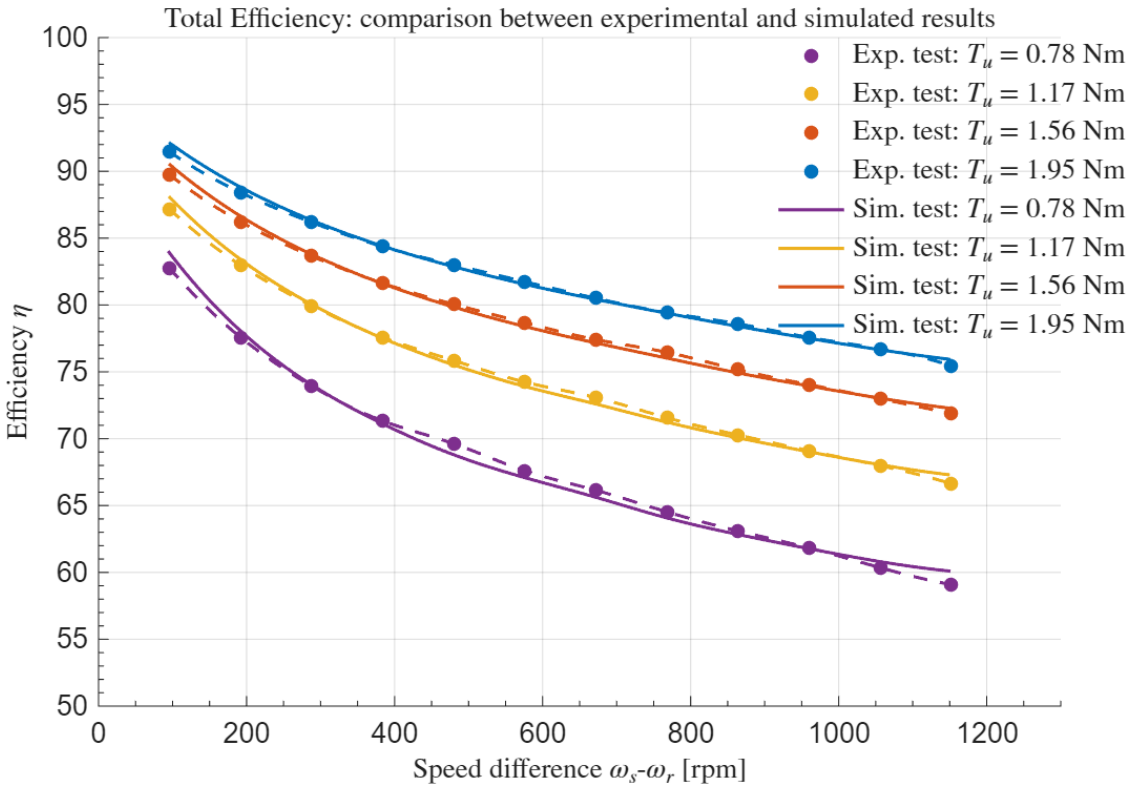

Figure 6.25: Total Efficiency: Experimental vs Simulated.

The main reason of this difference could be due to low signal to noise ratios, meaning that even a small noise could compromise the well effectiveness of the experimental curves obtained. Being the acquisitions of the data from the simulation environment free from any real life noise, a difference in the shape of the curves can be explained. That said, the two curves still follow the same overall trend.

The magnetic efficiencies curves of the other higher loading configurations tend to overlay better, which is a further confirmation of the potential noise contribution in lower loading tests. The results obtained at the highest loading condition, equal to the reference user torque of $T_u = 1.95\,Nm$, are almost perfectly overlaid, demonstrating the capability of the model to reproduce correctly the prototype parameters and characteristics.

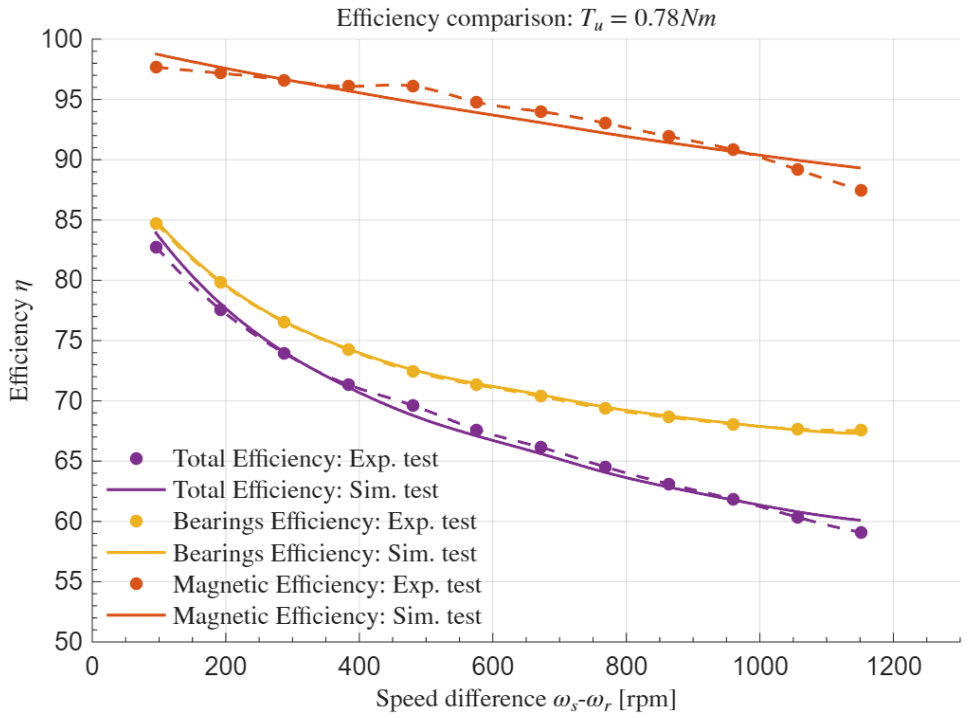

Figure 6.26: Efficiencies Comparison: $T_u = 0.78\ Nm$

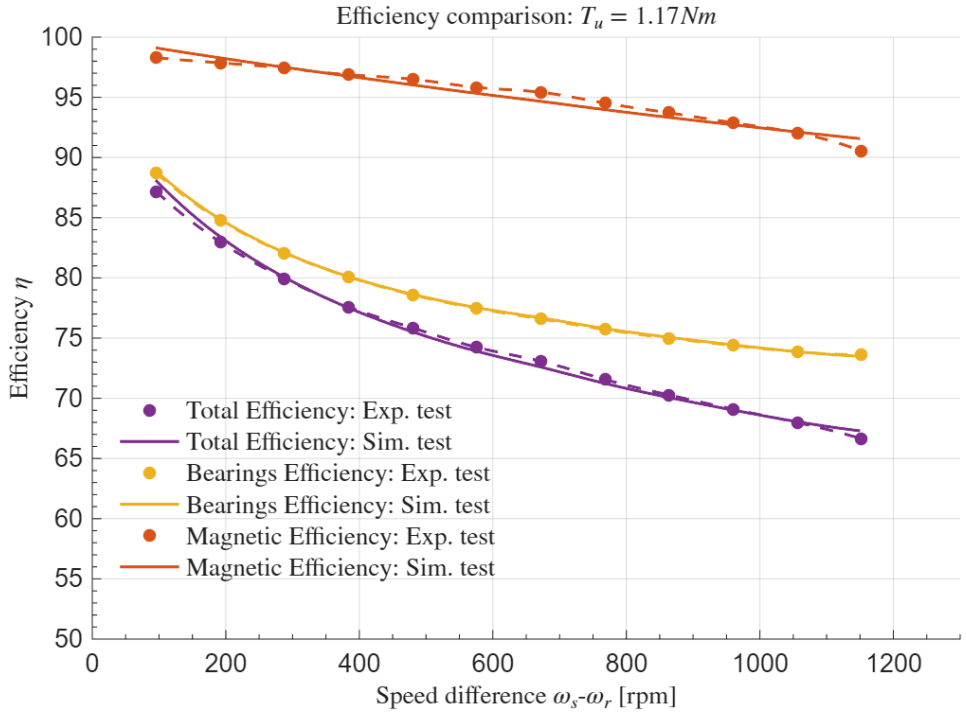

Figure 6.27: Efficiencies Comparison: $T_u = 1.17\ Nm$

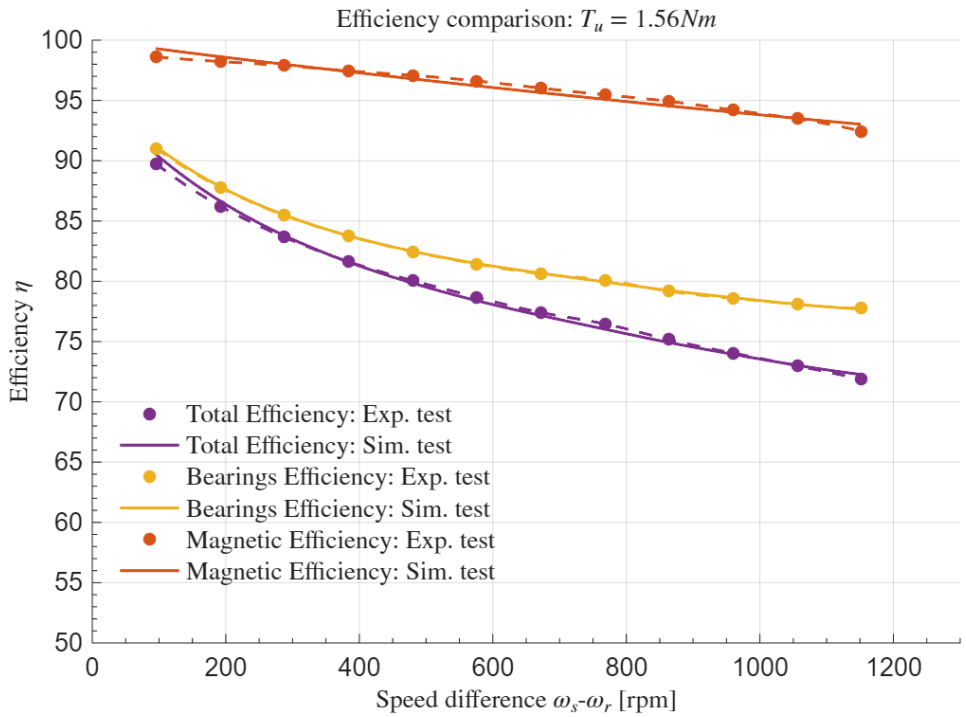

Figure 6.28: Efficiencies Comparison: $T_u = 1{,}56\ Nm$

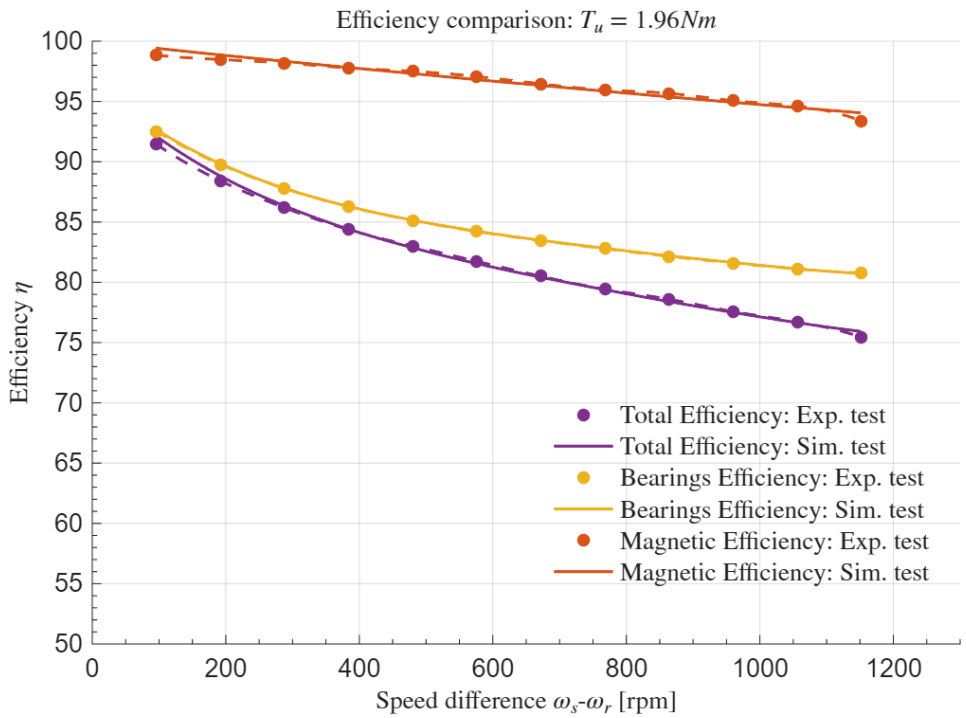

Figure 6.29: Efficiencies Comparison: $T_u = 1.95\,Nm$

In conclusion, the simulation model demonstrated very effective predictive capabilities of the prototype response across several different speed and load scenarios. While its accuracy increases with higher loads scenarios, it always manages to replicate with sufficiently high degrees of accuracy the losses and performances of the PMG system, supporting its use for potential design optimisation and further transient analysis.

Chapter 7

Conclusions

This thesis presented a comprehensive study of the prototype of a Planetary Magnetic Gearbox developed by Politecnico di Torino, and the realisation of a dynamic model in Simulink environment, specifically tuned to the real components that make up the test bench, to perform simulations and additional studies of the analysed system.

The study began with a general overview of the magnetic gears technology, highlighting their advantages over the more traditional mechanical gears, such as reduced wear, innate overload protection and the elimination of lubrication required. The focus then shifted towards the study of a specific configuration, namely the coaxial Planetary Magnetic Gears (PMG), that combines the benefits of the planetary gear system with the non-contact advantages coming from the torque transmission via magnetic coupling between the magnetic rotors. A general overview of the working principle of this technology was provided, along with the derivation of the characteristic dynamic equations and the modelling of the magnetic torque transmission resulting from the Maxwell stress tensor and spatial harmonics theory. The prototype under study was described in detail, including the design strategy previously implemented for the PMG assembly, together with the ancillary components that constitute the test bench. This prototype has been tested in both neutral (disengaged) and engaged configurations, to isolate the mechanical losses and evaluate the gearbox performances respectively. While these tests have already been performed in previous studies, a newer methodology was implemented putting particular attention towards the thermal stability of the test bench before the data acquisition phase, to improve the accuracy and repeatability of the results. Furthermore, a correction coefficient was proposed to correct the neutral tests results to account for the residual magnetic losses still present in the disengaged configuration. The main work of this thesis was the creation of a digital copy of the test bench, under the form of a dynamic model developed in Simulink environment, aimed at replicating both the architecture and the dynamic response of the physical prototype. The model incorporated the main elements of the prototype, namely motors, inertias, transmissions, bearings and, most importantly, the PMG, which incorporated the magnetic torque transmission maps derived from FEM analysis in previous works. A fitting procedure was implemented to calibrate the main parameters of the PMG block, accounting for the magnetic damping losses and the final evaluation of the correction coefficient to be applied to the neutral tests. A comparative

analysis of the simulation tests with the experimental acquisitions was conducted to validate the dynamic model, ensuring that the simulation environment reflects the prototype dynamic response.

Several results have been obtained through this work. For what concerns the experimental test bench, the newer methodology applied to the data acquisition showed significant improvements in either sets of tests. While in the neutral tests the mechanical losses follow trends that are much more physically consistent, in the engaged tests there was an improvement towards the repeatability of the results, with performance results that are much less dependent on the applied loads configurations. Additionally, the definition of a correction coefficient applied to the neutral tests results led to an accurate depiction of the magnetic losses in the prototype, which has been essential for the estimation of its magnetic damping coefficients. Other important results come from the creation of a consistent and accurate dynamic model of the system under study, which capabilities of replicating the performances of the prototype has been demonstrated, with an average prediction error of the total efficiency below 0.5% across all load scenarios. Furthermore, the simulation results confirmed that the main source of power losses inside the system are due to the mechanical friction of the bearings in the PMG assembly, accounting for $60\% - 80\%$ of the total losses. Overall, the model demonstrated strong predictive capabilities of the dynamic behaviour of the test bench, validating its use as a simulation tool that can be adopted for further evaluation and analysis.

While this study obtained significant results, some other analyses and issues can be further studied in future works. For starters, the study of the second gear configuration of the prototype can be further analysed, together with the simulation on the dynamic model of this condition, to further validate the proper design of the simulation environment. Another important aspect that can be discussed is the frequency response of the system. Some preliminary analyses have already been performed, however inconclusive results have been obtained and as such have not been inserted into this work. Finally, it could be useful to implement into the simulation environment a degradation model that can study how a degradation of the system and of the permanent magnets or iron poles could affect the torque transmission capability of the system.

In conclusion, this thesis has shown significant results regarding the effectiveness of using a combined experimental and simulation approach to study a planetary magnetic gears system dynamic response. The developed PMG model will allow for additional tests to be performed on the magnetic gears' technology, allowing for the research to progress and potentially getting closer to a mainstream application of this power transmission technology.

Bibliography

[1] C. Armstrong. Power-transmitting device. *U.S. Patent 687292*, Nov.26, 1901.

[2] K. Atallah, S.D. Calverley, and D. Howe. Design, analysis and realisation of a high-performance magnetic gear. *IEE Proceedings - Electric Power Applications*, 151:135–143, 2004.

[3] K. Atallah and D. Howe. A novel high-performance magnetic gear. *IEEE Transactions on Magnetics*, 37(4):2844–2846, 2001.

[4] Lotfi Baghli, E Gouda, S Mezani, and A Rezzoug. Hybrid vehicle with a magnetic planetary gear. *Mediterranean Journal of Measurement and Control*, 7(2):211–220, 2011.

[5] Nicola LA BELLA. Test bench development for poc power transmission magnetic gears. Master's thesis, POLITECNICO DI TORINO, July 2022.

[6] Christopher G. Cooley and Robert G. Parker. A review of planetary and epicyclic gear dynamics and vibrations research. *Applied Mechanics Reviews*, 66(4):040804, 06 2014.

[7] Boqun Dai, Kenji Nakamura, Yuma Suzuki, Yuichi Tachiya, and Kingo Kuritani. Cogging torque reduction of integer gear ratio axial-flux magnetic gear for wind-power generation application by using two new types of pole pieces. *IEEE Transactions on Magnetics*, 58(8):1–5, 2022.

[8] Melaine Desvaux, Roman Le Goff Latimier, Bernard Multon, Hamid Ben Ahmed, and StÃ©phane Sire. Design and optimization of magnetic gears with arrangement and mechanical constraints for wind turbine applications. In *2016 Eleventh International Conference on Ecological Vehicles and Renewable Energies (EVER)*, pages 1–8, 2016.

[9] Luca Dimauro. Power transmission systems: from traditional to magnetic gearboxes. 2021.

[10] Tugan Eritenel and Robert G. Parker. Three-dimensional nonlinear vibration of gear pairs. *Journal of Sound and Vibration*, 331(15):3628–3648, 2012.

[11] H. Faus. Magnet gearing. May.27, 1941.

[12] Ningjun Feng, H. J. Yu, L. L. Huang, W. P. Zhong, and Z. Shi. Performance analysis of a magnetic-geared linear permanent magnet generator for wave energy conversion. *2015 IEEE Magnetics Conference (INTERMAG)*, pages 1–1, 2015.

[13] Daniel Fodorean. State of the art of magnetic gears, their design, and characteristics with respect to ev application. In Mohamed Amine Fakhfakh, editor, *Modeling and Simulation for Electric Vehicle Applications*, chapter 4. IntechOpen, Rijeka, 2016.

[14] Tommy V. Frandsen, Laszlo Mathe, Nick Ilsoe Berg, Rasmus Koldborg Holm, Torben N. Matzen, Peter Omand Rasmussen, and Kasper K. Jensen. Motor integrated permanent magnet gear in a battery electrical vehicle. *IEEE Transactions on Industry Applications*, 51(2):1516–1525, 2015.

[15] Tommy Vestergaard Frandsen. Motor integrated permanent magnet gear, 2016. Associate Prof. Peter Omand Rasmussen, Aalborg University.

[16] Nicolas W. Frank and Hamid A. Toliyat. Gearing ratios of a magnetic gear for marine applications. In *2009 IEEE Electric Ship Technologies Symposium*, pages 477–481, 2009.

[17] Linni Jian, K. T. Chau, Wenlong Li, and Jiangui Li. A novel coaxial magnetic gear using bulk hts for industrial applications. *IEEE Transactions on Applied Superconductivity*, 20(3):981–984, 2010.

[18] Janusz KoÅodziej, RafaÅ Gabor, Marcin Kowol, and Marian Åukaniszyn. Theoretical and experimental comparison of gear systems: planetary mechanical transmission and coaxial magnetic gear. *Bulletin of the Polish Academy of Sciences Technical Sciences*, 72(5):e150334, 2024.

[19] Wenlong Li, K. T. Chau, and J. Z. Jiang. Application of linear magnetic gears for pseudo-direct-drive oceanic wave energy harvesting. *IEEE Transactions on Magnetics*, 47(10):2624–2627, 2011.

[20] Wenlong Li, K. T. Chau, and J. Z. Jiang. Application of linear magnetic gears for pseudo-direct-drive oceanic wave energy harvesting. *IEEE Transactions on Magnetics*, 47(10):2624–2627, 2011.

[21] Aurelio Liguori, Enrico Armentani, Alcide Bertocco, Andrea Formato, Arcangelo Pellegrino, and Francesco Villecco. Noise reduction in spur gear systems. *Entropy*, 22(11), 2020.

[22] Lukasz Macyszyn, Cezary Jedryczka, and Adam Myszkowski. Simulation and experimental investigation of a two-stage magnetic precession gear. *Energies*, 14(7), 2021.

[23] T. B. Martin. Magnetic transmission. *U.S. Patent 3378710*, Apr.16, 1968.

[24] Y. Mizuana, Kenji Nakamura, Y. Suzuki, Y. Oishi, Y. Tachiya, and K. Kuritani. Performance improvement of spoke-shaped interior permanent magnet magnetic gear. *Journal of the Magnetics Society of Japan*, 45:50–55, 05 2021.

[25] Alvarez-Valenzuela M. A. Sanchez-Garcia-Casarrubios J. Cristache C. Valiente-Blanco I. Perez-Diaz J. L., Diez-Jimenez E. Magnetic gearboxes for aerospace applications. In *The 42nd Aerospace Mechanism Symposium*, May 1, 2014.

[26] G. Puchhammer. Miniaturized magnetic gear as part of satellite component driving mechanisms. In *ACTUATOR 2018; 16th International Conference on New Actuators*, pages 1–4, 2018.

[27] Matthew Bergstresser Rochelle Enrera. Permanent magnet | definition, characteristics uses. Technical report, 2023.

[28] Gerardo Ruiz-Ponce, Marco A. Arjona, Concepcion Hernandez, and Rafael Escarela-Perez. A review of magnetic gear technologies used in mechanical power transmission. *Energies*, 16(4), 2023.

[29] Jalal Sepaseh, Naghi Rostami, M. Reza Feyzi, and Mohammad Bagher Bannae Sharifian. Optimal design of an axial magnetic gear by using particle swarm optimisation method. *IET Electric Power Applications*, 16, 03 2022.

[30] Ashokkumar Sundararathan, Antony Casmir Jayaseelan, Akshay Pradeep, and Amaljith Biju. Design and fabrication of drilling machine using contactless magnetic transmission system. *AIP Conference Proceedings*, 3042(1):020023, 03 2024.

[31] P. M. Tlali, R-J. Wang, and S. Gerber. Magnetic gear technologies: A review. In *2014 International Conference on Electrical Machines (ICEM)*, pages 544–550, 2014.

[32] Pushman Tlali, Rong-Jie Wang, and Stiaan Gerber. Magnetic gear technologies: A review. 09 2014.

[33] Jungang Wang, Liqun Qian, Shuairui Xu, and Ruina Mo. Analysis of electromagnetic performance of modulated coaxial magnetic gears used in semi-direct drive wind turbines. *Energy Engineering*, 118:251–264, 12 2020.

[34] Yawei Wang, Mattia Filippini, Giacomo Bacco, and Nicola Bianchi. Parametric design and optimization of magnetic gears with differential evolution method. *IEEE Transactions on Industry Applications*, 55(4):3445–3452, 2019.

[35] RJ Willis Jr. On the kinematics of the closed epicyclic differential gears. 1982.

[36] Bo Yan, Xianglin Li, Xiuhe Wang, and Yubo Yang. A review on the fieldâmodulated magnetic gears: Development status, potential applications, and existent challenges. *IET Electric Power Applications*, 18, 10 2023.

[37] Z.Q. Zhu and D. Howe. Influence of design parameters on cogging torque in permanent magnet machines. *IEEE Transactions on Energy Conversion*, 15(4):407–412, 2000.

Appendix A

Experimental Tests Grids

A.1 Neutral Tests Grids

$T_{b_{tot}}$ (Nm)		Ring speed n_r (rpm)												
		0	60	120	180	240	300	360	420	480	540	600	660	720
Sun speed n_s (rpm)	0	0.08	0.15	0.20	0.21	0.23	0.25	0.26	0.27	0.27	0.28	0.28	0.28	0.29
	60	0.13	0.17	0.20	0.22	0.23	0.25	0.26	0.27	0.28	0.28	0.28	0.29	0.29
	90	0.08	0.17	0.19	0.22	0.24	0.25	0.26	0.27	0.28	0.28	0.28	0.29	0.29
	120	0.11	0.19	0.20	0.22	0.24	0.25	0.27	0.27	0.28	0.28	0.28	0.29	0.29
	156	0.09	0.19	0.19	0.22	0.24	0.25	0.27	0.27	0.28	0.28	0.28	0.29	0.29
	312	0.09	0.16	0.20	0.22	0.25	0.26	0.27	0.28	0.29	0.29	0.29	0.29	0.30
	468	0.07	0.17	0.20	0.23	0.25	0.27	0.28	0.29	0.30	0.29	0.29	0.30	0.30
	624	0.08	0.17	0.21	0.24	0.26	0.28	0.29	0.29	0.30	0.30	0.30	0.30	0.31
	780	0.11	0.18	0.21	0.24	0.26	0.28	0.29	0.30	0.29	0.29	0.30	0.30	0.30
	936	0.10	0.19	0.23	0.25	0.27	0.29	0.30	0.30	0.31	0.31	0.31	0.32	0.33
	1092	0.15	0.20	0.23	0.26	0.28	0.29	0.31	0.31	0.32	0.32	0.32	0.33	0.34
	1248	0.11	0.20	0.24	0.26	0.28	0.30	0.31	0.32	0.32	0.33	0.33	0.34	0.34
	1404	0.12	0.21	0.24	0.27	0.29	0.31	0.32	0.33	0.33	0.34	0.34	0.35	0.36
	1560	0.12	0.21	0.25	0.28	0.30	0.32	0.33	0.34	0.35	0.35	0.36	0.37	0.38
	1716	0.16	0.22	0.26	0.29	0.31	0.33	0.34	0.35	0.36	0.36	0.37	0.38	0.39
	1872	0.18	0.23	0.27	0.30	0.33	0.35	0.36	0.37	0.38	0.38	0.39	0.40	0.41

Table A.1: New Neutral Tests Results: Total Bearings torque loss.

T_{bs} **(Nm)**		**Ring speed n_r (rpm)**												
		0	60	120	180	240	300	360	420	480	540	600	660	720
Sun speed n_s (rpm)	0	0.06	0.02	0.02	0.02	0.02	0.01	0.01	0.01	0.01	0.01	0.01	0.01	0.01
	60	0.04	0.02	0.03	0.02	0.02	0.02	0.02	0.02	0.02	0.02	0.02	0.02	0.02
	90	0.04	0.04	0.03	0.03	0.03	0.03	0.02	0.02	0.02	0.02	0.02	0.02	0.02
	120	0.05	0.05	0.03	0.03	0.03	0.03	0.03	0.03	0.03	0.03	0.02	0.02	0.02
	156	0.05	0.06	0.04	0.03	0.03	0.03	0.03	0.03	0.03	0.03	0.03	0.03	0.03
	312	0.06	0.05	0.05	0.05	0.05	0.05	0.05	0.04	0.04	0.04	0.04	0.04	0.04
	468	0.06	0.06	0.06	0.06	0.06	0.06	0.06	0.06	0.05	0.05	0.05	0.05	0.05
	624	0.07	0.07	0.07	0.07	0.07	0.07	0.07	0.07	0.06	0.06	0.06	0.06	0.06
	780	0.07	0.07	0.07	0.07	0.07	0.07	0.07	0.06	0.07	0.07	0.06	0.06	0.06
	936	0.09	0.09	0.09	0.09	0.09	0.09	0.08	0.08	0.08	0.08	0.08	0.08	0.08
	1092	0.10	0.10	0.10	0.10	0.10	0.10	0.09	0.09	0.09	0.09	0.09	0.09	0.09
	1248	0.11	0.11	0.11	0.10	0.10	0.10	0.10	0.10	0.10	0.10	0.10	0.10	0.10
	1404	0.11	0.11	0.11	0.11	0.11	0.11	0.11	0.11	0.11	0.11	0.11	0.11	0.11
	1560	0.12	0.12	0.12	0.12	0.12	0.12	0.12	0.11	0.11	0.11	0.11	0.11	0.11
	1716	0.12	0.12	0.12	0.12	0.12	0.12	0.12	0.12	0.12	0.12	0.12	0.12	0.12
	1872	0.13	0.13	0.13	0.13	0.13	0.13	0.13	0.13	0.13	0.13	0.13	0.13	0.13

Table A.2: New Neutral Tests Results: Sun shaft Bearings torque loss.

T_{br} **(Nm)**		**Ring speed n_r (rpm)**												
		0	60	120	180	240	300	360	420	480	540	600	660	720
Sun speed n_s (rpm)	0	0.02	0.13	0.18	0.19	0.22	0.23	0.25	0.25	0.26	0.26	0.27	0.27	0.28
	60	0.09	0.14	0.17	0.19	0.21	0.23	0.24	0.25	0.26	0.26	0.26	0.27	0.27
	90	0.04	0.13	0.16	0.19	0.21	0.23	0.24	0.25	0.25	0.26	0.26	0.27	0.27
	120	0.06	0.14	0.18	0.18	0.21	0.23	0.24	0.25	0.25	0.25	0.26	0.26	0.27
	156	0.04	0.13	0.15	0.18	0.20	0.22	0.23	0.24	0.25	0.25	0.26	0.26	0.26
	312	0.03	0.11	0.15	0.17	0.20	0.21	0.23	0.24	0.24	0.25	0.25	0.25	0.26
	468	0.01	0.10	0.14	0.17	0.19	0.21	0.22	0.23	0.24	0.24	0.24	0.24	0.25
	624	0.01	0.10	0.14	0.17	0.19	0.21	0.22	0.23	0.23	0.23	0.23	0.24	0.25
	780	0.04	0.10	0.14	0.17	0.19	0.20	0.22	0.23	0.22	0.23	0.23	0.24	0.24
	936	0.02	0.10	0.14	0.16	0.18	0.20	0.21	0.22	0.22	0.23	0.23	0.24	0.24
	1092	0.05	0.10	0.13	0.16	0.18	0.20	0.21	0.21	0.22	0.23	0.23	0.24	0.25
	1248	0.00	0.10	0.13	0.16	0.18	0.20	0.21	0.22	0.22	0.23	0.23	0.24	0.24
	1404	0.01	0.10	0.13	0.16	0.18	0.20	0.21	0.22	0.23	0.23	0.24	0.24	0.25
	1560	0.00	0.10	0.14	0.16	0.19	0.20	0.22	0.23	0.23	0.24	0.24	0.25	0.26
	1716	0.04	0.10	0.14	0.17	0.19	0.21	0.22	0.23	0.24	0.24	0.25	0.26	0.27
	1872	0.05	0.10	0.14	0.17	0.20	0.22	0.23	0.24	0.25	0.26	0.26	0.27	0.29

Table A.3: New Neutral Tests Results: Ring shaft Bearings torque loss.

A.2 Engaged Tests Grids

T_s (Nm)		Ring Torque T_r (Nm)			
		0.78	1.17	1.56	1.95
Sun speed n_s (rpm)	156	0.38	0.51	0.64	0.77
	312	0.41	0.54	0.67	0.80
	468	0.43	0.56	0.69	0.82
	624	0.45	0.58	0.71	0.84
	780	0.47	0.60	0.73	0.86
	936	0.49	0.62	0.75	0.88
	1092	0.51	0.64	0.77	0.90
	1248	0.52	0.65	0.79	0.91
	1404	0.54	0.67	0.80	0.92
	1560	0.55	0.68	0.81	0.94
	1716	0.57	0.70	0.83	0.96
	1872	0.60	0.72	0.85	0.98

Table A.4: New Engaged Tests Results: Sun shaft Torque.

T_r (Nm)		Ring Torque T_r (Nm)			
		0.78	1.17	1.56	1.95
Sun speed n_s (rpm)	156	0.81	1.15	1.49	1.82
	312	0.82	1.16	1.50	1.83
	468	0.83	1.17	1.51	1.84
	624	0.84	1.18	1.52	1.85
	780	0.85	1.19	1.52	1.86
	936	0.86	1.20	1.53	1.87
	1092	0.87	1.21	1.54	1.87
	1248	0.87	1.21	1.57	1.88
	1404	0.88	1.22	1.55	1.89
	1560	0.89	1.23	1.56	1.90
	1716	0.90	1.24	1.57	1.91
	1872	0.92	1.25	1.59	1.92

Table A.5: Old Engaged Tests Results: Ring shaft Torque.